

**DETECTION OF BLADE'S DEFECT USING
BENDING VIBRATIONS OF A SHAFT IN A
SHAFT-DISK-BLADE SYSTEM**

BY

Ali L. Alsaleh

A Thesis Presented to the
DEANSHIP OF GRADUATE STUDIES

KING FAHD UNIVERSITY OF PETROLEUM & MINERALS

DHAHRAN, SAUDI ARABIA

In Partial Fulfillment of the
Requirements for the Degree of

MASTER OF SCIENCE

In

MECHANICAL ENGINEERING

April 2020

KING FAHD UNIVERSITY OF PETROLEUM & MINERALS
DHAHRAN- 31261, SAUDI ARABIA
DEANSHIP OF GRADUATE STUDIES

This thesis, written by **Ali L. Alsaleh** under the direction of his thesis advisor and approved by his thesis committee, has been presented and accepted by the Dean of Graduate Studies, in partial fulfillment of the requirements for the degree of **MASTER OF SCIENCE IN MECHANICAL ENGINEERING**.

Zuhair
Gasem

Digitally signed by Zuhair Gasem
DN: cn=Zuhair Gasem, o=KFUPM, ou=Chair, 1.3
Digitally signed by Zuhair Gasem
DN: cn=Zuhair Gasem, o=KFUPM, ou=Chair, 1.3

Dr. Zuhair Gasem
Department Chairman

Dr. Suliman S. Al-Homidan
Dean of Graduate Studies

Date



Dr. Salem Bashmal
(Advisor)

Dr. Yehia Khulief
(Member)

Dr. Abdel Aziz Bazoune
(Member)

© Ali L. Alsaleh

2020

To the loved ones who passed away too soon, I dedicate this work.

ACKNOWLEDGMENTS

I would like to start by thanking my advisor, Dr. Salem Bashmal for his support and guidance throughout my thesis journey. The appreciation is extended to my thesis committee members, Dr. Khuleif and Dr. Bazoune, for their enriching remarks and crucial advices that helped advancing my research, and to all the faculty that crossed my path during this wonderful journey at KFUPM; each one of them has helped me grow to reach where I am today.

Special thanks go to my family and friend for their continuous support. The final thanks go to my wife and son for being the light that showed me the way through the darkest nights.

TABLE OF CONTENTS

ACKNOWLEDGMENTS	V
TABLE OF CONTENTS	VI
LIST OF TABLES	X
LIST OF FIGURES	XII
LIST OF ABBREVIATIONS AND SYMBOLS	XVI
ABSTRACT	XX
ملخص الرسالة	XXI
CHAPTER 1 INTRODUCTION	1
CHAPTER 2 LITRITURE REVIEW	3
2.1. BLADE-SHAFT-TORSIONAL DYNAMIC COUPLING	5
2.2. BLADE-SHAFT-BENDING DYNAMIC COUPLING	6
2.3. BLADE FAULTS DETECTION TECHNIQUES	15
2.4. PROPOSED RESEARCH	17
CHAPTER 3 ELASTODYNAMIC MODEL	18
3.1. INTRODUCTION	18
3.2. SYSTEM DESCRIPTION AND MODELING APPROACH	20
3.3. SHAFT ELEMENT	22
3.3.1 <i>Velocity Vector</i>	22
3.3.2 <i>Kinetic Energy of Shaft Element</i>	26

3.3.3	<i>Strain Energy of Shaft Element</i>	27
3.4.	BLADE ELEMENT.....	31
3.4.1	<i>Kinetic Energy of Blade Element</i>	31
3.4.2	<i>Strain and Potential Energy of Blade Element</i>	33
3.5.	DISK ELEMENT.....	34
CHAPTER 4 FINITE ELEMENT MODEL		35
4.1.	INTRODUCTION.....	35
4.2.	DISCRETIZATION AND SHAPE FUNCTIONS	36
4.3.	SHAFT ELEMENT	40
4.4.	BLADE ELEMENT.....	43
4.5.	DISK ELEMENT.....	44
4.6.	EXTERNAL FORCES	45
4.7.	GLOBAL EQUATION OF MOTION	46
4.8.	COUPLING PROPERTIES	48
4.8.1	<i>Element Coordinates Coupling</i>	48
4.8.2	<i>Structural Coupling</i>	48
CHAPTER 5 NUMERICAL SOLUTION.....		50
5.1.	ROTOR DYNAMICS ANALYSIS IN ANSYS	50
5.2.	MODEL PARAMETERS	54
5.3.	INITIAL ELEMENT SELECTION AND MESHING.....	58
5.4.	COUPLING IN ANSYS APDL	61

5.5.	REVISED ELEMENT SELECTION.....	62
5.6.	CONSTRAINTS AND FRAME OF REFERENCE SELECTION	72
5.7.	LOADING AND SOLUTION CONTROLS	75
5.8.	TEST CASES.....	77
	5.8.1 <i>Broken Blade</i>	78
	5.8.2 <i>Pitted Blades (Blades with holes)</i>	79
	5.8.3 <i>Bent Blades</i>	80
CHAPTER 6 VALIDATION OF THE MODEL		81
6.1.	MODEL PARAMETERS COMPARISON.....	81
6.2.	MODAL RESULTS COMPARISON – NO ROTATION	83
6.3.	MODAL RESULTS COMPARISON – WITH ROTATION.....	90
6.4.	EFFECT OF INCREASING THE NUMBER OF BLADES	94
CHAPTER 7 BLADE-DEFECT CASE STUDIES		97
7.1.	MODAL ANALYSIS – NO ROTATION.....	97
7.2.	MODAL ANALYSIS – WITH ROTATION	103
	7.2.1 <i>Broken Blades</i>	103
	7.2.2 <i>Pitted Blades</i>	104
	7.2.3 <i>Bent Blades</i>	106
7.3.	HARMONIC ANALYSIS.....	108
	7.3.1 <i>Healthy Rotor</i>	110
	7.3.2 <i>Blade-Defects Cases</i>	112

7.4. SUMMARY OF FINDINGS.....	120
CHAPTER 8 SENSITIVITY ANALYSIS	122
8.1. APPROACH TO SENSITIVITY ANALYSIS.....	124
8.2. SENSITIVITY ANALYSIS RESULTS	126
CHAPTER 9 CONCLUSION	130
9.1. RECOMMENDATION OF FUTURE RESEARCH	133
REFERENCES	135
VITAE.....	141

LIST OF TABLES

Table 2-1. Rotor Mode Shapes Abbreviations.....	4
Table 5-1. Geometric Parameters of Rotor Model.....	57
Table 5-2. Material Properties and Bearing Characteristics of Rotor Model.....	57
Table 5-3. Initial Rotor Element Selection	60
Table 5-4. First 4 Natural Frequency Values of the Disk Alone	65
Table 5-5. Final Rotor Element Selection.....	65
Table 6-1. Blades' Difference between Research and Benchmarked Model.....	81
Table 6-2. First 9 Mode Shapes of the Non-Rotating Research Model as Compared to the Benchmarked Model.....	83
Table 6-3. First 4 Mode Shape Results of a Non-Rotating Single Blade.....	88
Table 6-4. Modal Results Comparison between the research model and that in [36] at 1000 and 2000 RPM	93
Table 6-5. Modal Results At 0-Speed for a Rotor with Increasing Number of Blades	94
Table 7-1. Modal Results of a Single-Blade Defect in Comparison with a Healthy Rotor Model.....	98
Table 7-2. First 4 Mode Shape Results of a Clamped-Free Bent Blade	99
Table 7-3. Modal Results of a Three-Blades Defect in Comparison with a Healthy Rotor Model.....	100
Table 7-4. Frequency Peaks of The Lateral Deflection of Node 4 to Unbalance Excitation.....	111
Table 7-5. Frequency Peaks of The Lateral Deflection of Node 4 at Each Defect Case	112

Table 8-1. Key Inputs Parameters in this Research 125

Table 8-2. Normalized Sensitivity Results with Variation in Broken-Blade Shortened-Length . 126

Table 8-3. Normalized Sensitivity Results with Variation in Pitted-Blade Hole Diameter..... 126

Table 8-4. Normalized Sensitivity Results with Variation in Bent-Blade Radius of Curvature.. 127

LIST OF FIGURES

Figure 3.1. Schematic of the studied rotor in this work.	20
Figure 3.2 Shaft element cross sectional orientation.	23
Figure 3.3. Rotation angles of shaft element cross section.	24
Figure 3.4. Cross section of blade element.	32
Figure 3.5. Cross section of disk.	34
Figure 4.1. Discretized shaft of the studied rotor.	37
Figure 5.1. Physical dimensions of the model presented in [36].	55
Figure 5.2. Rotor model used in this research: (a) shaft and (b) disk and blades.	56
Figure 5.3. BEAM188 geometry [39].	58
Figure 5.4. COMBI214 geometry [39].	60
Figure 5.5. Blade’s configuration using the initial element selection in Table 5.3. The rigid disk is not visible in this configuration as it modeled as a nodal mass (MASS21).	63
Figure 5.6. Modal analysis of the disk alone, clamped at the inner radius.	64
Figure 5.7. Coupling between the shaft, disk and blades.	66
Figure 5.8. Disk-blades mesh cases for the numerical convergence study: (a) 250 elements (b) 400 elements (c)550 elements (d) 1300 elements (e) 1750 elements (f) 3000 elements	68
Figure 5.9. Modal results of the first 9 modes of the rotor model at 0 speed shown the effect of increasing the number of mesh elements.	69

Figure 5.10. Modal results of the first 9 modes of the rotor model at 5000 RPM shown the effect of increasing the number of mesh elements.....	69
Figure 5.11. Modal results of the first 9 modes of the rotor model at 10000 RPM shown the effect of increasing the number of mesh elements.....	70
Figure 5.12. Modal results of the first 9 modes of the rotor model at 15000 RPM shown the effect of increasing the number of mesh elements.....	70
Figure 5.13. Modal results of the first 9 modes of the rotor model at 20000 RPM shown the effect of increasing the number of mesh elements.....	71
Figure 5.14. Rotor with constraints. The displacement along the axis of rotation is constrained in nodes 1-15, the torsional deflection is constrained in node 15 and all DOF are constrained in bearing's nodes.....	73
Figure 5.15. Rotor model with harmonic excitation. The dashed red lines resemble the excitation force and the dashed blue lines resemble the collected response values.....	76
Figure 5.16. Rotor model with broken blades scenarios.....	78
Figure 5.17. Rotor model with pitted blades scenarios.....	79
Figure 5.18. Rotor model with bent blades scenarios.....	80
Figure 6.1. Graphical model comparison: (a) Benchmarked model [36] (b) Research model.	82
Figure 6.2. Shaft-disk-dominated mode shapes at 0 speed: (a) 1st mode (b) 2nd mode (c) 3rd mode.....	84
Figure 6.3. Shaft-disk-dominated mode shapes at 0 speed: (a) 4th mode (b) 5th mode.	85
Figure 6.4. Blade-dominated mode shapes at 0 speed: (a) 6th mode (b) 7th mode.	86
Figure 6.5. Blade-dominated mode shapes at 0 speed: (a) 8th mode (b)9th mode.	87

Figure 6.6. First four mode shapes of a single clamped-free blade.	88
Figure 6.7. Campbell diagram of a single clamped-free blade.	90
Figure 6.8. Campbell diagram of research model.	91
Figure 6.9. Campbell diagram of the model in [36] as reported. fr donates the 1X line and n correspond to the mode number (1-9) as seen in Table 6.2.	91
Figure 6.10. From the left: model with no blades, with five blades, with 6 blades, with 7 blades.	94
Figure 6.11. Campbell diagram of first 9 modes of the rotor with four blades as compared to a rotor with no blades.	96
Figure 7.1. Mode shapes of a clamped-free bent blade. The second mode is not visible because it is out-of-plane.....	99
Figure 7.2. Mode representation of the model with three bent blades: (a) Mode 7 (b) Mode 8 (c) Mode 9 (d) Mode 10 (e) Mode 11 (f) Mode 12.....	102
Figure 7.3. Campbell diagram of the model with a broken blade compared to a healthy rotor...	103
Figure 7.4. Campbell diagram of rotor with three broken blades compared to a healthy rotor. ...	104
Figure 7.5. Campbell diagram of rotor with a pitted blade compared to a healthy rotor.....	104
Figure 7.6. Campbell diagram of rotor with three pitted blades compared to a healthy rotor.	105
Figure 7.7. Campbell diagram of rotor with a bent blade compared to a healthy rotor.	106
Figure 7.8. Campbell diagram of rotor with a bent blade compared to a healthy rotor.	107
Figure 7.9. Rotor model with harmonic excitation. The dashed red lines resemble the excitation force and the dashed blue lines resemble the collected response values...	109
Figure 7.10. Frequency response of the lateral deflection of Node 4 to unbalance excitation. ...	110

Figure 7.11. Frequency response of the lateral deflection of Node 4 and Node 12 to unbalance excitation.....	112
Figure 7.12. Frequency response of the lateral deflection of a model with one broken blade.....	113
Figure 7.13. Frequency response of the lateral deflection a model with one pitted blade.	114
Figure 7.14. Frequency response of the lateral deflection of a model with one bent blade.....	115
Figure 7.15. Frequency response of the lateral deflection of a model with three broken blades.	116
Figure 7.16. Frequency response of the lateral deflection of a model with three pitted blades...	116
Figure 7.17. Frequency response of the lateral deflection of a model with three bent blades.	116
Figure 7.18. Frequency response of the lateral deflection of a model with three broken blades.	117
Figure 7.19. Frequency response of the lateral deflection of a model with three pitted blades...	118
Figure 7.20. Frequency response of the lateral deflection of a model with three bent blades.	119
Figure 8.1. Sensitivity analysis results of Mode 9 in bent-blade defect.	128
Figure 8.2. Sensitivity analysis results of Mode 10 in bent-blade defect.	128
Figure 8.3. Overall NSC values of the Sensitivity Analysis.....	129

LIST OF ABBREVIATIONS AND SYMBOLS

FFT	:	Fast Fourier Transform
APDL	:	<i>ANSYS</i> Parametric Design Language
FE	:	Finite Element
DOF	:	Degrees of Freedom
SDB	:	Shaft-Disk-Blade
$\bar{\mathbf{r}}$:	Position Vector
$\bar{\mathbf{u}}$:	Deformation Vector
φ	:	Rotation Around the X-axis
θ_y	:	Rotation Around the Y-axis Due to Bending
θ_z	:	Rotation Around the Z-axis Due to Bending
Ω	:	Angular Displacement
$\bar{\boldsymbol{\omega}}$:	Angular Velocity Vector
$[N]$:	Mode Shapes Matrix
$\{q\}$:	Nodal Coordinates Vector
T	:	Kinetic Energy

U	:	Potential Energy
ε	:	Strain Due to Bending
σ	:	Stress Due to Bending
γ	:	Strain Due to Shear
τ	:	Stress Due to Shear
E	:	Young's Modulus of Elasticity
G	:	Shear Modulus of Elasticity
ν	:	Poisson Ratio Due
k	:	Shear Factor
ρ	:	Mass Density of Beam Element
μ	:	Mass Density of Blade Element
V	:	Volume
A	:	Cross-Sectional Area
I	:	Cross-Sectional Area Second Moment of Inertia
I_D	:	Diametral Moment of Inertia
I_P	:	Polar Moment of Inertia
l	:	Longitudinal Length

v	:	Transverse Displacement Along the Y-axis
w	:	Transverse Displacement Along the Z-axis
Ψ	:	Inclination Angle of Blade's Mid-Plane to Rotation Plane
θ^b	:	Total Bending Rotation of Blade
v^{*b}	:	Total Transverse Displacement of Blade
F_c	:	Blade's Centrifugal Forces Along the Longitudinal Axis
m^d	:	Mass of the Disk
β	:	Shear Deformation Parameter in Shape Function
$[M]$:	Mass Matrix
$[K]$:	Stiffness Matrix
$[g], [G]$:	Gyroscopic Effect Matrix
$[B]$:	Lateral Displacement to Angular Displacement Coupling
$[D]$:	Damping Matrix
$\delta W(x, t)$:	Virtual Work
$[f(t)]$:	Nodal Force Row Vector
BEAM188	:	Beam Element in ANSYS
MASS21	:	Nodal Mass Element in ANSYS

COMBI214	:	Isotropic Bearing Element in <i>ANSYS</i>
SHELL181	:	Shell Element in <i>ANSYS</i>
CERIG	:	Coupling Region Command in <i>ANSYS</i>
[$C_{coriolis}$]	:	Coriolis Matrix in <i>ANSYS</i>
[K_c]	:	Spin Softening and Centrifugal Stiffening Matrix in <i>ANSYS</i>
QRDAMP	:	Mode-Superposition Eigen Solver in <i>ANSY</i>
SYNCHRO	:	Applying Synchronous Excitation Command in <i>ANSYS</i>
NSC	:	Normalized Sensitivity Coefficient

ABSTRACT

Full Name : Ali L. Alsaleh

Thesis Title : Detection of Blade's Defect Using Bending Vibrations of a Shaft in Shaft-Disk-Blades System

Major Field : Mechanical Engineering

Date of Degree : April 2020

This thesis investigates the feasibility of detecting defects in blades through the numerical analysis of the coupling between blade-bending and shaft lateral vibrations in a shaft-disk-blades (SDB) system. Based on the energy principle and Lagrange's equations, the equation of motion governing the dynamics of the system is established taking into account shear deformation, rotary inertia and centrifugal forces effects. The model is numerically simulated using *ANSYS APDL* software, where modal and harmonic analyses are conducted to generate the results of the study. Prior to carrying out the case studies, the model is validated via model-results benchmark and found in agreement with similar models in the literature. Three blade's defect scenarios are simulated in this thesis; a broken blade, pitted blade and a bent blade. The results of the analysis revealed the existence of coupling between blade-bending and shaft-lateral vibrations. The influence of the bent blade was largest among those modes, followed by the broken blade and lastly comes the pitted blade with the least influence. The results of the harmonic analysis revealed that detecting blade's defect is viable through monitoring the shaft lateral vibrations amplitude at frequency values corresponding to the blade-bending and shaft-lateral vibrations coupled modes. Lastly, the results' sensitivity is assessed through a deterministic sensitivity analysis and is found, for the most part, insensitive to scatter in the input.

ملخص الرسالة

الاسم الكامل: علي لؤي الصالح

عنوان الرسالة: الكشف عن عيوب الشفرات باستخدام تحليل اهتزازات عمود الدوران في المعدات الدوارة

التخصص: الهندسة الميكانيكية

تاريخ الدرجة العلمية: رمضان 1441

تبحث هذه الأطروحة جدوى اكتشاف عيوب الشفرات من خلال تحليل اهتزازات عمود الدوران الجانبية. استنادًا إلى مبدأ الطاقة، تم إنشاء معادلة الحركة التي تحكم ديناميكية معدة دوارة تتكون من عمود دروران، قرص و شفرات. لدراسة أثر انعطاب الشفرات على اهتزازات عمود الدوران، تمت محاكاة النموذج عددًا باستخدام برنامج المحاكاة، حيث يتم إجراء التحليلات الشكلية والتوافقية لاهتزازات النموذج للحصول على نتائج الدراسة. تم التحقق من صحة النموذج من خلال مقارنته بدراسات سابقة مشابهة تم نشرها. من ثم تمت دراسة ثلاثة سيناريوهات تحاكي عيوب مختلفة في الشفرات وهي كالتالي: شفرة مكسورة ، شفرة مثقوبة وشفرة مثنية. أظهرت نتائج الدراسة وجود اقتران بين اهتزازات ثني الشفرة والاهتزازات الجانبية لعمود الدوران. كان تأثير الشفرة المثنية هو الأكبر من بين تلك السيناريوهات ، متبوعًا بالشفرة المكسورة وأخيرًا تأتي الشفرة المثقوبة بأقل تأثير. فيما كشفت نتائج الدراسة أيضًا أن اكتشاف عيب الشفرة قابل للتطبيق من خلال مراقبة الاهتزازات الجانبية للعمود عند قيم التردد المقابلة لأنماط الانحناء للشفرة المتوافقة مع الاهتزازات الجانبية للعمود.

CHAPTER 1

INTRODUCTION

With the heavy engagement of modern turbomachinery in various industries, researchers have put decent efforts to discuss and assess machine failures in an attempt to increase their reliability and minimize unscheduled shutdowns. Their ultimate objective is either to prevent failures through selecting the appropriate design parameters, or establishing effective means of condition-monitoring programs to detect failures at early stages. For several decades, many condition-monitoring programs have been developed to address different aspects of machinery protection such as temperature and pressure monitoring, acoustic emissions, infrared thermography programs, etc. [1]. Vibration monitoring, nevertheless, have been proved to be the most effective method to monitor machine health and anticipate failures at early stages [2].

Turbomachines are subject to high vibrations for various reasons, one of which is blade faults. Blade faults may occur during operation in the form of twisting, breaking, bending, cracking, rubbing, pitting, looseness or creep [3]. Such types of faults could be induced by initial defect or get developed over time due to cyclic loading or fluid and foreign objects interactions. According to Meher-Homji [4], blade faults are the primary cause of failure in gas turbines and jet engines as they represent 42% of total failures. One way to limit the impact of blade faults in turbomachines is the early detection of their existence through vibration monitoring and diagnosis.

Faults in blades act as excitation to the machine resulting in a dynamic response in the form of vibration signal. Analyzing the vibration signal can form a diagnosis tool with the potential to aid detecting such faults. The current practice with regards to collecting vibrations signals in general involves various means. Some of which are costly and hard to work with such as tip timing measurements, others are cheap and easy to work with such as shaft lateral motion measurement through accelerometers. The signal collected by the different means are then analyzed and interpreted through several analysis methods, some of which includes Fast Fourier Transform (FFT), wavelet analysis, Empirical Mode Decomposition, Hilbert-Huang Transform, etc. [3]. Recently, there were many published studies employing such techniques to identify blade-faults signature.

The objective of this thesis is to investigate the feasibility of using shaft lateral vibrations to detect defects in blades through modal and harmonic analyses. The subsequent chapters detail the work done in this regard. Starting with a literature survey in Chapter 2, the recent related studies are reviewed in order to build a supporting background and identify the proper research contribution of this work. The underlying theory of the elastodynamic model is then discussed in Chapter 3 followed by a formulation of the mathematical model using the FE method in Chapter 4. Chapter 5 describes the solution to the numerical model using *ANSYS* FE package. In Chapter 6, the developed model is validated by means of comparison with a similar model from literature. The study-cases results are then discussed highlighting the key findings of each case in Chapter 7. In Chapter 8, a deterministic sensitivity analysis of the results is presented to assess the reliability of the model and the outcome of the study. Finally, In Chapter 9, the conclusion of the thesis is summarized followed by suggestions on future work.

CHAPTER 2

LITERATURE REVIEW

This chapter presents a comprehensive literature review addressing blades faults detection through shaft vibration analysis. The intention is to give an overview of the recent works done in the literature in this field and identify possible areas of contribution.

There have been many publications in the literature discussing various means of detecting blade faults in machinery operation. Before presenting those publications, one needs to develop an insight of the coupled dynamics among shaft and blade in bladed rotor systems. This insight will aid the selection of the appropriate detection mean for the various blade failure applications. The coupled dynamics among shafts and blades in bladed rotors is usually represented through the coupling of element mode shapes. Bladed rotors in their simplest form consists of a shaft, disk and blades all attached to each other and rotates at the same angular speed. The shaft, disk and blades can be subjected to excitation forces through different ways (i.e. elastic destructive forces on the shaft, fluid turbulence excitation on the blades, etc.). The rotor system will develop a response to the excitation usually in the form of vibrations. The energy induced by the vibrations can be transferred from one element to another, from the blades into the shaft for instance, at specific mode shapes. At these modes, the dynamics between the shaft and the blades are coupled, and the modes are called coupled mode shapes [5].

Researchers in this field discussed several coupling mode-shapes between shafts and blades in rotors. Those modes can be classified into two main families: (1) blade-shaft-torsional and (2) blade-shaft-bending coupling modes families. The first coupling family occurs when the dynamics of the blades (i.e. in-plane or out-of-plane bending, transverse) influence the shaft torsional motion or vice versa. Whereas the second coupling family occurs when the dynamics of the blades influences the shaft bending (lateral) motion and vice versa. Table 2.1 list the rotor mode-shapes abbreviations that will be used throughout this manuscript.

Table 2-1. Rotor Mode Shapes Abbreviations

Abbreviation	Description
Shaft-dominated Mode Shapes	Rotor mode shapes that are primarily influenced by the shaft bending and torsional mode shapes.
Disk-Swing Mode Shapes	Rotor mode shapes that are primarily influenced by the disk swing motion.
Blade-dominated Mode Shapes	Rotor mode shapes that are primarily influenced by the blade's first bending mode shape.
Blade-Blade Coupling Mode Shapes	Rotor mode shapes that couple blades vibrations only.
Blade-Shaft Coupling Mode Shapes	Rotor mode shapes that couple blades bending vibrations to shaft vibrations. The coupling can be either with shaft-lateral vibrations or shaft-torsional vibrations.

2.1. Blade-shaft-torsional dynamic coupling

The blade-shaft-torsional dynamic coupling has been thoroughly investigated in the literature. Many studies proposed well-established mathematical models that shows the influence of blade bending and transverse vibrations on the shaft torsional vibrations [6,7,8,9,10]. Yang and Huang [7,10] developed a mathematical model to investigate shaft-torsional and blade-bending vibrations and the effect of blade number, longitudinal flexibility and stagger angle on the coupling dynamics of a shaft-disk-blade rotor. Their model assumed flexible blades attached to a rigid disk of a stagger angle. The vibration excitation was applied on the shaft torsional and longitudinal direction. The equation of motion governing the dynamics of the system was developed using the energy approach and solved by the assumed modes method. The results were represented in terms of system frequencies and mode shapes. Among the several conclusions they came out with, Yang and Huang found that the coupling among shaft torsional and blade-bending vibrations is clearly reflected on the system mode shapes, as shaft torsional vibrations were largely affected by blade bending and vice versa.

In a similar approach, Al-Bedoor [8] investigated the shaft-torsional and blade-bending coupling using a linearized reduced order mathematical model. The blades were modeled using Euler-Bernoulli beam theory and accounting for the stagger angle. The blade stiffening due to centrifugal forces and blade shortening were considered. The results were interpreted in terms of coupled natural frequencies and compared to an (FE) model generated by *Pro-Mechnaica* were there was a good agreement. Al-Bedoor found that different system properties, such as stagger angle, rotating blade inertia and rotating speed,

have a direct effect on the coupled natural frequencies of the shaft-blade system. Hwanhee et al [9] followed Al-Bedoor methodology but considered a nonlinear dynamic system modeling pre-twisted blades. Upon interpreting the results through modal analysis, the authors have found that the pre-twisting angle and shaft torsional flexibility largely affect the coupled natural frequencies of the system. The presented studies and many more suggest that blade vibration signature can be in fact deduced from shaft torsional vibration analysis.

2.2. Blade-shaft-bending dynamic coupling

Unlike the blade-shaft torsional coupling dynamics, there has not been as many studies discussing the coupling dynamics among blades and shaft bending vibrations. In fact, studies in this field often neglect this coupling-mode family as it is considered rare [11,12,13]. In the following, the major studies that addressed the coupling dynamics among blades and shaft-bending vibrations are presented.

Al-Bedoor, et al. [6] investigated experimentally the effect of blade random vibrations on rotor-assembly lateral and torsional vibrations. The test rig used in this experiment consists of a varying-in-length shaft, a single disk with four blades and two roller-element bearings. The torsional and blade-bending vibrations were measured using five strain-gauges stations, two at the blades and three on the shaft. The lateral vibrations of the rotor assembly were measured using accelerometers mounted on the bearing housings. Different from other experimental works in this field where the excitation is generated via a distinct or sweep frequency, the authors used a shaker generating a white random signal to simulate a realistic forcing condition where a wide spectrum of frequencies are excited, much similar

to a real condition such as fluid turbulence. The testing was done for three different lengths of the shaft, during which one blade that is equipped with a strain gauge was excited by the shaker and the response of the rotor system was measured via the strain gauges and the accelerometers.

The results obtained were analyzed in the frequency spectrum domain, as extracted from Fast Fourier Transform (FFT), and were compared to the mode shapes and system natural frequencies generated by *ANSYS* using FE Analysis. The study revealed that torsional vibrations of the shaft correlate to blade-bending natural frequencies, particularly at low frequencies, more than the lateral vibrations. In summary, this study supports extracting blade vibrations signature from shaft torsional vibration analysis only.

Adewusi [14] studied experimentally the impact of blade faults on the lateral vibrations of rotor assembly considering rotation effect. The test rig used by Adewusi consists of a shaft driven by a DC motor, single disk with six blades attached in an over-hung configuration, two roller elements bearing with two accelerometers mounted at one bearing housing to measure the lateral vibrations of the rotor.

In order to evaluate the contribution of the defective blade on the coupled shaft-disk-blade response, Adewusi used a modal testing approach through impact testing to identify the natural frequencies of the blades. Corresponding numerical analysis of the mode shapes and the blade theoretical natural frequencies was conducted using *ANSYS* via FE analysis. In the experiment, Adewusi simulated three different blade faults (broken, bent and twisted blade) with the aim to define a distinctive signature of blade vibrations on the rotor lateral vibrations. Each defective blade was tested at constant rotational speed with five healthy blades attached to the disk. Along with results of modal testing, the results of the three test-

runs were compared, in frequency domain, to the results of a test-run of six healthy blades to understand the effect of each blade-defect mode on the vibration response.

The results of Adewusi [14] revealed that attempt to match the isolated blade modal frequencies to the shaft-disk-blade coupled frequencies in rotation is not useful, since blade dynamical characteristics were minimal compared to the overall coupled system characteristics. Nevertheless, by comparing the magnitudes of frequency content at healthy-blades-rotor test-run with those of defects blades, Adewusi was able to identify some distinctive features. The twisted blade resulted in a decrease in the amplitude of the first two resonance frequencies and an increase in the amplitude of the synchronous frequency corresponding to the running speed. The opposite impact was noticed in the case of bent blade, whereas the broken-blade test results showed an increase in the amplitude of the first two resonance speed as well as the synchronous frequency corresponding to the running speed.

Hui Ma, et al. [15] developed a dynamic model of a rotor-blade system that describes the coupling between shaft-lateral deflection and the deflection of the blades. The model accounts for the gyroscopic effect of the rotor, the stiffening effect, softening and Coriolis forces of the blades. The blades were modeled as Timoshenko beams, while the shaft and the disk were modeled as lumped mass parameters connected with massless springs of lateral and torsional stiffness.

Hui Ma, et al. [15] derived the equation of motion of the system using Hamilton principle. To validate the accuracy of the model, the authors compared the model with a FE model and experimental data. The comparison with the FE model was done on the modal natural frequencies including the effect of rotation, whereas the comparison with the experimental

setup was done on the modal analysis at static condition as obtained from the Frequency Response Function (FRF) generated by impact testing.

Using *ANSYS*, Hui Ma, et al. [15] modeled the shaft as 14 Timoshenko beams with 15 nodes, each with 5 degrees-of-freedom (DOF). The disk was modeled as a lumped mass suppressed at one node and connected rigidly to the shaft. The 4 blades were also modeled as Timoshenko beams, 4 at each blade with 5 nodes. The blades were connected to the disk by sharing nodes. The gyroscopic effect on the shaft and the disk, as well as the centrifugal stiffening and spin softening effect on the blades were both considered on two different models in *ANSYS*, due to software limitations. The results of the model agreed well with the FE model and the experimental data validating the accuracy of the model. In addition, the authors observed that the coupling between the blade-bending and the shaft-lateral vibration is more pronounced with increased number of blades.

Santos, et al. [16] studied the interaction between blades motion and shaft lateral vibrations using a simple spring-mass system. The developed mathematical model considered only the horizontal lateral deformation of the shaft and used Euler-Bernoulli beam theory to represent the blades. Neither Gyroscopic effect due to angular vibrations of the rotor, shear forces, nor beam distributed masses were taken into consideration. Three models were considered in the study; linear model, second-order linearized modal and fully non-linear model. That was established by assuming small blade deformation, large blade deformation and non-linear blade deformation respectively. The system equation of motion was developed using Newton-Euler-Jourdain's formulation.

Santos, et al. [16] used an experimental test-rig to validate their three developed model. The rig consists of a rotating disk attached to a motor fixed on rigid foundation. The

foundation is supported by beams of adjustable lengths, which can be configured as adjustable springs. This configuration eliminates the effect of gyroscopic moment as only linear motion of the rotor center is allowed. Four blades with tip masses were attached to the rotating disk. The vibration signal was measured using accelerometers attached to the rig foundation. The testing in this study was done by running the disk on various rotational speeds and acquiring the vibration response due to unbalance of the blades. In addition, the foundation of the rig was excited via a shaker to obtain the impact response of the system at different rotational speeds including static condition, which helps illustrating the coupling modes between the blades and the shaft.

Analyzing the testing results using frequency spectrums generated by FFT and waterfall diagrams, Santos, et al. [16] found that only the second order linearized model along with the non-linear model were able to match the experimental setup. The authors also noted that the lighter the fixable blades are, the closer the coupling modes (blade-blade and shaft-blade) will be to each other in the frequency domain. Therefore, careful acquisition time setting is needed to precisely identify both frequencies and modes during testing.

Anegawa et al. [17] investigated the shaft-blade coupled bending vibration for the in-plane and out-of-plane cases due to resonance experimentally. They conducted the experiment on a rotor kit that consists of a shaft, a set of 8 flat blades that could be mounted circumferentially either in-plane or out-of-plane fitted to a rigid disk that is fitted to the shaft, one ball bearing and one Active Magnetic Bearing (AMB) to support the rotor in a between-bearing configuration and also provides excitation means. The rotor was driven by a synchronous motor with variable speeds. The shaft lateral vibration measurements

were collected with the aid of proximity probes mounted on the AMB, whereas the blades vibrations were collected with strain gauges mounted at blades roots.

By analyzing the results using Campbell diagrams, Anegawa et al. [17] observed interesting phenomena. First, when the rotor is excited at a speed equal to the difference between the blade natural frequency and the shaft natural frequency, resonance of the entire rotor-system with high amplitude occurs in the in-plane and out-of-plane condition. Second, the response of the rotor-system in the out-of-plane case exhibited elliptical whirl owed to shaft unbalance in addition to self-induced vibrations attributed to fluid forces, similar observations were not noticed in the in-plane case.

Chao-Feng et al [11] studied the impact of shaft bending on the coupling vibrations of a flexible blade-rotor mathematically. More specifically, the authors investigated the effect of the number of blades, the position of the disk and the speed of the rotor on the coupled blade-rotor vibrations of the system. The developed model consists of a continuous shaft and a rigid disk with blades. Using the Euler-Bernoulli beam model, the mathematical model of the rotor system was developed using assumed mode method. Upon analyzing the resultant modes of the first two-order rotor natural frequencies, the authors concluded that the shaft-blade mode shapes cannot be easily distinguished from the blade-blade (BB) coupled vibrations. They also found that the modes of blade have no effect on the deformation of rotor, whereas vice versa is true. The authors also noticed that the number of blades does not significantly impact the coupled rotor-blade vibrations. In addition, the authors realized that the position of the disk, overhung or mid-way between bearing, along with the rotation speed directly impacted the shaft vibrations, which in turns impacted the coupled vibrations of the system significantly.

Using the same rotor geometry and configuration in [12] Hou-xin et al [13] studied the effect of shaft and disk flexibility on the coupled disk-blade vibrations with shaft bending vibrations of rotor system. The shaft was intentionally made relatively long, more flexible, to better express the effect of shaft flexibility on the coupled system vibrations. The shaft was modeled using Timoshenko beam whereas the disk was modeled as flexible element. The blades were modeled as cantilever beams using Euler-Bernoulli beam theory. Considering shaft torsion, disk transverse and blade bending displacement, the authors used Lagrange principle to generate the equation of motion of the system. The solution to the equation, mode shapes, were evaluated by FE method after using power series formulation of the mode shapes using Bessel method.

Upon interpreting of the results, Hou-xin et al [13] realized that with rigid shaft, the coupled shaft-disk-blade (SDB) modes are negligible and the predominant coupling modes are transverse-disk-blade (TDB), disk-blade (DB) and blade-blade (BB) modes. As shaft flexibility increases, the repeated DB modes transfers into SDB which couples with the disk and blade vibrations at the first diametral nodal mode of the disk only.

Considering shaft bending flexibility, Hou-xin et al [13] found that for their selected material properties, 0.1m shaft length was a threshold of bending rigidity, below which the effect of the coupled system vibrations on the shaft bending is negligible. In addition, they found that the shaft-disk-blade bending frequencies as well as the disk transverse-blade frequencies decreases significantly with the increase of shaft bending flexibility. As for disk transverse flexibility, Hou-xin et al [13] found that as the flexibility increases, more coupled mode shapes start to appear but the blade-disk-shaft bending mode does not get affected drastically. They also found that further increasing the transverse flexibility of the

disk will cause large deformation in the disk affecting its vibrations symmetry in the vertical and horizontal vibrations.

Okabe et al [12] proposed a method to evaluate the coupled vibrations of a shaft-blade turbine system through the analysis of the system Eigen-frequencies. In this study, the authors modeled the blades as single-mass-points attached to the disk via springs. Lagrange equation with mixed-inertial reference frame was used to construct the equation of motion governing the coupled vibrations. The blades system was modeled using a rotating reference frame whereas the shaft was modeled using a fixed reference frame and superposition principle was applied to combine the two models using FE method.

The equation of motion was solved using a tracking solver method to obtain the Eigen-frequencies. By analyzing the results using Campbell diagram, Okabe et al [12] concluded that the blades vibrations increase significantly when the blade frequency and the shaft frequency get close to each other. The authors also identified the frequencies and the speeds at which strong coupling between shaft and blade occurs on the vibration signal.

Bachschnid et al [5] studied the influence of the shaft lateral vibrations on the last stage row blades vibration of a low-pressure steam turbine. Their objective was to develop a 3-D FE model of the row blade dynamics that can be coupled with bare shaft models and be used in general purpose FE software. In the study, the simulated two different excitation means, unbalance excitation to the shaft and fluid flow random excitation to the blades. The shaft bending vibration response was measured at the bearing at both conditions. The results of the study demonstrated that at shaft unbalance excitation, the blade resonance vibrations were not coupled with the shaft bending nor torsional vibrations as only a phase change was noticed at the vibration measurement points (on the bearings). On the contrary,

the response to the fluid flow blade excitation showed that resonance condition of the blade row caused a peak in blade row frequencies at the shaft lateral vibration measurement collected at the bearing.

The presented studies this far considered single disk rotors. However, there are several published studies that considered multi-stage rotors as well [18-22]. Rzadkowski and Drewczynski [18] investigated the resonance condition and coupling effect of multi-stage shaft-disk-blade industrial rotor. The rotor model was simplified geometrically. Six out of the eight rectangular, twisted and staggered blades were shrouded and the rotor was simulated in vacuum condition and excited via air jet. FE method was applied via *ANSYS* to calculate the forced and free vibration response of the rotor including the spinning and gyroscopic moment effect. The authors found that the shaft bending effect was pronounced up to the two nodal diameter modes of the disk, where the effect in zeroth and first nodal diameter mode was more visible than then second nodal diameter mode. Also, the effect of shaft bending was more visible on the shrouded blades when compared to the non-shrouded ones. The results, in terms of natural frequencies, were then validated by an experimental setup and found in agreement.

In summary, the presented studies support that dynamics coupling exists among the blades, the disk and the shaft in rotors. In cases where those elements are flexible, and the rotor speed is relatively high, such coupling modes are pronounced. This notion is promising as it avails the possibility of detecting blade fault vibrations through shaft bending dynamical analysis.

2.3. Blade faults detection techniques

Gubran [23] reviewed the different in-situ vibrations measurement techniques to detect blade faults in turbomachinery. He classified those measurement into three categories: (1) stationary testing which addresses the natural frequencies of blades through modal testing, (2) dynamic testing which addresses the blade natural frequencies under centrifugal loads, and (3) in-service testing which addresses the blade natural frequencies while the machine is in operation.

The in-service measurement techniques can be further broken down into direct and indirect techniques. Direct measurement techniques are those at which the measuring instrument is directly attached or is directly reading the vibrations of the blades such as strain gauges, laser doppler and optical methods. Whereas the indirect techniques are when the instrument is not directly reading the vibrations of the blade such as picking up the signal from the casing, bearing pedestals or the rotor and then analyze the data to interpret blades vibrations.

According to Gubran [23], strain gauges are the least intrusive among the direct measurement techniques. They offer the advantage of reading the local deformation for an individual blade, or disk. On the contrary, they come with several disadvantages due to their exposure to harsh environment, such as the high temperature in gas turbine, as they are mounted on the surface of the blade. This introduces signal error, shorten the gauges lifespan and makes it hard to access the gauges and transmit the collected signals. The authors of [24-27] reviewed extensively the usage, applications, and limitations of strain gauges in monitoring blades vibrations.

Blade tip timing is another direct vibration measurement technique that relies on optical sensors, capacitance, eddy current or similar sensors to measure blade vibrations [23]. This technique works by measuring the time interval of a blade tip as it passes by the probe. This time measurement can then be used to evaluate useful blade dynamic parameters such as the natural frequencies, time and angle of arrival. Nevertheless, they also have the disadvantage of being exposed to harsh environment. In addition, their accuracy might be jeopardized if the sensor is blocked by particles, the blade tip gets deformed or scratched during operations or incorrect spacing was done during installation. The authors of [28-32] discussed thoroughly the usage, applications, advantages and disadvantages of Blade tip timing technique in measuring blade vibrations.

The indirect techniques involve collecting the relative vibration signal of the shaft or the absolute vibrations signal of the bearing pedestals or the casing to deduce blades vibrations. The raw vibration signal in this technique usually relates to either shaft torsional or lateral vibrations. Shaft torsional vibrations are picked up via means similar to the indirect blade vibrations measurement such as the instantaneous angular speed signal that gets collected by an encoder [23]. Such signal can be translated into shaft torsional vibrations. The more commonly extracted signal in this technique is the shaft lateral vibrations, where the signal is extracted by proximity probes that measures the relative lateral motion of the shaft, or accelerometers that measures the absolute lateral motion of the shaft or the casing [33]. While indirect techniques do not have the advantages of directly measuring the deformation of the blade, they have the advantages of being less intrusive, less expensive and easier to access and transfer signals, which makes them more favorable for the practical use [23]. This is in addition to the fact that shaft vibration monitoring through similar

techniques is already widely used in many industrial sectors involving operation of rotating machines [14]. Industrial practices and guidelines to control machinery vibrations through such techniques have already been established in this regard [34].

2.4. Proposed Research

Upon reviewing the recent relevant studies concerning blade defect detection, it is noted that using shaft torsional vibrations to monitor blade's health is feasible but can be used in limited cases. On the contrary, shaft lateral vibrations measurement techniques are widely adopted in the industrial sectors, yet detecting blade health using shaft lateral vibrations has not been explored. Therefore, the intention of this study is to investigate the feasibility of using shaft lateral vibrations to detect defects in blades through modal and harmonic analyses. Toward this goal, we propose to achieve the following:

- 1- Develop a numerical model, using *ANSYS* finite-element package, to simulate the dynamics of a rotor with a single bladed-disk, while considering three types of blade defects (broken, pitted - blade with holes - and bent blades).
- 2- Validate the accuracy of the mathematical model via comparisons with numerical results from the literature.
- 3- Present benchmark insights on the influence of each blade defect on the shaft lateral vibrations through modal and harmonic analyses.

CHAPTER 3

ELASTODYNAMIC MODEL

This chapter addresses the theory underlying the analysis in this research starting from the description of the system under study and modeling approach, all the way to expressing the dynamic equations governing the motion of the model.

3.1. Introduction

The studies of rotating-structure dynamics typically involve the development of appropriate mathematical models. The objective of such models is to transform the physical complexity of rotating structure into simplified representative dynamic parameters that can aid the design and analysis of structure-vibrations. Rotors are rotating structures that generally consist of a shaft, a disk and support bearings. In the dynamic studies of rotors, also called *Rotordynamics*, parameters such as critical speeds and modes of vibrations are of particular importance. The research in the field of *Rotordynamics* evolved over a span of 140 years [35]. The early works of research treated rotors as rigid bodies using the lumped-parameter assumption, where rotors were modeled as a single mass-spring system with limited Degrees of Freedom (DOF). With the modern designs of lightweight, high-speed rotors, such analysis is no longer sufficient as rotors no longer behave as rigid bodies, but continuous-flexible systems of multi DOF.

In contrast to the rigid-body model, mathematical models of a continuous rotor are complex and involve multi DOF. Continuous systems of such complexity cannot be oftentimes solved analytically. Hence, numerical methods must be deployed to obtain solution to such systems and FE analysis is a powerful candidate. In fact, FE analysis has been heavily deployed in the this filed of research as a primary tool to facilitate constructing and solving mathematical models of continuous rotors with multi DOF.

In a typical continuous rotor, the shaft is modeled as flexible beam element with 6 DOF; two lateral displacements, one axial displacement and three rotations around each axis in a Cartesian 3-D space. Shafts are essential elements of rotors and they contribute to the kinetic and potential energy of rotors through their inertia and elasticity, respectively. Rotating disks are cyclic structures with relatively short axial length and large diameters. They are also modeled with a 6 DOF element and generally contribute more to the rotor kinetic energy due to their minimal strain energy variation. That is unless the disk is considered flexible, in which case it also contributes significantly to the rotor potential energy. Bearings provide structural support to the entire rotor and they typically influence the rotor stiffness and govern the boundary conditions. This chapter lays out the elastodynamic foundation of the shaft, disk and blades to be used in the formulation in the FE model.

3.2. System Description and Modeling Approach

The SDB rotor model under study in this research is depicted in Figure 3.1.

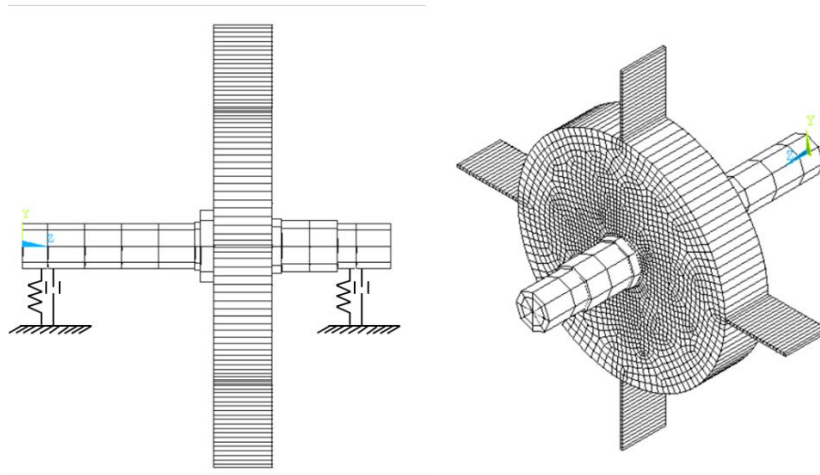


Figure 3.1. Schematic of the studied rotor in this work.

The shaft consists of multiple spools of varying cross-sections. The blades are evenly distributed around the disk and have the same transverse thickness as the disk. The rotor is supported by two ball bearings and is rotating around a global axis of rotation passing through the centerline of the shaft. This rotor model is inspired by the model used in [36] and has been adopted, with some modification to blade geometry, to enable model validation and increase the reliability of the results. The following general assumptions are considered while developing the FE model,

- 1- The material properties of the shaft, disk and the blades are isotropic,
- 2- The shaft and blades are modeled based on Timoshenko beam theory,
- 3- The cross-sectional properties of each element are constant along the axial direction,

- 4- The disk is rigidly connected to the shaft while the blades are connected to the disk via sharing nodes,
- 5- The bearings are identical, isotropic and are simulated ideally using linearized stiffness and damping characteristics,
- 6- The longitudinal displacement along the shaft axis is constrained,
- 7- Material damping and fluid-elastic forces are neglected.

The FE model, resembled by the governing global equations of motion, is typically developed for such systems based on energy method and Lagrange equation. Numerical methods are used to solve the mathematical model through the use of FE software such as *ANSYS* Parametric Design Language (*APDL*). The FE model is first verified by comparing it to the original model published in the literature via modal analysis results comparison. Upon successful comparison with the literature, the model is further validated by analyzing the effect of blade addition on the modal results. Once the model is fully validated, the following test cases are simulated to investigate the effects of blade defects on the rotor's overall vibrations and, specifically, shaft lateral vibrations,

- 1- Broken Blades
- 2- Pitted Blades (Blade with holes)
- 3- Bent Blades

Modal analysis including rotation and harmonic analyses with unbalance excitation are conducted for each case. The obtained results are benchmarked with baseline results established for a healthy shaft to track and highlight trends, vibrations-coupling features and significant findings of each defect case on the rotor's vibrations.

3.3. Shaft Element

3.3.1 Velocity Vector

Analysis of continuous rotating shafts is based on classical beam theory. The most fundamental beam model is based on the Euler-Bernoulli- beam theory which assumes that the cross section of a shaft remains perpendicular to the shaft centerline during vibrations [35]. This assumption essentially results in the shear forces and rotatory inertia effect on the shaft being negligible. Euler-Bernoulli beam theory is suitable for the analysis of cylindrical-shaped beams with low diameter-to-length ratios. As the diameter-to-length ratio increases, the effect of rotary inertia and shear forces on the shaft becomes significant. A more accurate model of the rotor in such cases would be based on the Timoshenko beam theory. The evaluation of shaft element in this section is based on the Timoshenko beam theory and is following the work done in [37].

Considering the beam element seen in Figure 3.2, let the Cartesian coordinate system, XYZ , be the fixed inertial reference frame of the system. The beam deforms as it rotates. Hence, the coordinate $X^i Y^i Z^i$ is defined to denote the element coordinate at undeformed state and $x^i y^i z^i$ is defined to denote the element coordinate at deformed state. Considering an arbitrary point p^i on the undeformed element, which then can be transformed into the point p at the deformed element, we can define the following position vector,

$$\bar{r}_p = \bar{R} + \bar{r} \quad (3.1)$$

$$\bar{r} = \bar{r}_0 + \bar{u} \quad (3.2)$$

where \bar{u} is the deformation vector.

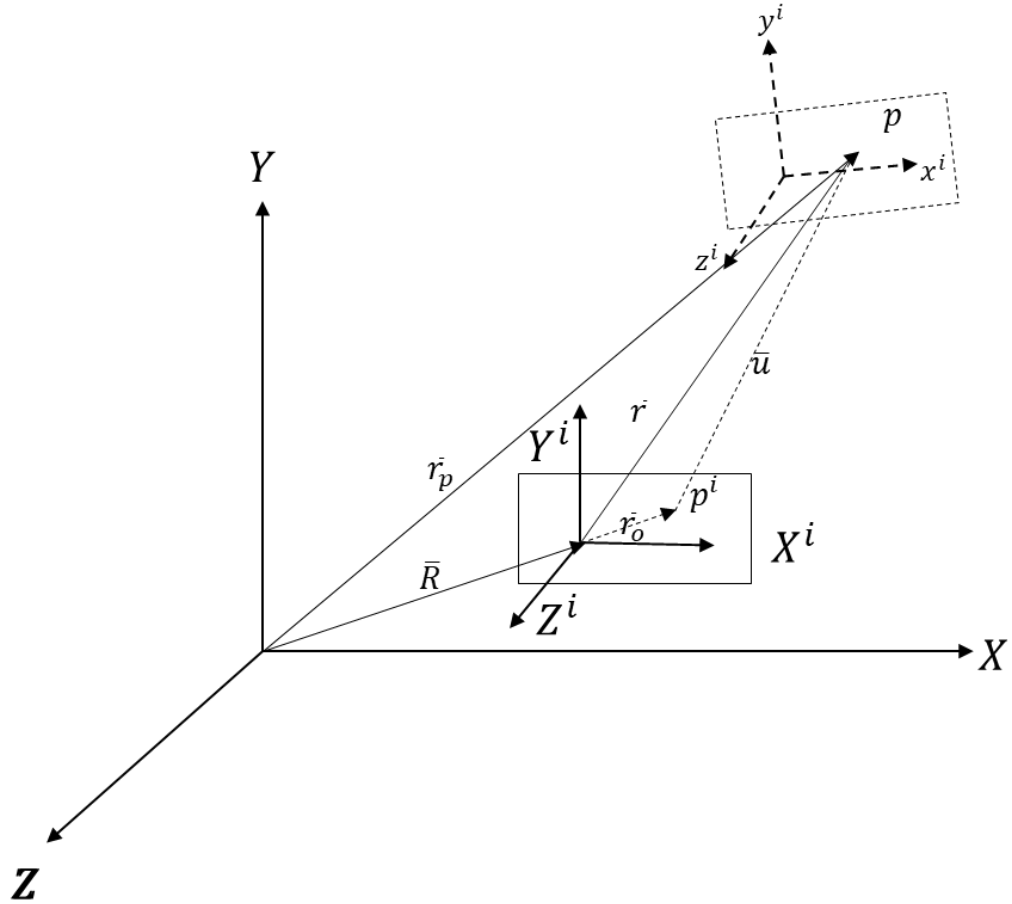


Figure 3.2 Shaft element cross sectional orientation.

The xyz -coordinate is related to the XYZ -coordinate through the angles, φ , θ_y and θ_z . As the element rotates around the x -axis with angular displacement Ω , the element cross-section orientation after deformation can be obtained by applying the appropriate coordinate transformation as seen in Figure 3.3. First, the element is rotated by an angle of $(\Omega + \varphi)$ around the X -axis. Then the element is rotated around the new- y -axis, denoted by y_2 , by θ_y . Lastly, the element is rotated around the final z -axis by θ_z .

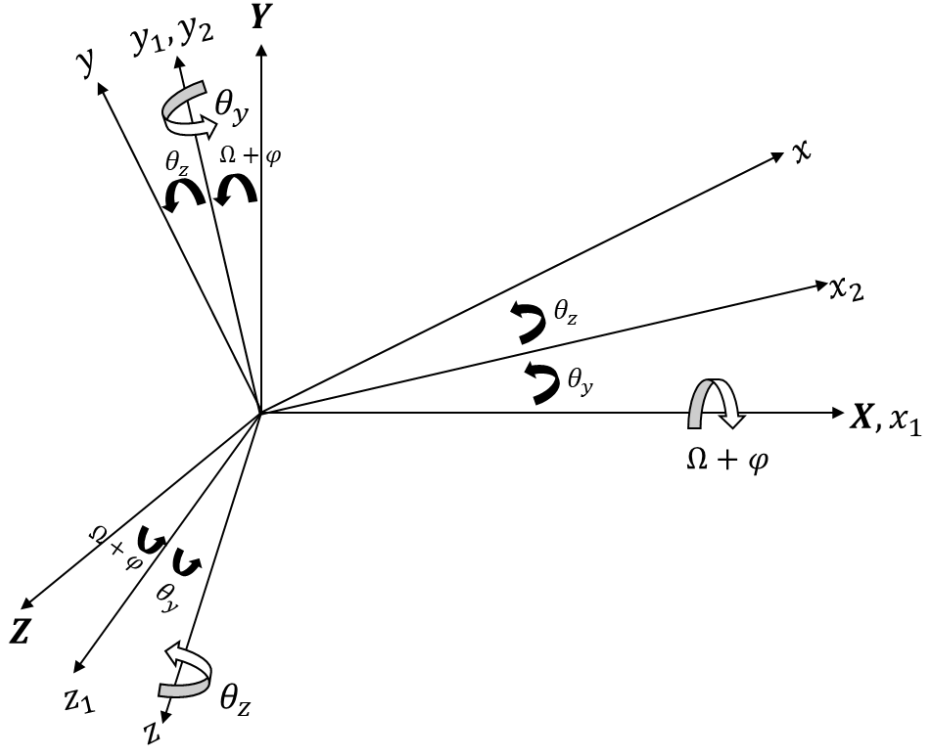


Figure 3.3. Rotation angles of shaft element cross section.

The instantaneous angular velocity vector of the resultant $x^i y^i z^i$ can now be expressed as the following,

$$\bar{\omega} = (\dot{\Omega} + \dot{\varphi})\hat{I} + (\dot{\theta}_y)\hat{j}_1 + (\dot{\theta}_z)\hat{k}_2 \quad (3.3)$$

where $\dot{\Omega}$ is the beam angular velocity. Transforming the velocity vector in Equation (3.3) into the global coordinate system xyz , we obtain the following,

$$\bar{\omega} = (\dot{\Omega} + \dot{\varphi})\hat{I} + \dot{\theta}_y[\cos(\Omega + \varphi)\hat{j} + \sin(\Omega + \varphi)\hat{K}] + \dot{\theta}_z[-\sin(\theta_y)\hat{I} - \sin(\Omega + \varphi)\cos(\theta_y)\hat{j} + \cos(\theta_y)\cos(\Omega + \varphi)\hat{K}] \quad (3.4)$$

Assuming small deformations in accordance with the linear theory of elasticity, small angles approximation can be invoked to rewrite Equation (3.4) as the following,

$$\begin{aligned}\bar{\omega} = & (\dot{\Omega} + \dot{\varphi})\hat{I} + \dot{\theta}_y[\cos(\Omega + \varphi)\hat{J} + \sin(\Omega + \varphi)\hat{K}] + \\ & \dot{\theta}_z[-\theta_y\hat{I} - \sin(\Omega + \varphi)\hat{J} + \cos(\Omega + \varphi)\hat{K}]\end{aligned}\quad (3.5)$$

Simplifying the expression in Equation (3.5) and rewriting it in matrix form,

$$\bar{\omega} = \begin{Bmatrix} \omega_x \\ \omega_y \\ \omega_z \end{Bmatrix} = \begin{Bmatrix} \dot{\Omega} + \dot{\varphi} - \dot{\theta}_z\theta_y \\ \dot{\theta}_y \cos(\Omega + \varphi) - \dot{\theta}_z \sin(\Omega + \varphi) \\ \dot{\theta}_y \sin(\Omega + \varphi) + \dot{\theta}_z \cos(\Omega + \varphi) \end{Bmatrix}\quad (3.6)$$

To obtain an expression for the velocity of the point p , we differentiate the position vector \bar{r}_p with respect to time as the following,

$$\frac{d\bar{r}_p}{dt} = \dot{\bar{r}}_p + \bar{\omega} \times \bar{r}_p = \dot{\bar{r}}_p + [\tilde{\omega}]\{r_p\}\quad (3.7)$$

where

$$[\tilde{\omega}] = \begin{bmatrix} 0 & -\omega_z & \omega_y \\ \omega_z & 0 & -\omega_x \\ -\omega_y & \omega_x & 0 \end{bmatrix}\quad (3.8)$$

Using the finite element method, the position vector of the point p , can be expressed as,

$$\bar{u} = \{u\} = [N]\{q\}\quad (3.9)$$

where $[N]$ is the shape function matrix, which will be discussed in Chapter 4, and $\{q\}$ is the nodal coordinates vector (also called generalized coordinates vector). Taking advantage of the fact that there is no change in the magnitude of the vectors \bar{R} and \bar{r}_0 when the beam deforms, Equation (3.7) can be rewritten as,

$$\frac{d\bar{r}}{dt} = [N]\{\dot{q}\} + [\tilde{\omega}]\{r_p\} = [N \quad \tilde{\omega}]\begin{Bmatrix} \dot{q} \\ r_p \end{Bmatrix} \quad (3.10)$$

3.3.2 Kinetic Energy of Shaft Element

The kinetic energy of a spinning beam element can be expressed by the following integral,

$$T = \frac{1}{2} \int_V \rho \left\{ \frac{dr_p}{dt} \right\}^T \left\{ \frac{dr_p}{dt} \right\} dV \quad (3.11)$$

or simply as,

$$T = \frac{1}{2} \int_V \rho \begin{bmatrix} \dot{q}^T & r_p^T \end{bmatrix} \begin{Bmatrix} N_v^T \\ \tilde{\omega}^T \end{Bmatrix} \begin{bmatrix} N_v & \tilde{\omega} \end{bmatrix} \begin{Bmatrix} \dot{q} \\ r_p \end{Bmatrix} dV \quad (3.12)$$

where T is the kinetic energy for the beam element, V is the volume of the element and ρ is the mass density of the element. The kinetic energy can be expressed in matrix format as,

$$T = \frac{1}{2} \int_V \rho \left[\{\dot{q}\}^T [N_v]^T [N_v] \{\dot{q}\} + \{\dot{q}\}^T [N_v]^T [\tilde{\omega}] \{r_p\} \right. \\ \left. + \{r_p\}^T [\tilde{\omega}]^T [N_v] \{\dot{q}\} + \{r_p\} [\tilde{\omega}]^T [\tilde{\omega}] \{r_p\} \right] dV \quad (3.13)$$

The first and last terms in Equation (3.13) are due to the translational and rotational kinetic energies of the beam, respectively. The second and third terms can be set to zero if moment of inertia are calculated with respect to the element center of mass.

To evaluate the rotational energy term, the following expression may be used,

$$[\tilde{\omega}]^T [\tilde{\omega}] = \begin{bmatrix} \omega_z^2 + \omega_y^2 & -\omega_x \omega_z & -\omega_z \omega_x \\ -\omega_x \omega_y & \omega_z^2 + \omega_x^2 & -\omega_y \omega_z \\ -\omega_x \omega_z & -\omega_y \omega_z & \omega_y^2 + \omega_x^2 \end{bmatrix} \quad (3.14)$$

This will yield a rotational kinetic energy term that can be expressed as,

$$\frac{1}{2} \int_V \rho \{r_p\} [\tilde{\omega}]^T [\tilde{\omega}] \{r_p\} dV = \frac{1}{2} \int_0^l \rho (I_x \omega_x^2 + I_y \omega_y^2 + I_z \omega_z^2) dx \quad (3.15)$$

where I is the cross-sectional area second moment of inertia of the beam and l is the length of the beam along the axis of rotation. Substituting Equation (3.6) back in Equation (3.15) and simplifying we get,

$$\begin{aligned} \frac{1}{2} \int_V \rho \{r_p\} [\tilde{\omega}]^T [\tilde{\omega}] \{r_p\} dV &= \frac{1}{2} \int_0^l I_p \dot{\Omega}^2 dx + \int_0^l I_p \dot{\phi}^T \dot{\phi} dx \\ &+ \int_0^l I_p \dot{\Omega} \dot{\phi} dx - \int_0^l I_p (\dot{\Omega} + \dot{\phi}) \dot{\theta}_z^T \theta^y dx + \int_0^l I_D \begin{Bmatrix} \dot{\theta}_y \\ \dot{\theta}_z \end{Bmatrix}^T \begin{Bmatrix} \theta_y \\ \theta_z \end{Bmatrix} dx \end{aligned} \quad (3.16)$$

where

$$\rho I_y = \rho I_z = I_D \quad \text{and} \quad \rho I_x = I_p \quad (3.17)$$

3.3.3 Strain Energy of Shaft Element

The strain energy of a beam element can be derived by first defining the deformation of the beam cross-section. A cross section that is arbitrary located x -distance from the shaft endpoint or the blade root in a deformed state can be described by a set of translations and small rotations. Neglecting axial deformation, two translation motions can be defined, v and w along the Y - and Z -axis respectively to describe the bending and shear contribution to the deformation. The two-translation motions are defined as,

$$v(x, t) = v_b(x, t) + v_s(x, t) \quad (3.18)$$

$$w(x, t) = w_b(x, t) + w_s(x, t) \quad (3.19)$$

Where the subscript ' b ' denotes bending and the subscript ' s ' denotes shear.

Three small rotations can be defined to describe the motion of the element cross section as it deforms. $\theta_y(x, t)$ and $\theta_z(x, t)$ about the X - and y_2 - axes denote the rotations due to bending. $\varphi(x, t)$ around the z - axis denotes the rotations due to torsion. The elastic rotations are related to bending deformation by the following relationship,

$$\theta_y(x, t) = -\frac{\partial w_b(x, t)}{\partial x} \quad (3.20)$$

$$\theta_z(x, t) = \frac{\partial v_b(x, t)}{\partial x} \quad (3.21)$$

The strain due to bending is given by,

$$\varepsilon = -y \frac{\partial^2 v_b^*}{\partial x^2} - z \frac{\partial^2 w_b^*}{\partial x^2} \quad (3.22)$$

The strain energy expression of the beam can be written as the following,

$$U_b = \frac{1}{2} \int_V \varepsilon^T \sigma dV \quad (3.23)$$

where σ is the stress on the cross-section. Deploying the stress-strain relationship $\sigma = E\varepsilon$,

Equation (3.23) can be rewritten as,

$$U_b = \frac{E}{2} \int_V \varepsilon^T \varepsilon dV = \frac{E}{2} \int_V \varepsilon^2 dV \quad (3.24)$$

Substituting the expression in Equation (3.23) back in Equation (3.24),

$$\begin{aligned} U_b &= \frac{E}{2} \int_0^l \int_A \left(-y \frac{\partial^2 v_b^*}{\partial x^2} - z \frac{\partial^2 w_b^*}{\partial x^2} \right)^2 dA dx \\ &= \frac{E}{2} \int_0^l \int_A \left[y^2 \left(\frac{\partial^2 v_b^*}{\partial x^2} \right)^2 + 2yz \frac{\partial^2 v_b^*}{\partial x^2} \frac{\partial^2 w_b^*}{\partial x^2} + z^2 \left(\frac{\partial^2 w_b^*}{\partial x^2} \right)^2 \right] dA dx \end{aligned} \quad (3.25)$$

Due to the symmetry of the structure, the integral of the third term will go to zero. Using the following inertia expressions,

$$I_z = \int_A y^2 dA \quad \text{and} \quad I_y = \int_A z^2 dA \quad (3.26)$$

The strain energy due to bending can be ultimately rewritten as,

$$U_b = \frac{E}{2} \int_0^l \left[I_z \left(\frac{\partial^2 v_b^*}{\partial x^2} \right)^2 + I_y \left(\frac{\partial^2 w_b^*}{\partial x^2} \right)^2 \right] dx \quad (3.27)$$

Moving to the strain energy of the beam due to shear forces, we start by defining the shear strain along the X - Z plane as the following,

$$\gamma_{xz} = \frac{\partial w^*}{\partial x} - \frac{\partial v_b^*}{\partial x} \quad (3.28)$$

$$\gamma_{xy} = \frac{\partial v^*}{\partial x} - \frac{\partial v_b^*}{\partial x} \quad (3.29)$$

and from constitutive relationships, the shear stress can accordingly be defined as,

$$\tau_{xz} = kG\gamma_{xz} \quad (3.30)$$

$$\tau_{xy} = kG\gamma_{xy} \quad (3.31)$$

where G is the shear modulus which is defined as,

$$G = \frac{E}{2+(1+\nu)}; \quad (3.32)$$

where ν is the Poisson's ration and k is the shear factor which differs based on the cross-section shape. Similar to the bending strain energy, the strain energy expression due to the shear deformation can be written as,

$$U_s = \int_V (\tau_{xy} \gamma_{xy} + \tau_{xz} \gamma_{xz}) dV \quad (3.33)$$

$$U_s = \frac{1}{2} \int_V kG(\gamma_{xy} + \gamma_{xz}) dV = \frac{1}{2} \int_0^l \left\{ kGA(x) \left[\left(\frac{\partial v^*}{\partial x} - \frac{\partial v_b^*}{\partial x} \right)^2 + \left(\frac{\partial w^*}{\partial x} - \frac{\partial w_b^*}{\partial x} \right)^2 \right] \right\} dx \quad (3.34)$$

The bending and shear deformation can be further expressed in terms of displacement components, v and w , using the following relationship,

$$v^* = v \cos\theta - w \sin\theta \quad (3.35)$$

$$w^* = v \sin\theta + w \cos\theta \quad (3.36)$$

Accordingly,

$$\begin{aligned} U_b &= \frac{E}{2} \int_0^l I(x) \left[\left(\frac{\partial^2 v_b}{\partial x^2} \right)^2 + I_y \left(\frac{\partial^2 w_b}{\partial x^2} \right)^2 \right] dx \\ &= \frac{E}{2} \int_0^l I(x) \left[\left(\frac{\partial \theta_y}{\partial x} \right)^2 + \left(\frac{\partial \theta_z}{\partial x} \right)^2 \right] dx \end{aligned} \quad (3.37)$$

$$U_s = \frac{1}{2} \int_0^l k G A(x) \left[\left(\frac{\partial v_s}{\partial x} \right)^2 + \left(\frac{\partial w_s}{\partial x} \right)^2 \right] dx \quad (3.38)$$

In addition, the strain energy due to torsion can be written as,

$$U_t = \frac{1}{2} \int_0^l G I_p \left(\frac{\partial \varphi}{\partial x} \right)^2 dx \quad (3.39)$$

Accordingly, the total strain energy of the beam element can be expressed as,

$$\begin{aligned} U &= \frac{E}{2} \int_0^l I(x) \left[\left(\frac{\partial \theta_y}{\partial x} \right)^2 + \left(\frac{\partial \theta_z}{\partial x} \right)^2 \right] dx \\ &+ \frac{1}{2} \int_0^l k G A(x) \left[\left(\frac{\partial v_s}{\partial x} \right)^2 + \left(\frac{\partial w_s}{\partial x} \right)^2 \right] dx + \frac{1}{2} \int_0^l G I_p \left(\frac{\partial \varphi}{\partial x} \right)^2 dx \end{aligned} \quad (3.40)$$

3.4. Blade Element

The evaluation of the kinetic, strain and potential energy of the blade elements follows, for the most part, that of the shaft element since both are modeled based on Timoshenko beam theory. The exceptions are the element cross section shape and the element orientation with respect to the rotor and therefore, the rotation axis. The evaluation of the blade element is following the work done in [37] and [38].

3.4.1 Kinetic Energy of Blade Element

Considering the blade element of length l^b seen in Figure 3.4, let the XYZ - axis be the fixed reference frame and xyz - axis be the local rotating axis with the blade around the shaft. The blade is connected to the shaft-disk assembly and rotating with a constant angular velocity, Ω , around the shaft axis of rotation. According to the Timoshenko beam theory, the deformation of the blade can be defined by a transverse displacement, $v^b(x, t)$ and $w^b(x, t)$, and a rotational displacement due to bending, $\theta_y^b(x, t)$ and $\theta_z^b(x, t)$. The mid-plane of the blade is inclined to the rotation plane with an angle Ψ , called the stagger angle. For $\Psi = 0$, the motion is confined to the y - z plane and is pure flapping. For $\Psi = \frac{\pi}{2}$, the transverse motion exists in the x - y plane and is considered pure lead-lag. Ψ in this work is made intentionally $\frac{\pi}{2}$, as seen in Figure 3.1, to establish a geometrical coupling between blade's bending vibrations and shaft bending vibrations as will be demonstrated later.

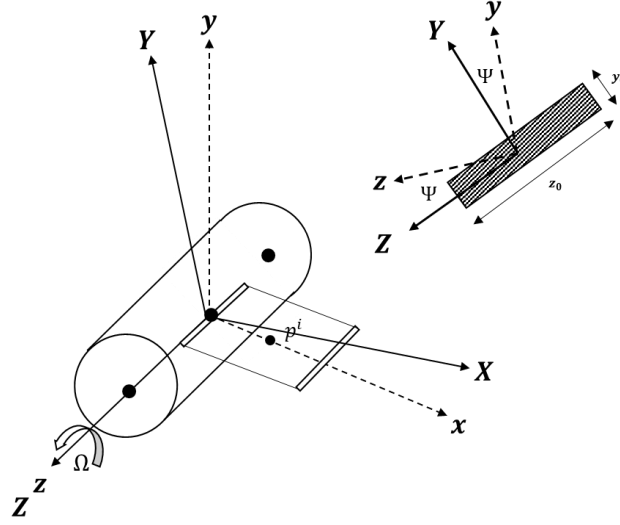


Figure 3.4. Cross section of blade element.

The kinetic energy of the blade can be evaluated in a similar manner to the evaluation done for the shaft element. However, since the rotation of the blade is now around the shaft axis, a non-spinning beam model will be adapted. According to [38], the kinetic energy of a non-spinning beam element due to translational and rotational deformation is given by,

$$T^b = \frac{1}{2} \int_0^{l^b} \mu^b A^b(x) \left(\frac{\partial v^{*b}}{\partial t} \right)^2 dx + \frac{1}{2} \int_0^{l^b} \mu^b I^b(x) \left(\frac{\partial \theta^b}{\partial t} \right)^2 dx \quad (3.41)$$

where v^{*b} is the transverse displacement of the blade (v^b and w^b). Similarly, θ^b is the total bending rotation of the blade (θ_y^b and θ_z^b). μ^b is the mass density of the blade, $A^b(x)$ is the cross-sectional area of the blade and $I^b(x)$ is the moment of inertia of the blade per unit length around the neutral axis of the blade. Unlike shaft element, the gyroscopic moment effect does not appear in the kinetic energy expression as the blade does not spin around itself.

3.4.2 Strain and Potential Energy of Blade Element

The strain energy of the rotating blade can be expressed using the following equation,

$$U_{strain}^b = \frac{1}{2} \int_0^{l^b} (E^b I^b(x) \left(\frac{\partial \theta^b}{\partial x}\right)^2 + k^b G^b A^b(x) \left(\frac{\partial v^{*b}}{\partial x} - \theta^b\right)^2 + F_C \left(\frac{\partial v^{*b}}{\partial x}\right)^2) dx \quad (3.42)$$

where E^b is the Young's modulus of elasticity of the blade, G^b is the shear modulus of elasticity of the blade and F_C is the centrifugal forces along the longitudinal axis of the blade. Since Ω is constant, the centrifugal forces are approximately constant and thus, they can be treated as axial load. The first term of Equation (3.42) reflects the flexural strain contribution, while the second terms reflects the shear strain energy contribution and the third term reflect the effects of centrifugal forces on the blade total strain energy.

The centrifugal stiffening effect has been accounted for in Equation (3.42). However, the spin-softening effect has been not. According to [38], the potential energy per unit volume variation of the beam element due to the spin-softening effect is given by,

$$U_{spin}^b = -\frac{1}{2} \int_0^{l^b} \mu^b A^2(x) \Omega^2 v^{*b^2} \sin^2 \Psi dx \quad (3.43)$$

where Ψ is the stagger angle, which is the inclination angle between the mid-plane of the blade and the axis of rotation.

3.5. Disk Element

The disk in this research is modeled as a rigid body due to its large thickness. Rigid bodies do not exhibit internal deflections. Hence, their strain energy variation is minimal. Assuming the lateral deflection (elevation) of the disk to be small, the gravitational contribution to the potential energy can be neglected as well. Thus, the disk energy contribution can be expressed entirely in terms of kinetic energy.

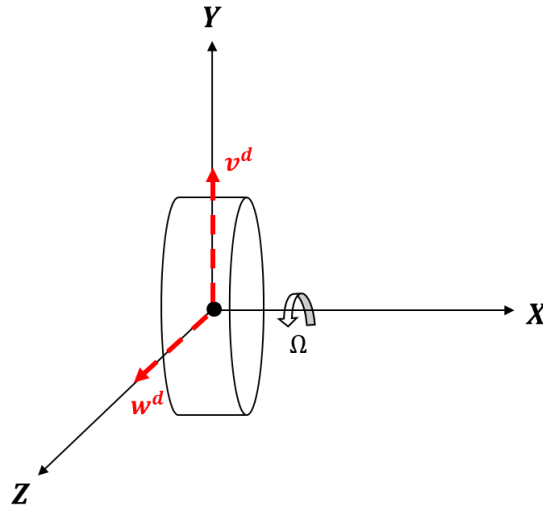


Figure 3.5. Cross section of disk.

Considering the disk cross-section seen in Figure 3.5, let v^d and w^d be the generalized coordinates of the disk center of mass in the XYZ -coordinate system. The disk only deforms in the y - z plane. The kinetic energy of the disk can be expressed following the procedure used for the shaft element using the following equation,

$$T^d = \frac{1}{2} m^d (\dot{v}^{d2} + \dot{w}^{d2}) + \frac{1}{2} I_D^d (\dot{\theta}_y^2 + \dot{\theta}_z^2) + \frac{1}{2} I_p^d (\dot{\Omega}^2 + \dot{\phi}^2) + I_p^d \dot{\phi} \dot{\Omega} - I_p^d (\dot{\Omega}^2 + \dot{\phi}^2) \dot{\theta}_z \theta_y \quad (3.44)$$

CHAPTER 4

FINITE ELEMENT MODEL

This chapter discusses the finite element procedure that is used to construct the global equation of motion of the model. The discussion in this chapter complements the analysis done in Chapter 3 and aims at describing the development of the system governing equations of motion.

4.1. Introduction

The FE analysis comes particularly handy in the analysis of flexible rotors. Through the appropriate discretization techniques, each rotor's component can be broken down into smaller, finite, elements governed by linearized interpolated functions that can be solved by numerical computations to represent the dynamics of the rotor.

Upon developing an appropriate FE model of the system, various dynamic analyses might be conducted, among which is the modal analysis. Modal analysis involves computing the system natural frequencies through uncoupling the governing equations of motion via linear coordinate transformation. This treatment yields a system of linear equations of motion that can be solved as an Eigenvalue problem to obtain the desired solution, which is resembled in this case by the system natural frequencies or mode shapes. Modal analysis is essential in *Rotordynamics* as it facilitates understanding the system response at various

running conditions. Modal analysis is typically performed at the design stage of rotating machines to aid the design-parameter selection-process.

Another useful analysis type in *Rotordynamics* is the harmonic analysis. Harmonic analysis addresses the forced response of the system when subjected to a harmonic excitation, a sinusoidal force for example, after the decay of the initial transient response. They are usually performed online – during machine operation – as a health-monitoring mean to identify abnormalities and causes of vibrations in machine operation.

Both modal and harmonic analyses are conducted in this research on a flexible Shaft-Disk-Blades (SDB) rotor system with the intention to investigate the feasibility of detecting blades' defect through the interpretation of shaft lateral vibrations.

4.2. Discretization and Shape Functions

The flexible rotor under study is discretized as seen in Figure 4.1. The shaft is modeled using 14 Timoshenko elements. The global Cartesian coordinate system XYZ has its origin at Node 0 (The left end extremity of the shaft). The blades are modeled as Timoshenko beams as well and are connected to the disk via sharing nodes. The disk is rigidly connected to the shaft at Node 9.

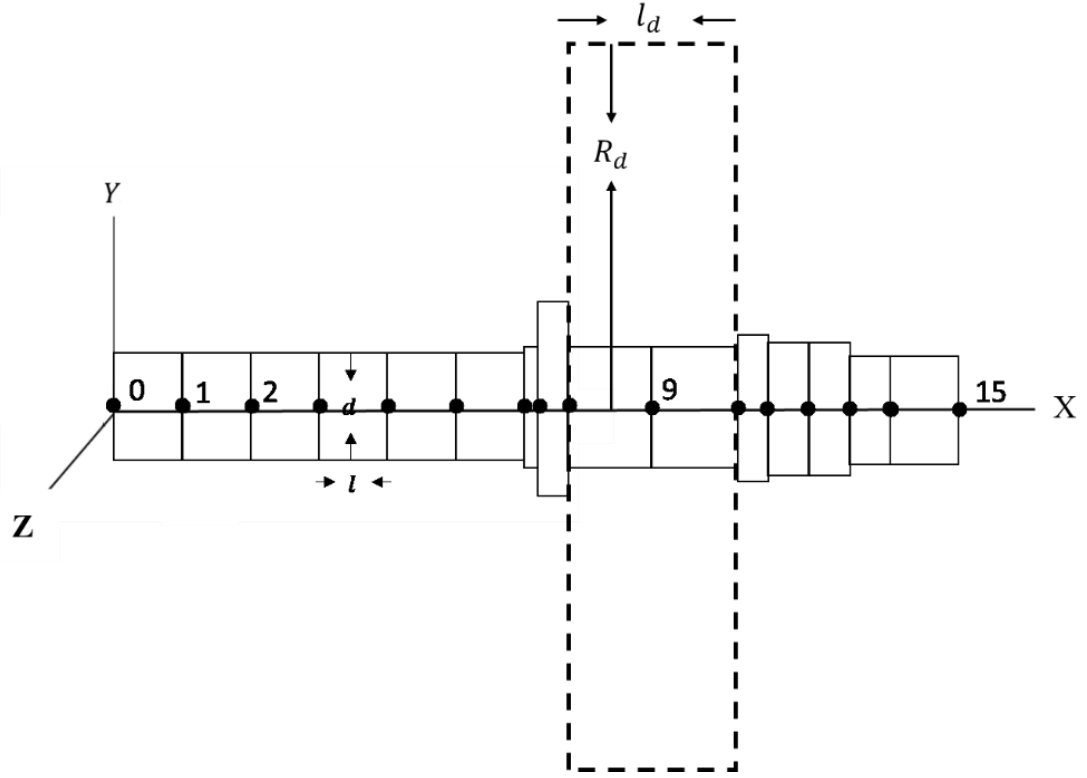


Figure 4.1. Discretized shaft of the studied rotor.

Neglecting axial deflection of shaft and blades, the nodal local generalized coordinates of the shaft, disk and blades can be defined as,

$$\{q^*\} = \begin{Bmatrix} q_1^* \\ q_2^* \\ q_3^* \\ q_4^* \\ q_5^* \end{Bmatrix} = \begin{Bmatrix} v \\ w \\ \varphi \\ \theta_y \\ \theta_z \end{Bmatrix} \quad (4.1)$$

where the subscript ‘*’ can be ‘s’, ‘b’ or ‘d’ for shaft, blade or disk elements, respectively.

The generalized coordinates at each node define the nodal displacement at that node. Nodal coordinates are sufficient to define the entire motion for the disk since it is modeled as a rigid body. However, in order to express the displacement of shaft and blade elements, interpolation functions are needed (called shape functions, $\{N\}$, in FE terminology). To

develop the shape functions in accordance with the Timoshenko beam theory, the following transverse displacement variation function is defined,

$$q(x) = a_1 + a_2x + a_3x^2 + a_4x^3 \quad (4.2)$$

The cubic displacement function is appropriate in this analysis because it is assumed that each node has five DOF only. The displacement function also satisfies the basic beam differential equation and slope continuity at shared nodes between elements. By expressing the nodal DOF across the element (two nodes) in terms of Equation (4.1) the following set of equations are obtained,

$$[N_v]\{q\} = \begin{Bmatrix} v(x, t) \\ w(x, t) \end{Bmatrix} \quad (4.3)$$

$$[N_\theta]\{q\} = \begin{Bmatrix} \theta_y(x, t) \\ \theta_z(x, t) \end{Bmatrix} \quad (4.4)$$

$$[N_\varphi]\{q\} = \varphi(x, t) \quad (4.5)$$

$$[N_v] = \begin{bmatrix} N_1 & 0 & 0 & N_2 & 0 & N_3 & 0 & 0 & N_4 & 0 \\ 0 & N_1 & -N_2 & 0 & 0 & 0 & N_3 & -N_4 & 0 & 0 \end{bmatrix} \quad (4.6)$$

$$[N_\theta] = \begin{bmatrix} 0 & -N_5 & N_6 & 0 & 0 & 0 & -N_7 & N_8 & 0 & 0 \\ N_5 & 0 & 0 & N_6 & 0 & N_7 & 0 & 0 & N_8 & 0 \end{bmatrix} \quad (4.7)$$

$$[N_\varphi] = [0 \quad 0 \quad 0 \quad 0 \quad N_9 \quad 0 \quad 0 \quad 0 \quad 0 \quad N_{10}] \quad (4.8)$$

By evaluating Equation (4.2) at each node in accordance with the Timoshenko beam theory, the values of the shape functions, N , can be written as,

$$N_1 = \frac{(1-3\gamma^2+2\gamma^3+(1-\gamma)\beta)}{1+\beta} \quad (4.9)$$

$$N_2 = \frac{l\left(\gamma - 2\gamma^2 + \gamma^3 + \frac{(\gamma - \gamma^2)\beta}{2}\right)}{1 + \beta} \quad (4.10)$$

$$N_3 = \frac{(3\gamma^2 - 2\gamma^3 + \gamma\beta)}{1 + \beta} \quad (4.11)$$

$$N_4 = \frac{l\left(-\gamma^2 + \gamma^3 - \frac{(\gamma - \gamma^2)\beta}{2}\right)}{1 + \beta} \quad (4.12)$$

$$N_5 = \frac{6(-\gamma + \gamma^2)}{l(1 + \beta)} \quad (4.13)$$

$$N_6 = \frac{(1 - 4\gamma + 3\gamma^2 + (1 - \gamma)\beta)}{1 + \beta} \quad (4.14)$$

$$N_7 = \frac{6(\gamma - \gamma^2)}{l(1 + \beta)} \quad (4.15)$$

$$N_8 = \frac{(-2\gamma + 3\gamma^2 + \gamma\beta)}{1 + \beta} \quad (4.16)$$

$$N_9 = 1 - \gamma \quad (4.17)$$

$$N_{10} = \gamma \quad (4.18)$$

$$\gamma = \frac{x}{l} \quad (4.19)$$

$$\beta = \frac{12EI}{kGA l^2} \quad (4.20)$$

where β is the shear deformation parameter that relates the bending stiffness to the shear stiffness, E is the modulus of rigidity, I is the cross-sectional area second moment of inertia, A is the cross-sectional area, l is the length of the element, G is the shear modulus and k is the shear correction factor that depends on the shape of the cross-section (2/3 for a rectangle and 3/4 for a circle).

The defined shape functions can now be used to express the energy functions of the rotor elements in FE terminology. In the following sections, the kinetic, strain and potential energy as well as the generalized forces will be constructed in matrix format for the shaft, blade and disk elements to enable the development of the global equation of motion of the system using Lagrange principle.

4.3. Shaft Element

In Section 3.3.2, an expression for the kinetic energy of the shaft element was derived and expressed in Equation (3.13). The rotational kinetic energy term was simplified as,

$$\begin{aligned} \frac{1}{2} \int_V \rho \{r_p\} [\tilde{\omega}]^T [\tilde{\omega}] \{r_p\} dV &= \frac{1}{2} \int_0^l I_p \dot{\Omega}^2 dx + \int_0^l I_p \dot{\phi}^T \dot{\phi} dx \\ &+ \int_0^l I_p \dot{\Omega} \dot{\phi} dx - \int_0^l I_p (\dot{\Omega} + \dot{\phi}) \dot{\theta}_z^T \theta^y dx + \int_0^l I_D \begin{Bmatrix} \dot{\theta}_y \\ \dot{\theta}_z \end{Bmatrix}^T \begin{Bmatrix} \dot{\theta}_y \\ \dot{\theta}_z \end{Bmatrix} dx \end{aligned} \quad (4.21)$$

By using the shape functions, Equation (4.21) can be written as,

$$\begin{aligned} \frac{1}{2} \int_V \rho \{r_p\} [\tilde{\omega}]^T [\tilde{\omega}] \{r_p\} dV &= \frac{1}{2} \int_0^l I_p \dot{\Omega}^2 dx + \int_0^l \{\dot{q}\}^T [N_\phi]^T I_p [N_\phi] \{\dot{q}\} dx \\ &+ \int_0^l I_p \dot{\Omega} \dot{\phi} dx - \int_0^l \{\dot{q}\}^T [N_{\theta_z}]^T I_p \dot{\Omega} [N_{\theta_y}] \{\dot{q}\} dx \\ &- \int_0^l \{\dot{q}\}^T [N_{\theta_z}]^T I_p [N_{\theta_y}] \{q\} [N_\phi] \{\dot{q}\} dx + \int_0^l \{\dot{q}\}^T \begin{Bmatrix} [N_{\theta_y}] \\ [N_{\theta_z}] \end{Bmatrix}^T I_D \begin{Bmatrix} [N_{\theta_y}] \\ [N_{\theta_z}] \end{Bmatrix} dx \end{aligned} \quad (4.22)$$

To further simplify Equation (4.22), the following expressions are introduced,

$$\frac{1}{2} \int_0^l I_p dx = C_1 \quad (4.23)$$

$$\int_0^l [N_\varphi]^T I_p [N_\varphi] dx = [M_\varphi] \quad (4.24)$$

$$\int_0^l [N_{\theta_z}]^T I_p [N_{\theta_y}] dx = [g^s] \quad (4.25)$$

$$\int_0^l I_p [N_{\theta_z}]^T [N_{\theta_y}] \{e\} [N_\varphi] dx = [M_e] \quad (4.26)$$

$$\int_0^l \begin{Bmatrix} [N_{\theta_y}] \\ [N_{\theta_z}] \end{Bmatrix}^T I_D \begin{Bmatrix} [N_{\theta_y}] \\ [N_{\theta_z}] \end{Bmatrix} dx = [M_r] \quad (4.27)$$

where $[M_e]$ is the inertia coupling between torsional and transverse vibrations. The inertial coupling between rigid body motion and elastic motion is given by the term $\int_0^l I_p \Omega \dot{\varphi} dx$. When the angular velocity of the beam, Ω , is constant, the term has no contribution to the beam equation of motion. Thus, it can be omitted. Using the aforementioned expressions, the kinetic energy of the shaft element can be expressed as,

$$\begin{aligned} T = & \frac{1}{2} \{\dot{q}\}^T [M_t] \{\dot{q}\} + \frac{1}{2} C_1 \dot{\Omega}^2 + \frac{1}{2} \{\dot{q}\}^T [M_\varphi] \{\dot{q}\} \\ & - \{\dot{q}\} \dot{\Omega}^T [g^s] \{q\} - \{\dot{q}\}^T [M_e] \{\dot{q}\} + \frac{1}{2} \{\dot{q}\}^T [M_r] \{\dot{q}\} \end{aligned} \quad (4.28)$$

Or simply,

$$T^s = \frac{1}{2} \{\dot{q}^s\}^T [M^s] \{\dot{q}^s\} + \frac{1}{2} C_1^s \dot{\Omega}^2 - \dot{\Omega} \{\dot{q}^s\}^T [g^s] \{q^s\} \quad (4.29)$$

where

$$[M^s] = [M_t^s] + [M_r^s] + [M_\varphi^s] + [M_e^s] \quad (4.30)$$

$$[M_t^s] = \int_0^{l^s} [N_v^s]^T \mu^s A^s [N_v^s] dx \quad (4.31)$$

where $[M^s]$ is the composite mass matrix, $[g^s]$ is the gyroscopic matrix and μ^s is the density of the element per unit area and A^s is the cross-sectional area of shaft element.

The strain energy of shaft element was derived in Section 3.3 and explicitly expressed at last by Equation (3.40). Using the established shape functions, the total strain energy of the shaft can be written as,

$$U^s = \frac{1}{2} \{q^s\}^T [K^s] \{q^s\} \quad (4.32)$$

where U^s is the strain energy for shaft element and $[K^s]$ is an augmented stiffness matrix, which can be defined as the following,

$$[K^s] = [k_e^s] + [k_s^s] + [k_t^s] \quad (4.33)$$

$$[k_e^s] = \int_0^l EI_a [N_\theta^{s'}]^T [N_\theta^{s'}] dx = \text{Elastic stiffness matrix} \quad (4.34)$$

$$[k_s^s] = \int_0^l [B_s^s]^T kGA [B_s^s] dx = \text{Shear stiffness matrix} \quad (4.35)$$

$$[k_t^s] = \int_0^l [\varphi^{s''}]^T GI_p [\varphi^{s''}] dx = \text{Torsional stiffness matrix} \quad (4.36)$$

$$[B_s^s] = [N_v^{s'}] - [N_\theta^s] \quad (4.37)$$

where (') denotes a differentiation with respect to s . Equation (4.37) demonstrates the coupling among the lateral displacement and lateral angular deflection in beam element.

4.4. Blade Element

The kinetic energy of the blade was addressed in Section 3.4.1. The final form is written in Equation (3.41). Equation (3.41), in FE terminology, can be written as,

$$T^b = \frac{1}{2} \{\dot{q}^b\}^T [M^b] \{\dot{q}^b\} \quad (4.38)$$

where

$$[M^b] = [M_t^b] + [M_r^b] \quad (4.39)$$

$$[M_t^b] = \int_0^{l^b} [N_{v^*}^b]^T \mu^b A^b [N_{v^*}^b] dx = \textit{Translational inertia} \quad (4.40)$$

$$[[M_r^b] = \int_0^{l^b} [N_\theta^b]^T \mu^b I^b [N_\theta^b] dx = \textit{Rotational inertia} \quad (4.41)$$

The potential energy of the blade element is the summation of the strain energy due to bending the potential energy due to centrifugal forces as explained in Section 3.4.2. The potential energy of the blade element in matrix form can be written as,

$$U^b = \frac{1}{2} \{q^b\}^T [k^b] \{q^b\} - \frac{1}{2} \{q^b\}^T \Omega^2 \sin^2 \Psi [M_t^b] \{q^b\} \quad (4.42)$$

$$[k^b] = [k_e^b] + [k_s^b] + [k_c^b] \quad (4.43)$$

$$[k_e^b] = \int_0^{l^b} [N_{\theta'}^b]^T E^b I^b [N_{\theta'}^b] dx = \textit{Elastic Stiffness} \quad (4.44)$$

$$[k_s^b] = \int_0^{l^b} [B_s^b]^T k^b G^b A^b [B_s^b] dx = \textit{Shear Stiffness} \quad (4.45)$$

$$[k_c^b] = \int_0^{l^b} F [N_{v^*}^b]^T [N_{v^*}^b] dx = \textit{Centrifugal Stiffness} \quad (4.46)$$

$$[B_s^b] = [N_{v'}^b] - [N_\theta^b] \quad (4.47)$$

4.5. Disk Element

The disk is modeled as a rigid body and only exhibit kinetic energy as demonstrated in Section 3.5. The kinetic energy of the disk in matrix format using the established generalized coordinates can be written as,

$$T^d = \frac{1}{2} \{\dot{q}^d\}^T [m^d] \{\dot{q}^d\} + \frac{1}{2} I_p^d \dot{\Omega}^2 - \dot{\Omega} \{\dot{q}^d\}^T [g^d] \{q^d\} \quad (4.48)$$

$$[m^d] = [m_t^d] + [m_r^d] + [m_\theta^d] - 2[m_e^d] \quad (4.49)$$

$$[m_t^d] = \begin{bmatrix} m_d & 0 & 0 & 0 & 0 \\ 0 & m_d & 0 & 0 & 0 \\ 0 & 0 & 0 & 0 & 0 \\ 0 & 0 & 0 & 0 & 0 \\ 0 & 0 & 0 & 0 & 0 \end{bmatrix} \quad (4.50)$$

$$[m_r^d] = \begin{bmatrix} 0 & 0 & 0 & 0 & 0 \\ 0 & 0 & 0 & 0 & 0 \\ 0 & 0 & I_d^d & 0 & 0 \\ 0 & 0 & 0 & I_d^d & 0 \\ 0 & 0 & 0 & 0 & 0 \end{bmatrix} \quad (4.51)$$

$$[m_\theta^d] = \begin{bmatrix} 0 & 0 & 0 & 0 & 0 \\ 0 & 0 & 0 & 0 & 0 \\ 0 & 0 & 0 & 0 & 0 \\ 0 & 0 & 0 & 0 & 0 \\ 0 & 0 & 0 & 0 & I_p^d \end{bmatrix} \quad (4.52)$$

$$[m_e^d] = \begin{bmatrix} 0 & 0 & 0 & 0 & 0 \\ 0 & 0 & 0 & 0 & 0 \\ 0 & 0 & 0 & \theta_y & 0 \\ 0 & 0 & 0 & 0 & 0 \\ 0 & 0 & 0 & 0 & 0 \end{bmatrix} \quad (4.53)$$

$$[g^d] = \begin{bmatrix} 0 & 0 & 0 & 0 & 0 \\ 0 & 0 & 0 & 0 & 0 \\ 0 & 0 & 0 & I_p^d & 0 \\ 0 & 0 & 0 & 0 & 0 \\ 0 & 0 & 0 & 0 & 0 \end{bmatrix} \quad (4.54)$$

where m^d is the mass of the disk, g^d is the gyroscopic moment matrix of the disk, I_p^d is the polar moment of inertia of the disk around the axis of rotation and I_d^d is the diametral moment of inertia of the disk around the y-axis.

4.6. External Forces

The external forces and moments applied on the shaft can be addressed using the virtual work concept as the following,

$$\delta W(x, t) = f_v \delta v + f_w \delta w \quad (4.55)$$

Or in matrix format,

$$\delta W(x, t) = [f(t)]\{\delta q^s\} \quad (4.56)$$

where $[f(t)]$ is a row vector composed of the nodal forces, f_i . The external force vector will take into account the bearing effect, stiffness and damping, as well as any external excitation applied on the system.

4.7. Global Equation of Motion

The global equation of motion of the rotor is constructed using the Lagrange method. Lagrange method is a technique based on the calculus of variation used to construct the equation of motion of systems using the principle of mechanical energy. Lagrange equation is seen below,

$$\frac{d}{dt} \left(\frac{\partial T}{\partial \dot{q}_j} \right) - \frac{\partial T}{\partial q_j} + \frac{\partial U}{\partial q_j} = Q_j, \quad j = 1, 2, \dots, M \quad (4.57)$$

where T is the system kinetic energy, U is the system potential energy, q is the generalized coordinates and Q is the generalized external forces.

Upon using the appropriate assembly techniques to combine the matrices of the shaft, disk and blades into a global rotor system coordinates using the generalized coordinates of each, the global equation of motion for the rotor system can be written in the following form,

$$[M]\{\ddot{q}\} + [D]\{\dot{q}\} + [K]\{q\} = \{F\} \quad (4.58)$$

where M , D and K are the augmented mass, damping, stiffness matrices of the rotor system, respectively. q and F are the generalized coordinates and external forces vectors on the rotor system, respectively. The generalized coordinates vector, q , consists of the shaft, disk and blades generalized coordinates vectors as follows,

$$\{q\} = \{q^s \quad q^d \quad q^b\}^T \quad (4.59)$$

where s , d and b denote shaft, disk and blades, respectively. The mass matrix, M , consists of the shaft, disk and blades inertia values in the global X, Y, Z directions. Each

component's matrix essentially includes the transverse and rotary inertia terms. The rotor system augmented mass matrix can be defined by the following summation,

$$[M] = [M^s] + [m^d] + [M^b] \quad (4.60)$$

The rotor system augmented damping matrix, D , includes the bearing's damping matrix and the gyroscopic matrices of the shaft and the disk. It can be written as,

$$[D] = \dot{\Omega}[g^s] + \dot{\Omega}[g^d] + [D_{bearings}] \quad (4.61)$$

Since it was assumed that the bearings are modeled with linearized isotropic stiffness and damping values, $D_{bearings}$ matrix is symmetric. D is skew-symmetric in nature due to the coupling terms imposed by the gyroscopic matrices.

The augmented stiffness matrix of the rotor system can be expressed as the following,

$$[K] = [K^s] + [K^b] + [K_{bearings}] \quad (4.62)$$

The rotor system augmented stiffness matrix, K , includes the bearings stiffnesses matrix, the shaft stiffness matrices due to bending, torsional and shear forces and the blades stiffness matrices due to bending and shear forces as well as the centrifugal forces that results for the blade's rotation around the shaft. The explicit stiffness matrix of the blade elements can be written as,

$$[K^b] = [k_e^b] + [k_s^b] + [k_c^b] - \Omega^2 \sin^2 \Psi [M_t^b] \quad (4.63)$$

The generalized forcing vector, F , can be zero to study the free response of the system. It also can be linear or nonlinear, harmonic, periodic or random to model any type of excitation that real systems are subject to.

4.8. Coupling Properties

4.8.1 Element Coordinates Coupling

By examining the resultant inertia, stiffness and gyroscopic matrices of the shaft and blades we observe the existence of coupling between the lateral and torsional vibrations, in the form of inertial and geometrical coupling. Inertial coupling appears when the mass matrix of the element is non-symmetric. The shaft and disk inertial term, denoted by $[M_e]$ in Equation (4.26) and (4.53), provides the inertial coupling between the lateral and torsional vibrations of the shaft and disk. The geometrical coupling exists when the stiffness matrix of the element is non-symmetric. This coupling is attributed to the presence of shear deformation stiffness in the shaft and blades matrices that has the term $[B_s]$ present as seen in Equation (4.37) and Equation (4.47).

4.8.2 Structural Coupling

The major components of the rotor system (shaft, disk and blades) are coupled on structural level. The disk that is modeled as a rigid body is lumped to the shaft into Node 9. This means that by appropriately assembling the global matrices of the system, the nodal inertial and gyroscopic moment properties of the disk will add linearly to those of the shaft at Node 9. Likewise, the inertial and gyroscopic properties of the blades will also be added to those at Node 9 to account for the blade dynamic behavior. This summation of dynamic properties will result in a global mass and damping matrix that has non-diagonal terms, which will essentially provide the inertial coupling to the rotor components. This coupling scheme is done in ANSYS FE package using constraint equations where the nodal degrees

of freedom of the disk and blades-roots are forced to follow those of the shaft at Node 9. implementation of coupling will be elaborated in Chapter 5.

In addition to the inertial coupling among shaft, disk and blades, there exists a geometrical coupling between the shaft and the blades attributed to the stagger angle Ψ . As explained in Section 3.4.1, the stagger angle is the inclination angle between the mid-plane of the blade and the axis of rotation. The setting of this angle dictates the vibrations of the blade due to shaft rotation, whether they will be pure flapping or has a transverse component in the x - y plane. The stagger angle also provides geometrical coupling between the blades and the shaft lateral vibrations due to the existence of the term $-\Omega^2 \sin^2 \Psi [M_t^b]$ in Equation (4.63). This coupling is deemed crucial as it provides means of lateral vibrations transmission from the blades to the shaft, and ultimately allows for blade-faults detections through indirect vibrations measurement as will be demonstrated later in this thesis.

CHAPTER 5

NUMERICAL SOLUTION

5.1. Rotordynamics Analysis in ANSYS

The numerical solution of the established Shaft-Disk-Blade (SDB) rotor model is carried out using *ANSYS* Parametric Design Language (*APDL*) software. *APDL* is a general-purpose commercial software based on the Finite Element (FE) method that provides numerical aid to solve various problem types including, structural mechanics, fluid flow, heat transfer, electromagnetism. In structural mechanics, *APDL* provides a specific module to handle *Rotordynamics* problems. In this module, *APDL* allows simulating the dynamic response of axisymmetric structures accounting for various inertial effects such as the centrifugal forces and the gyroscopic effects. Users may use *APDL* to perform modal, harmonic or transient analyses on rotating structures and develop insight about the dynamics of the structure in various running conditions via attributes like mode shapes and critical speeds.

The basic *Rotordynamics* analysis approach in *APDL* involves the following steps,

- 1- Build the model
- 2- Define element types and material properties
- 3- Define rotational velocity and account for the gyroscopic effect
- 4- Mesh the model

- 5- Solve the model
- 6- Postprocessing

Typically Step 1 and Step 2 go together. While Step 1 involves defining the geometry of the model, which includes the location and dimension of the different rotor components, Step 2 involves selecting element types, which largely influence the geometry assignment. For example, if the shaft is modeled using beam element, the shaft geometry should be 1-D straight line. Whereas, if the shaft is modeled as a 3-D solid element, the geometry should be changed accordingly into a 3-D cyclic body.

APDL offers more than 150 types of element that users can select from. 1-D, 2-D and 3-D elements are all supported and can be selected depending on the required analysis types. In *Rotordynamics* analysis, however, only axisymmetric elements are supported due to software limitations. Among those elements are BEAM188 and PIPE161 elements that are based on beam theory and can be used to model rotating shafts and blades, MASS221, SHELL181 and SOLID185 elements can be used to model the disk and blades while COMBI214 and MATRIX27 can be used to model bearings. A discussion of the selected elements in this work is detailed in section 5.4.

In step 3, the rotational effects on the structure are specified. The rotational speed is either applied on the entire structure using OMEGA command or on specific components using the CMOMEGA command. The rotational effects such as the gyroscopic moment and the rotation damping are then applied to the model using the CORIOLIS command.

In Step 4, the actual FE model is generated through the meshing process. Here, the physical spatial body is modeled using a set of finite elements and nodes that define the connectivity

among those elements. *APDL* provides two general types of meshing processes, mapped and free. Mapped meshing is a controlled technique where geometrical constraints are created to generate a regular mesh patterns in areas and volumes. On the contrary, free meshing does not adhere to such constraints and typically yield meshed areas and volumes that have no specific patterns. The created mesh elements in both techniques are either linear or quadratic in terms of nodal arrangement, and triangle, quadrilateral, hexahedral or tetrahedral in terms of shape. Users may select to default-mesh their models using the program-selected options, or specify the meshing parameters to generate a specific meshing outcome.

The meshing process does not completely describe the rotor as it leaves out the coupling across rotor's component. A disk that is rigidly connected to the shaft will behave differently than a disk that is connected to that shaft via structural joints. Typically, such physical interaction is translated into some form of coupling among the nodal Degrees of Freedom (DOF) of adjacent elements. This DOF coupling is not defined in the meshing process and must be specified. In *APDL*, the DOF coupling is done by either creating coupling regions or defining constraints equations. More on this is addressed in Section 5.4.

Upon generating the mesh and defining the connectivity of the model, Step 5 addresses the solution to the FE model. In general, this step includes defining the boundary conditions, the loads on the model and the solver type to be used. Boundary conditions are generally a physical constraint that is simulated on the model via DOF constraint. In *Rotordynamics*, such DOF constraints are applied on bearing and shaft nodes.

APDL allows the application of various loads in its simulations. Loads can be forces, moments or a combination of both. They can be applied on nodes, nodal forces and moments, be distributed over a surface, or be body forces. Loads can take different forms and shapes. They can be constant, varying with time or even random, depending on the loading that is being simulated.

Once the nodal constraints and loads are applied, the analysis type must be specified to carry out the required analysis. As stated earlier, *APDL* support modal, harmonic and transient analyses in its *Rotordynamics* module. In modal analysis, which is essentially an eigenvalue problem, *APDL* uses *DAMP* and *QRDAMP* eigen-solvers to solve the system. Both solvers consider the rotational effect in the structure. The only difference between the two solves is that *QRDAMP* uses the mode-superposition method to solve a reduced system of equations for computation efficiency purposes. In harmonic and transient analyses, a full method and a mode-superposition method, which is based on *QRDAMP* solver, can be used to solve the system and simulate the harmonic or transient response of the system to the applied loads.

The last step in *APDL Rotordynamics* analysis is postprocessing, Step 7. Therein, the results are displayed in different forms for review purposes. *APDL* uses *POST1*, the general postprocessor, to present modal results. The results can be viewed in the form of natural frequencies values (eigenvalues), mode shapes, orbit plots or Campbell diagram and critical speeds in the case where rotation is applied. For harmonic and transient response, *APDL* uses *POST26*, the time-history postprocessor, to present nodal solution results in time-wave or frequency spectrum plots.

5.2. Model Parameters

The parameters of the rotor model in this work were similar to those introduced by Hui Ma, et al. in [36] as seen in Figure 5.1. This model was adopted in this research for validation purposes, with some modifications to blade's geometry. The authors of [36] conveniently listed the design parameters of the rotor system they used including the materials properties of the different elements and the bearing characteristics. In addition, the paper presents modal analysis results of the structure, considering rotation, using *ANSYS APDL*. Those two features facilitate a comprehensive comparison and validation process of the model used in this research.

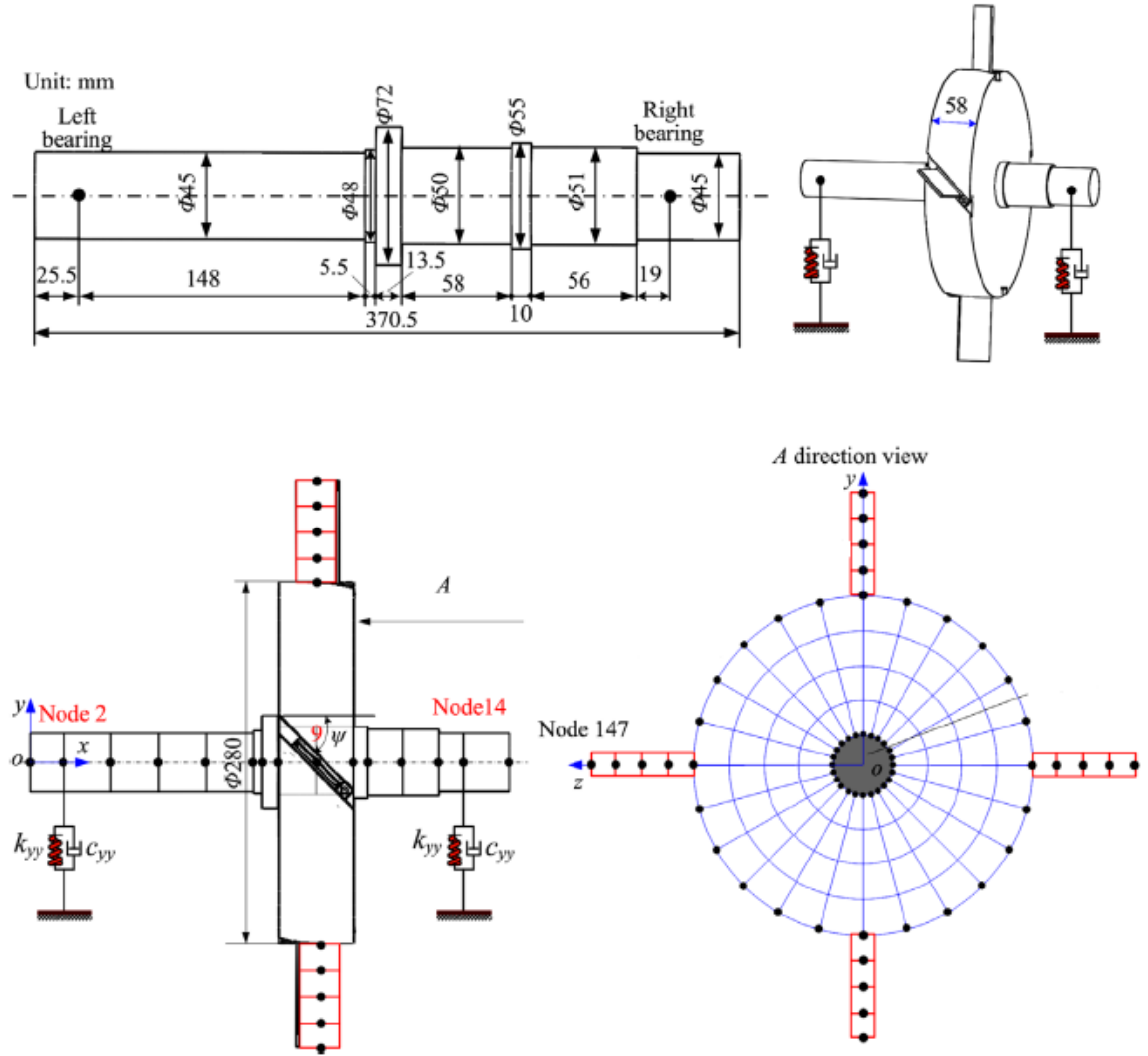
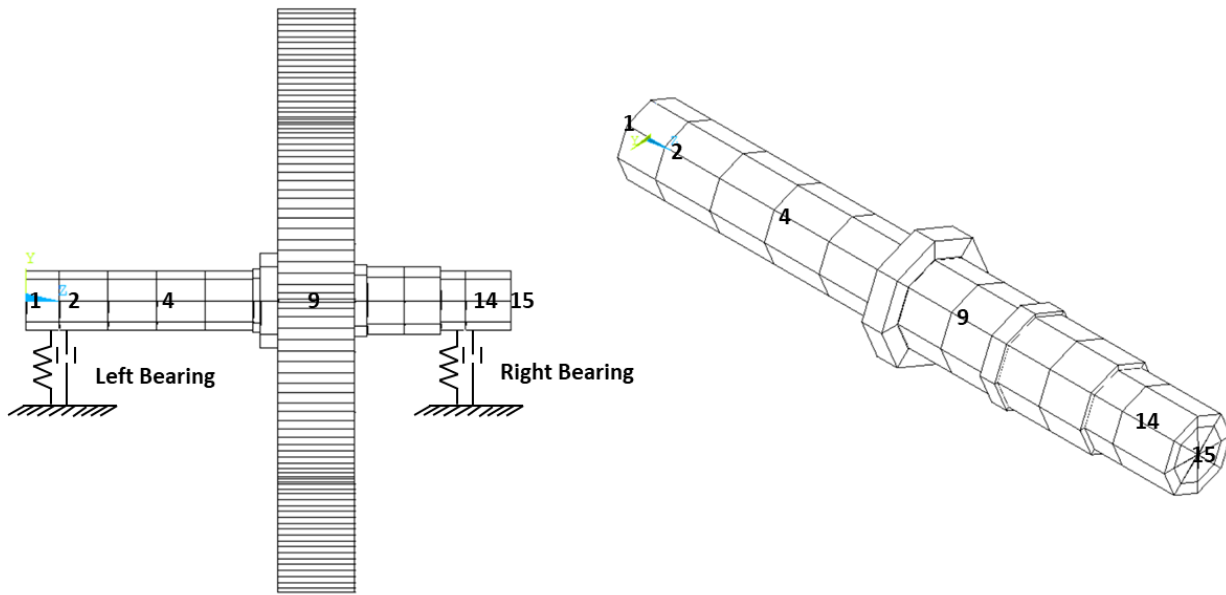


Figure 5.1. Physical dimensions of the model presented in [36].

The rotor model used in this research is illustrated in Figure 5.2. The shaft consists of 14 spools of 6 different cross sections, a disk and four rectangular thin blades that are attached to the disk with 90° stagger angle (Ψ in Equation (4.63) = 90°). Two ideal bearings are supporting the rotor with equal linearized stiffness and damping coefficients along the lateral directions (x and y – axis). The full parameters of the system including the dimensions of shaft spools, disk and blades, the materials properties of each component and the bearing characteristics are listed in Table 5.1 and Table 5.2.

(a)



(b)

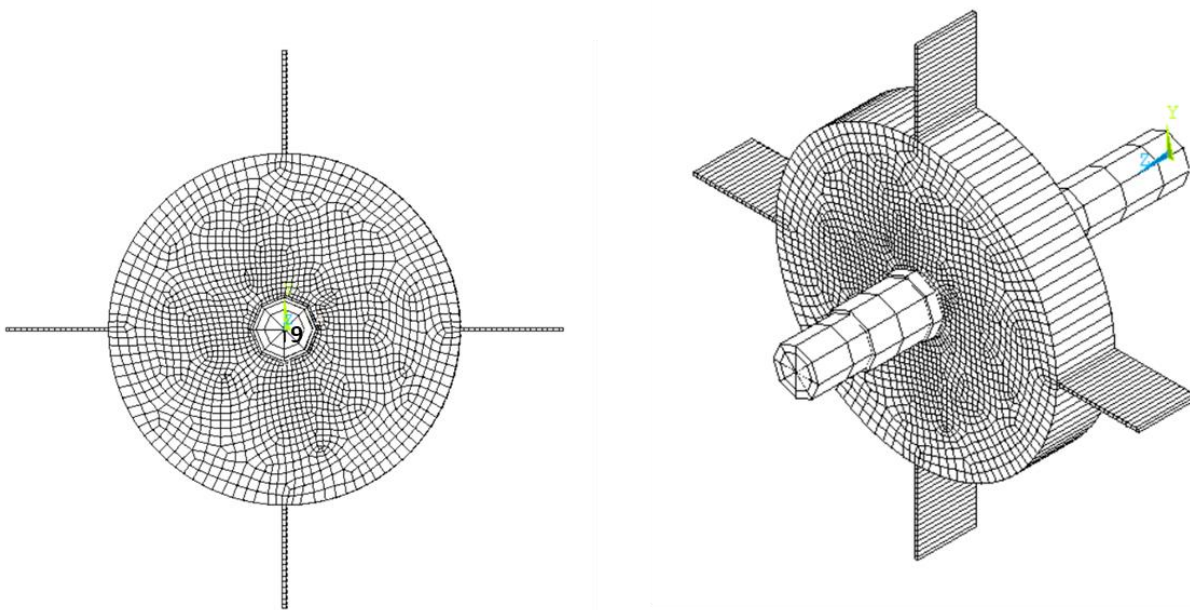


Figure 5.2. Rotor model used in this research: (a) shaft and (b) disk and blades.

Table 5-1. Geometric Parameters of Rotor Model

Node	Axial Position (mm)	Bearing/Disk	Length (mm)	Diameter (mm)
1	0		25.5	45
2	25.5	Left Bearing	25.5	45
3	62.5		37.0	45
4	99.5		37.0	45
5	136.5		37.0	45
6	173.5		37.0	45
7	179.0		5.5	48
8	192.5		13.5	72
9	221.5	Shaft	29.0	50
		Disk	58.0	280
10	250.5		29.0	50
11	260.5		10.0	55
12	288.5		28.0	51
13	316.5		28.0	51
14	335.5	Right Bearing	19.0	45
15	370.5		-	-
Blade dimensions: 82 × 58 × 3 mm				

Table 5-2. Material Properties and Bearing Characteristics of Rotor Model

Property/Characteristic	Value
Young's Modulus of Elasticity (N/m^2)	$2.00 * 10^{11}$
Poisson Ratio	0.3
Volume Density (kg/m^3)	7800
Bearing Linearized Stiffness (N/m)	$1.50 * 10^7$
Bearing Linearized Damping ($N s/m$)	$2.00 * 10^3$

5.3. Initial Element Selection and Meshing

The rotor model in Figure 5.2 can be created using 3-D solid elements or using a combination of 1-D and 2-D elements. While the 3-D models might be easier to make and allow for complex geometry modeling (i.e. twisted blades and complex impeller designs), they are less efficient at capturing the electrodynamics of the structure and typically require a finer mesh size to yield accurate results. 1-D and 2-D elements, on the other hand, are harder to deal with geometry-wise and require careful treatment of element connectivity to ensure nodal DOF compatibility. Nevertheless, 1-D and 2-D models are usually more efficient and take considerably less memory sizes to arrive at accurate results. For this reason, the model in this research is created using a combination of 1-D and 2-D elements.

When selecting the element for the rotor model it is important to consider the work done in the theory section. As outlined in the aforementioned sections, the shaft and blades are modeled according to Timoshenko beam theory. In *APDL*, the element that follow Timoshenko beam theory is BEAM188 and can be seen in Figure 5.3.

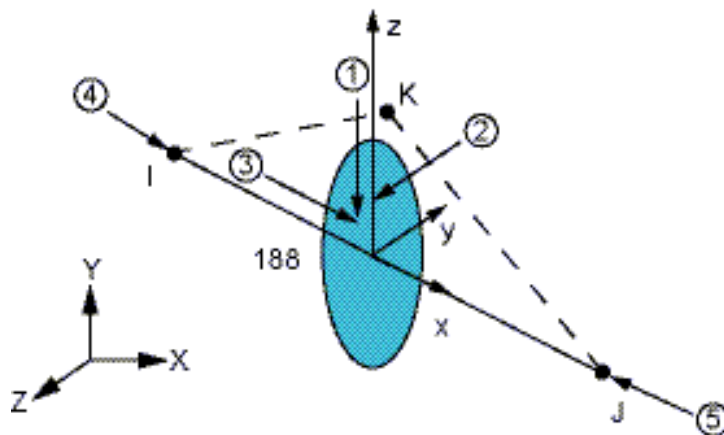


Figure 5.3. BEAM188 geometry [39].

According to *ANSYS* user manual [39], BEAM188 is a linear, quadratic, or cubic two-node line element in 3-D that is based on Timoshenko beam theory, which includes shear-deformation effect. BEAM188 has six or seven DOF at each node. These include translations in the x, y, and z directions and rotations about the x, y, and z directions. A seventh DOF (warping magnitude) is optional. This element is well-suited for analyzing slender to moderately thick beams, making it applicable to model the blades in this research. BEAM188 is also suited for linear, large rotation, and/or large strain nonlinear applications. Each of the 14 shaft elements and the four blades were initially modeled using BEAM188 elements with different cross-sections and lengths.

In the theory section, the disk is assumed to be rigid with only inertial properties. MASS21 is a nodal element that can be used to model rigid bodies in *APDL*. According to [39], MASS21 is defined by a single node, concentrated mass components in the element coordinate directions, and rotary inertias about the element coordinate axes.

The linearized bearings can be modeled using COMBI214 element, which is a 2-D spring-damper bearing element as seen in Figure 5.4. According to [39], COMBI214 is a tension-compression element that has no mass and can take up to two DOF at each node. It has translational, longitudinal and cross-coupling capabilities in 2-D applications. COMBI214 supports modeling ideal bearing with linearized characteristics in two planes.

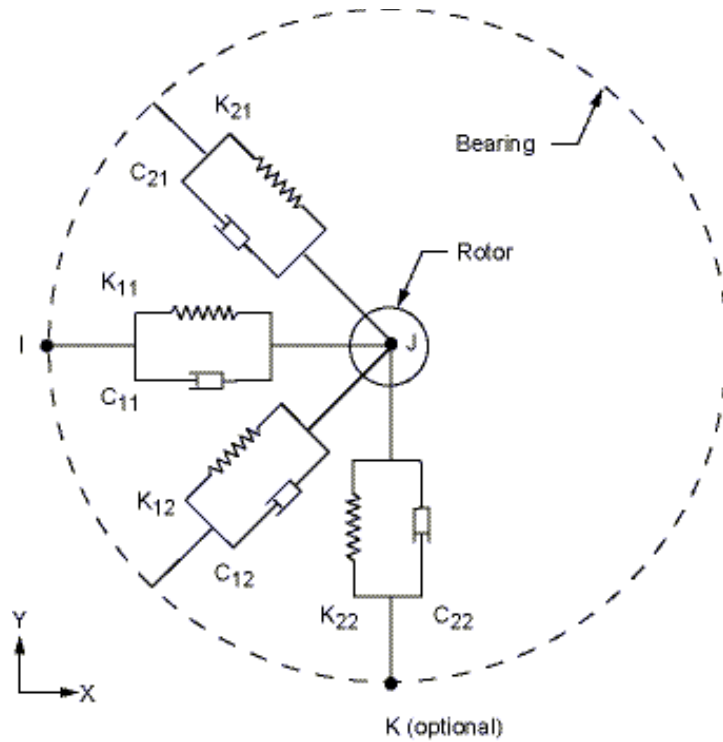


Figure 5.4. COMBI214 geometry [39].

This initial selection of elements, summarized in Table 5.3, is common in the *APDL* *Rotordynamics* simulations. This selection was later revised as will be discussed next.

Table 5-3. Initial Rotor Element Selection

Rotor Model Component	<i>APDL</i> Element
Shaft Spools	BEAM188
Disk	MASS21
Blades	BEAM188
Bearings	COMBI214

5.4. Coupling in ANSYS APDL

As discussed in Section 4.8.2, the rigid coupling between the rotor components is established theoretically in the form of inertial and geometrical coupling at Node 9 where the shaft, disk and blades all come together. This type of coupling is considered in *APDL* by creating a rigid coupling region at Node 9. Coupling regions usually involve a set of nodes, where only one of them, called the *prime* node is retained in the analysis matrix equations, while the other will be omitted. This method forces the nodal DOF of all nodes to take the values of the *prime* node. Typical applications of this coupling method are hinge and pin joints. Constraint equations, on the other hand, define a linear relationship between the nodal DOF as per the following equation [39],

$$Constant = \sum_{i=1}^N Coefficient (i) * U(i) \quad (5.1)$$

where $U(i)$ is the DOF of term i and N is the number of terms in the equation. Constraint equations allows a more general form of DOF coupling to facilitate modeling different types of physical interaction. One application of this coupling method is rigid regions. In rigid regions, the constraint equations are set so that a group of nodes, called *slave* nodes, are related to a single node, called *master* node, in such a way that only the *master* node DOF are retained in the analysis matrix. The master node in this application will be Node 9 at the shaft, where the slave nodes will be those of the disk inner radius and the blades roots.

5.5. Revised Element Selection

The initial element configuration, shown in Table 5.3, results in a structure that is not axisymmetric about the spin axis due to the blade's orientation. As seen in Figure 5.5, when blades are modeled using BEAM188 elements, they rotate around an axis that do not pass through their centerline. This violates the axisymmetric condition within *APDL* and prevent the solver from accounting for the gyroscopic effect in the dynamic calculations of the entire structure. This issue was discussed by Hui Ma, et al. in their earlier work, [15], considering the same rotor model. Therein, they had to consider two separate models, a shaft-disk rotor, and blades. In the shaft-disk model, the gyroscopic moment is considered but not the rotary inertia, including the spin softening and centrifugal stiffening effects. In the blades model, the gyroscopic moment was neglected and only the rotary inertia terms were accounted for. The effects on the modes of both models were then superimposed linearly in one Campbell diagram. The issue in this approach is that it decouples the structure, which might affect the coupled modes of vibrations among the shaft, disk and blades, which are of particular interest in this work. In [36], Hui Ma, et al. neglected the effect of the gyroscopic moment in the whole structure to overcome this issue.

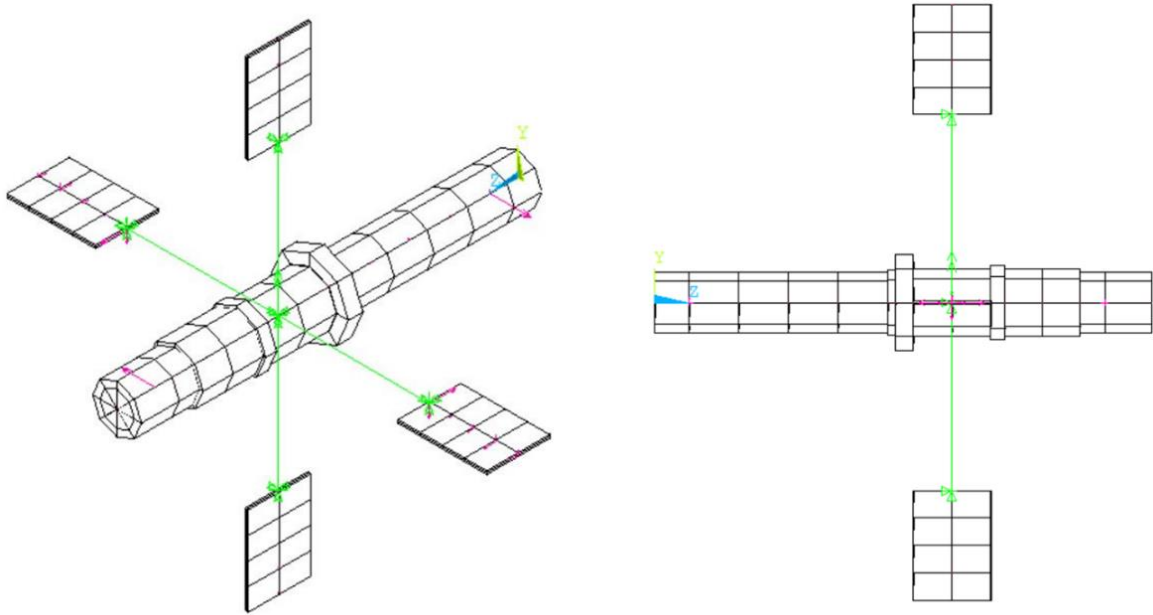


Figure 5.5. Blade's configuration using the initial element selection in Table 5.3. The rigid disk is not visible in this configuration as it modeled as a nodal mass (MASS21).

To overcome this limitation in *APDL* analysis and to avoid impacting the coupled modes by linear supposition, SHELL181 element was used to model the disk and the blades as continuous 2-D elements. Thus, the analysis can be done without decoupling the structure. According to [39], SHELL181 is a four-node element with six DOF at each node, translations in the x, y, and z directions, and rotations about those axes. SHELL181 is well-suited to analyze thin to moderately thick shell structure and is suited for linear, large rotations and large strain nonlinear applications. SHELL181 was used in *ANSYS Rotordynamics* Guide, [40] to model thin rotating disks. However, modeling the disk and blades using SHELL181 elements will result in a deviation from the theoretical model discussed in CHAPTER 3 and 4, since the disk is now modeled as a flexible body (Shell) instead of a rigid body.

With this regard, it must be reiterated that the theoretical formulations were done to establish a theoretical baseline of the research work and not to be followed strictly in the numerical model. Therefore, slight modifications to the model in response to mandatory restrictions by the simulation software are acceptable as long as they do not drastically alter the model under study. Moreover, the initial assumption made to model the disk as a rigid body in Chapter 3 was due to its large thickness. This is still valid in the model. The large thickness makes it unlikely that the disk will internally deflect at the same frequency range in which the first bending modes of the shaft and the blades are excited. To further investigate this hypothesis, a preliminary modal analysis was conducted on the disk alone while modeled with SHELL181 elements as seen in Figure 5.6. The inner radius of the disk was clamped while the outer radius was free. The disk was meshed with a program-selected controls. The first four natural frequency values of the disk are listed in Table 5.4.

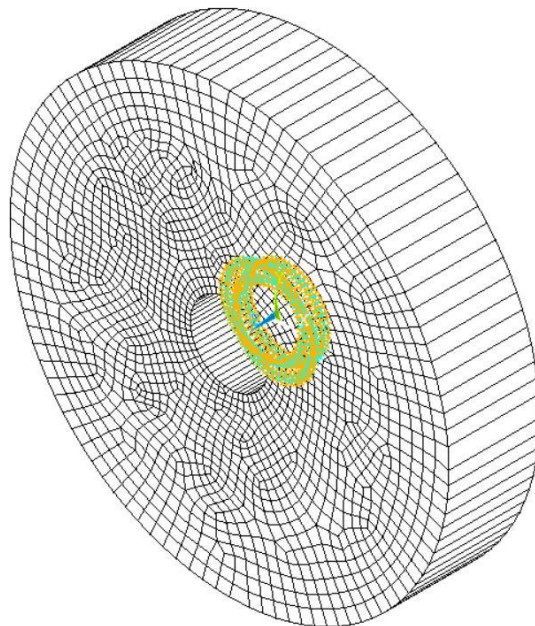


Figure 5.6. Modal analysis of the disk alone, clamped at the inner radius.

Table 5-4. First 4 Natural Frequency Values of the Disk Alone

Natural Frequency	Value (Hz)
1	1946.91
2	2236.32
3	2236.97
4	2757.86

From Table 5.4, the first internal deflection of the disk (0-nodal circle, 1-nodal diameter) occurs at a frequency value of 1946.9 Hz. It will be demonstrated in the next chapters that the frequency range that falls within the scope of this research is between 0 and 1000 Hz. At this frequency span, the rotor coupled modes of vibrations with respect to the blade first bending mode take place. Since at this frequency range the disk behaves as a rigid body although it is modeled as a flexible shell, this particular deviation does not conflict with the rigid body assumption for the disk. The influence of this deviation is further discussed in Chapter 6 when the model is compared with that in [36] for validation.

Based on the aforementioned discussion, the new element selection of the model is listed in Table 5.5.

Table 5-5. Final Rotor Element Selection

Model Component	APDL Element
Shaft Spools	BEAM188
Disk	SHELL181
Blades	SHELL181
Bearings	COMBI214

The coupling between the shaft and the disk is done by creating a rigid region linking node 9 to the inner diameter nodes of the disk using the CERIG command as explained in Section

5.4. As far as blades to disk rigid coupling, this is now done via sharing nodes, since the blades and the disk are considered as a single body. The coupling among the shaft, disk and blades in this configuration satisfies the coupling properties discussed in Section 4.8.1 and 4.8.2 and is illustrated in Figure 5.7

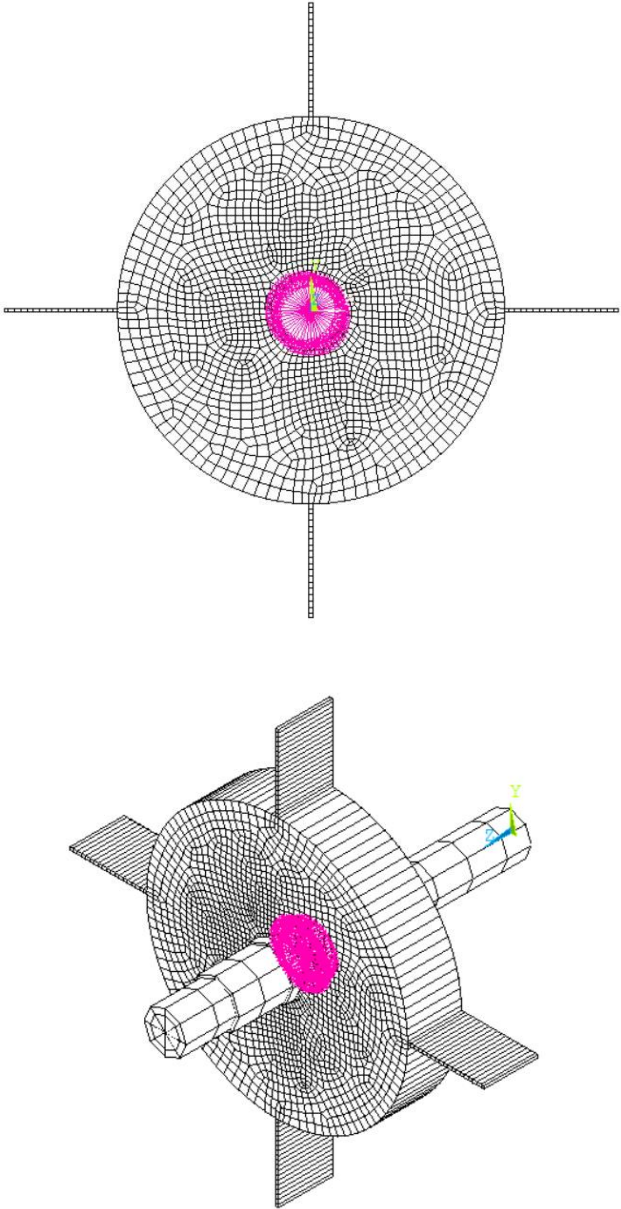


Figure 5.7. Coupling between the shaft, disk and blades.

The final rotor model mesh is seen in Figure 5.2. Each of the 14 shaft's spools was meshed as a single BEAM188 element of a cubic shape function and two nodes. This meshing scheme is following the work done in [36]. The disk and blades are modeled as a single-surface body that is irregular. The most suitable meshing scheme for irregular surface bodies are free meshing using either quadrilateral or triangular shapes. Quadrilateral shaped elements are selected to mesh the disk and blades elements using the MESH TOOL option in *APDL*, which is a program-selected control to carry out the meshing process.

A numerical convergence study was performed on the disk-blades mesh to determine the most suitable number of elements to be selected. Using the SMART SIZE option in *APDL*, the element size in the free-mesh option can be varied in a scale of 1-10. In this study, the number of elements was increased from 250 to 3000 elements in six steps and a modal analysis was conducted on each step to calculate the first 9 modes of the entire structure. The modal analysis was conducted including rotation at running speeds ranging from 0 to 20000 RPM in a step load of 5000 RPM. The difference in the meshing shape across the 6 studied cases is seen in Figure 5.8 and the results of the numerical convergence study is seen in Figure 5.9 through 5.13.

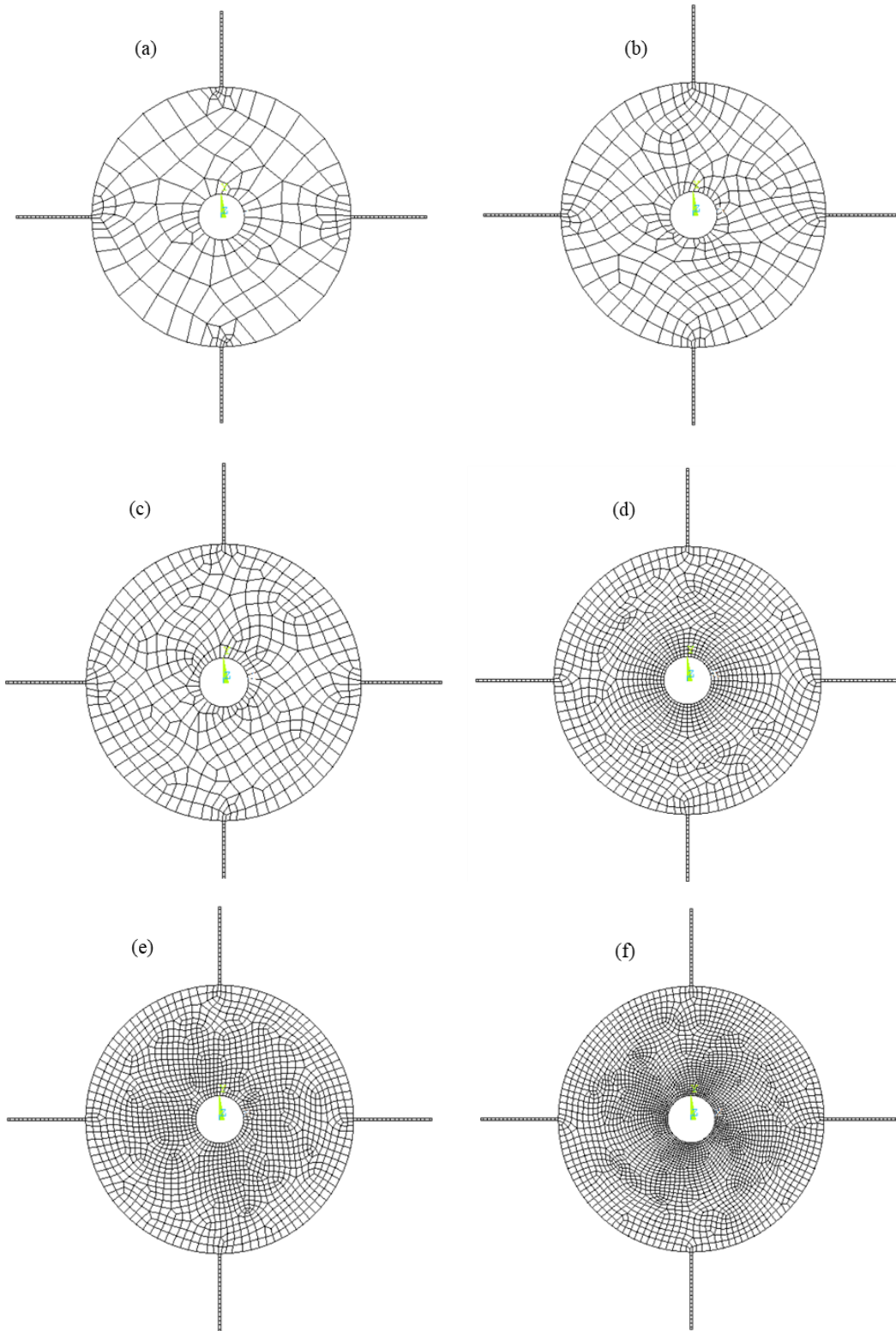


Figure 5.8. Disk-blades mesh cases for the numerical convergence study: (a) 250 elements (b) 400 elements (c) 550 elements (d) 1300 elements (e) 1750 elements (f) 3000 elements

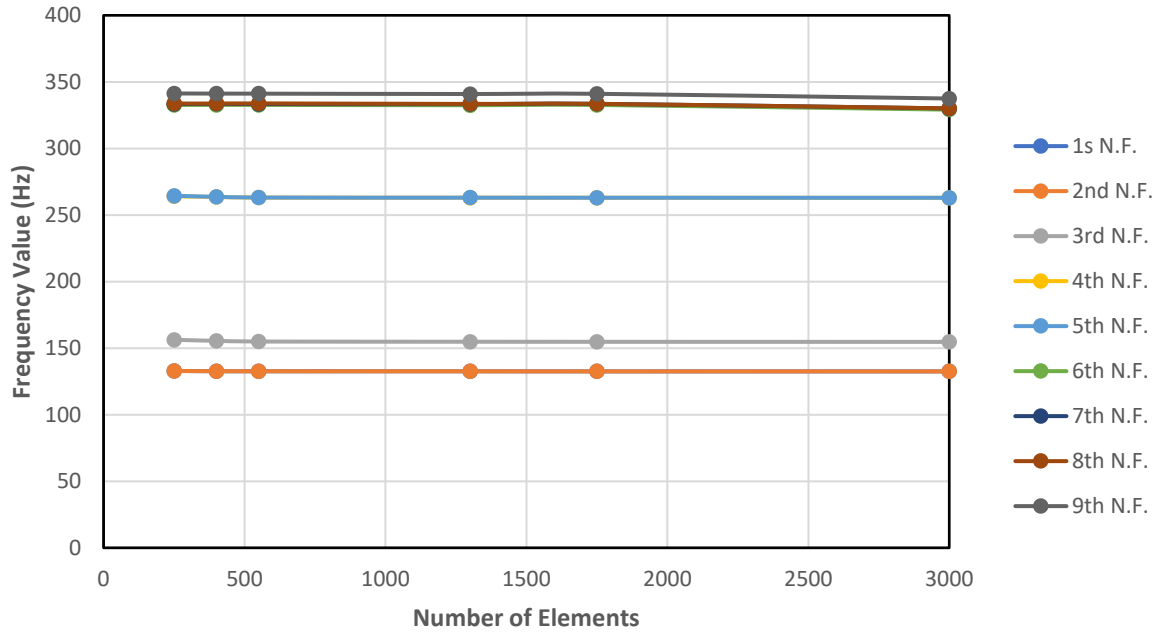


Figure 5.9. Modal results of the first 9 modes of the rotor model at 0 speed shown the effect of increasing the number of mesh elements.

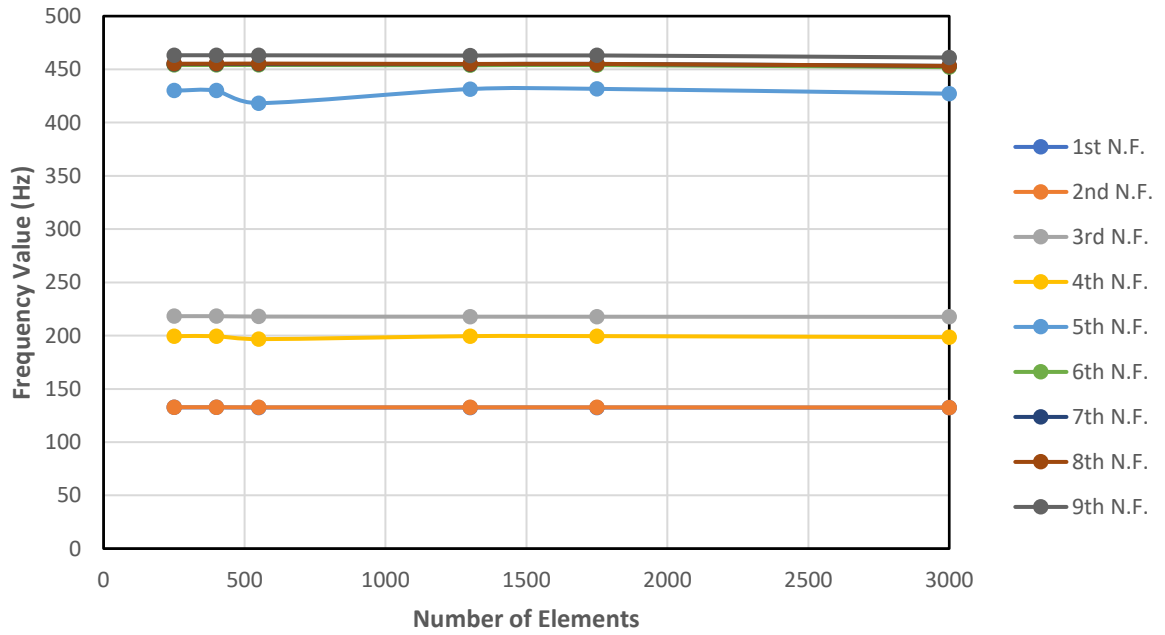


Figure 5.10. Modal results of the first 9 modes of the rotor model at 5000 RPM shown the effect of increasing the number of mesh elements.

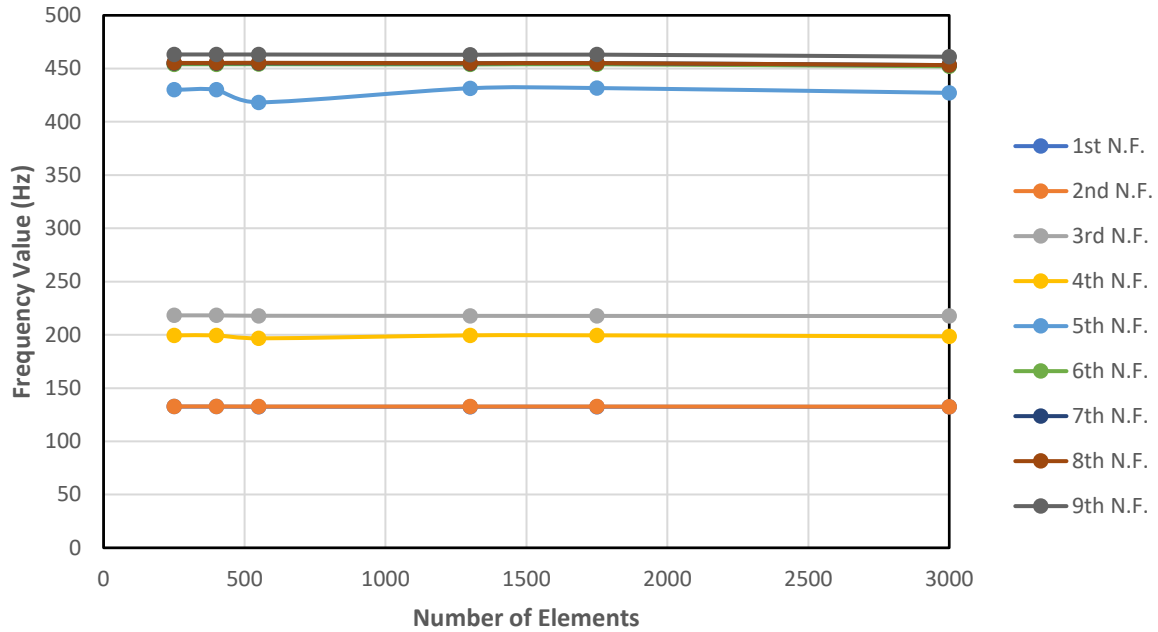


Figure 5.11. Modal results of the first 9 modes of the rotor model at 10000 RPM shown the effect of increasing the number of mesh elements.

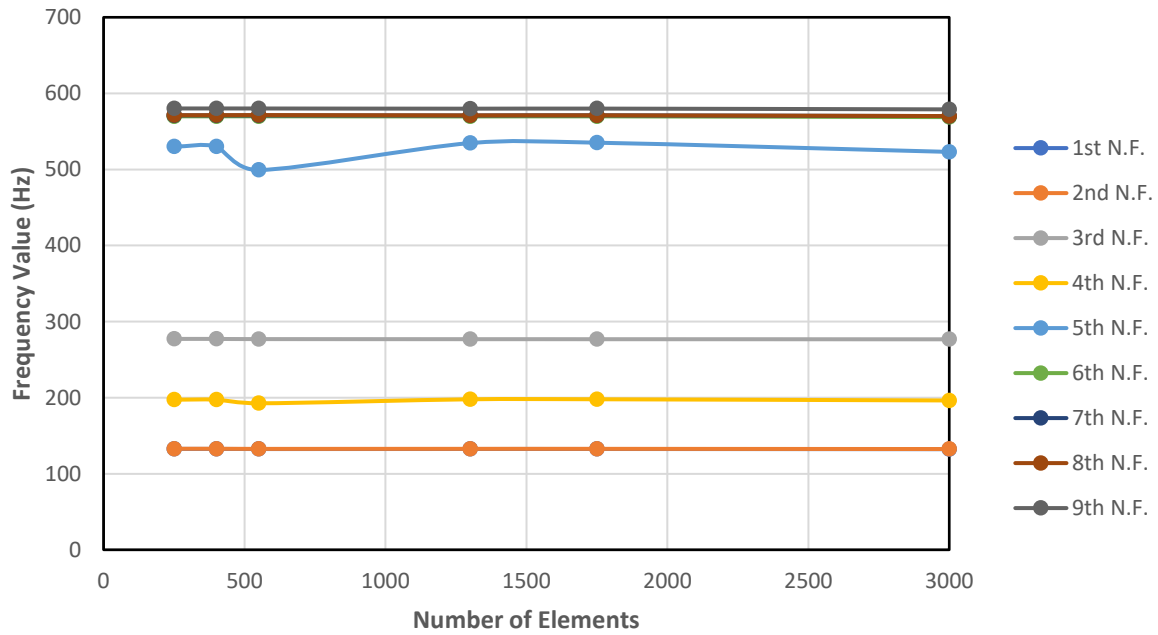


Figure 5.12. Modal results of the first 9 modes of the rotor model at 15000 RPM shown the effect of increasing the number of mesh elements.

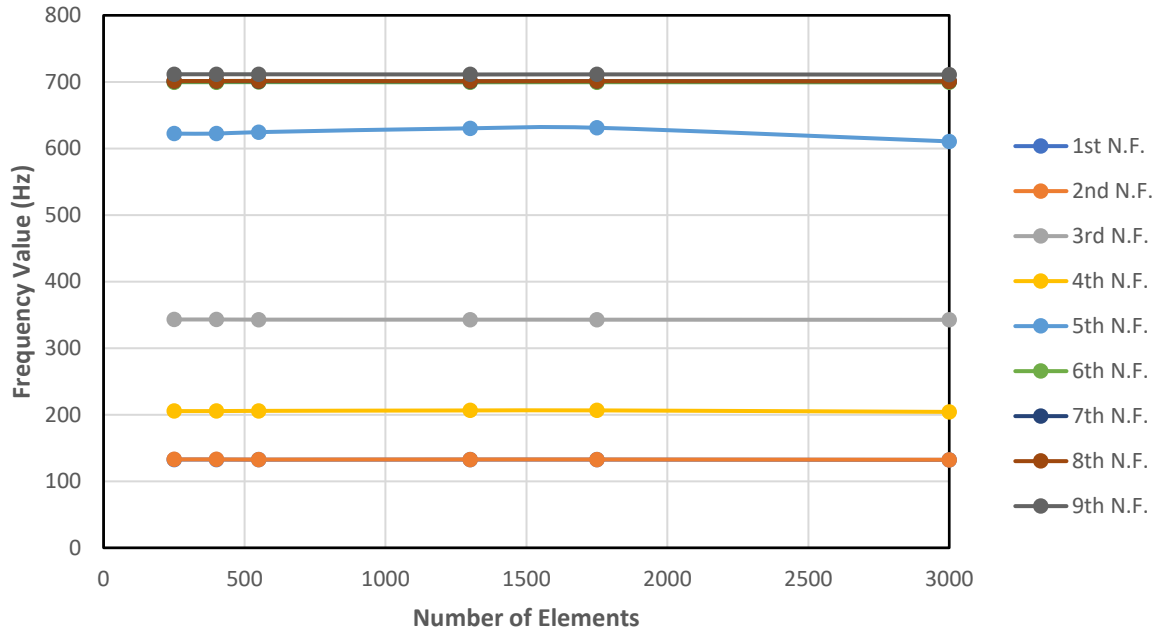


Figure 5.13. Modal results of the first 9 modes of the rotor model at 20000 RPM shown the effect of increasing the number of mesh elements.

The natural frequency values in Figure 5.9 through Figure 5.13 show only slight variations with increasing elements. This is expected since Figure 5.8 illustrate that the variation in blades' mesh is minimal across the six cases and most of the changes are taken place in the disk area. But the disk is considered rigid in the frequency span under study. Thus, the influence of the variation on the modal results is minimal since the disk experiences minimal internal deflections at the testing frequency span. The variation in blade mesh, on the other hand, matters but it is not significant across the six cases.

Nevertheless, the results in Figure 5.9 through Figure 5.13 are converging with minimal variations once the number of elements passes the 1500. For this reason, the disk-blades structure was modeled with 1750 SHELL181 elements. This configuration is displayed in Figure 5.8 (e).

5.6. Constraints and Frame of Reference Selection

Upon meshing the model, the only step left prior to conduct the analysis is the application of constraints and loading. Following the assumptions made in Chapter 3, the displacement along the rotor axis of rotation is neglected. Consequently, the nodal displacement along the z-axis in *APDL*, *UZ*, are constrained for nodes 1 through 15. In addition, the torsional deflection in node 15 is constrained in order to match the model in [36].

The two bearings elements, modeled using *COMBI214* elements, had two nodes each, one that is connected to the shaft while the other node is grounded. The two nodes connected to the shaft are nodes 2, and 14 for the left bearing and right bearing, respectively. The other two nodes have all *DOF* constrained. All other *DOF* of the rotor are free.

This simplicity in applying the constraints on nodes is because the model is not built entirely of solid 3-D elements. In which case, the nodal constraint are inadequate and surface constraints must be applied to resemble the required boundary conditions. The full nodal constraints of the rotor are seen in Figure 5.14. It must be stated that this configuration of constraints is used in the validation study as well as all subsequent case studies conducted in this research.

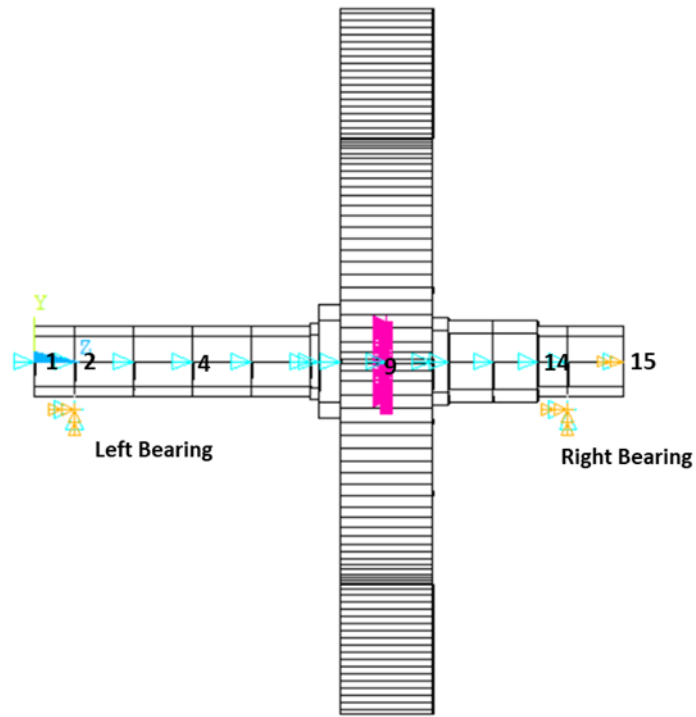
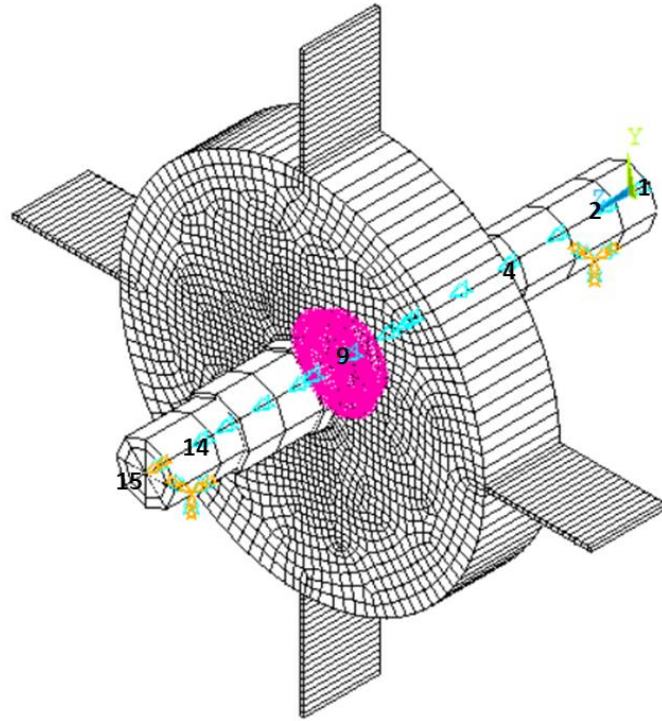


Figure 5.14. Rotor with constraints. The displacement along the axis of rotation is constrained in nodes 1-15, the torsional deflection is constrained in node 15 and all DOF are constrained in bearing's nodes.

Considering the rotational effects in *APDL* is a key parameter in the *Rotordynamics* module. Whether it was a modal, harmonic or transient analysis, the frame of reference in which the analysis is conducted must be specified. The rotational effects are accounted for as a result. In *APDL*, a stationary or a rotating frame of reference can be specified.

When a stationary reference frame is selected, *APDL* assumes the following form for the equation of motion of the structure [41],

$$[M]\{\ddot{u}\} + [G + C]\{\dot{u}\} + [K]\{u\} = \{F\} \quad (4.2)$$

where u is the generalized coordinate vector, $[M]$, $[C]$, $[K]$ and $[F]$ are the mass, damping, structural stiffness and external generalized forces matrices of the rotating structure, respectively, and $[G]$ is the gyroscopic effect matrix. The combined spin softening and centrifugal stiffening effects are not accounted for in the stationary reference frame analysis. To account for them, a pre-stress static analysis must be conducted prior to each run of the required analysis (i.e. modal, harmonic or transient).

On the other hand, when a rotating reference frame is selected, *APDL* assumes the following form for the structure equation of motion [41],

$$[M]\{\ddot{u}\} + [C + C_{coriolis}]\{\dot{u}\} + [K - K_c]\{u\} = \{F\} \quad (4.3)$$

where $[C_{coriolis}]$ is the Coriolis matrix, $[K_c]$ is the combined spin softening and centrifugal stiffening effect matrix and $\{F\}$ is the external forces matrix which now includes the Coriolis forces terms. The Coriolis matrix differs from the gyroscopic matrix in the sense that there is no moment generated due to the presence of two perpendicular rotations in the reference frame. Because of that, the separating (bifurcation) effect on the eigenmodes does not appear.

Although selecting the rotational reference frame has the advantage of including the combined effect of the spin softening and centrifugal stiffening effect directly, it comes with the disadvantage of losing the apparent effect the gyroscopic moment. In addition, *APDL* does not support generating Campbell diagrams and critical speed analysis for rotational frame of reference. For those reasons, and since Equation (4.2) better matches the global equation of motion developed for the rotor in Chapter 4, the stationary frame of reference is selected for all the subsequent analyses in this research. This selection result in accounting for the combined effect of spin softening and centrifugal stiffening for the entire structure and not only the blades as considered in Chapter 4. Nevertheless, neglecting the aforementioned rotational effects for the shaft and the disk during the theoretical formulation was done for convenience purposes to ease the formulation process. Accounting for all relevant rotational effects on the entire structure is believed to only enhance the practicality of the model and the accuracy of the simulation results.

5.7. Loading and Solution Controls

The discussion of loading is only appropriate in the context of the selected analysis. In Modal analysis, the only load applied to the system is rotation. The rotational velocity is applied on the global Z-axis, which coincide with the rotor axis of rotation. The applied rotational speed starts at 0.1Hz and goes up to 2000 Hz in twenty (20) step loads. Eleven (11) modes are extracted in each run using the mode-superposition engine solver (QRDAMP) to capture all the rotor coupled-vibrations-mode related to the blade's first bending mode. Using a for-loop operation, each modal analysis run is preceded by a pre-

stress static analysis to account for the combined effect of spin softening and centrifugal stiffness in the modal results.

In harmonic analysis, both rotation and synchronous forces are applied on the model to simulate unbalance scenario. It is the interest of this research to investigate the coupling in vibrations among the blades-bending and shaft-lateral deflections. Thus, the unbalance forces applied on the rotor are chosen to be along the lateral direction (x and y-axes) to excite the lateral modes of the shaft and pronounce the influence of blade-defects cases on the desired coupling modes.

To that end, synchronous lateral forces equal to 10% of the disk mass ($\sim 0.042 N$) is applied to the node where the disk is attached to the shaft (node 9) as seen in Figure 5.15. The response to this excitation is collected at node 4 and node 12 in the form of lateral nodal displacement.

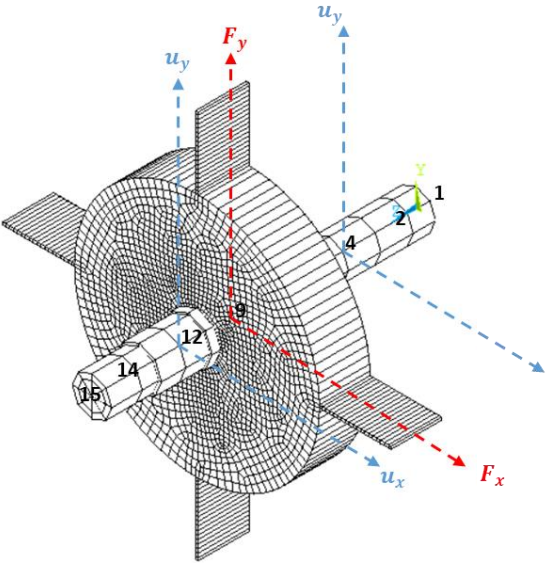


Figure 5.15. Rotor model with harmonic excitation. The dashed red lines resemble the excitation force and the dashed blue lines resemble the collected response values.

The synchronous unbalance excitation can be expressed in the following form,

$$\{\vec{F}_{Harmonic}\} = m e \omega^2 \begin{Bmatrix} \cos(\omega t) \\ \sin(\omega t) \end{Bmatrix} \quad (4.4)$$

where m is the unbalance mass, e is the eccentricity and ω is the rotation speed. Via the SYNCHRO command, *APDL* allows running harmonic analysis of multiple runs considering a varying rotational speed. Using this feature, multiple runs of the harmonic analysis is conducted for each study case in this research considering running speeds ranging from 0 to 1000 Hz with 500 load steps.

5.8. Test Cases

Using the developed rotor model in *APDL*, three blade-defect modes are simulated with the intention to investigate the influence of each defect on the shaft lateral vibrations. The influence is investigated through modal and harmonic analysis results as explained earlier. The defect cases are graphically presented in the following subsections.

5.8.1 Broken Blade

The first simulated blade-defect is a broken blade case. The defects are simulated by arbitrarily reducing the length of the broken blade. Two scenarios are simulated in this case. In the first scenario, the top blade was shortened from 82 mm into 40 mm (48% of original length). In the second case, the top and right blades were shortened into 40 mm, while the bottom blade was shortened into 20 mm (24% of original length) as seen in Figure 5.16.

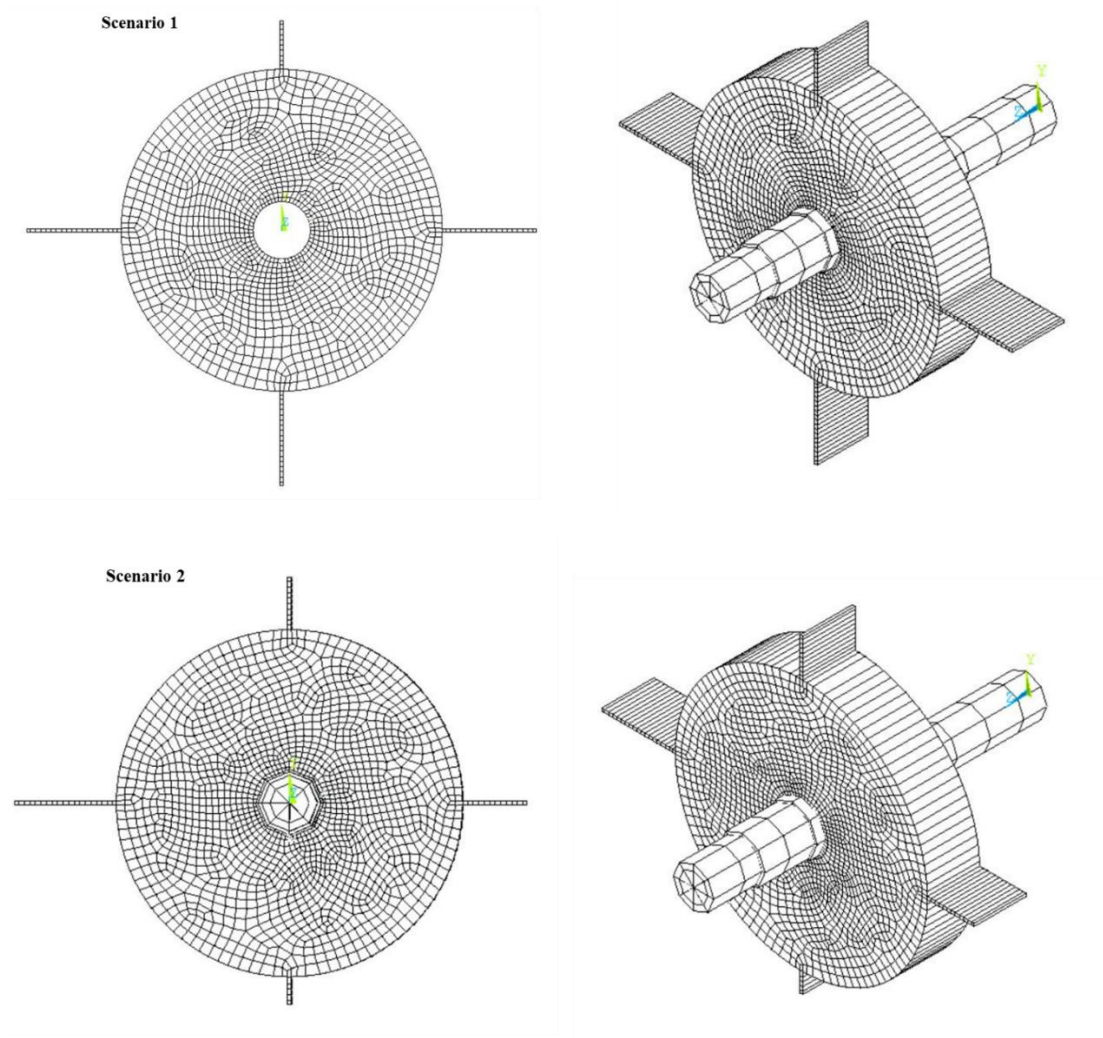


Figure 5.16. Rotor model with broken blades scenarios.

5.8.2 Pitted Blades (Blades with holes)

The second simulated blade-defect is a pitted blade case. This defect is simulated by creating three small holes of 2.5 mm diameter in blades. The holes centers are 20mm apart along the blade longitudinal axis. Pitting usually occurs along the transverse axis of the blades due to interaction with the flow, but because the blades are modeled as an extruded 2-D plane, modeling transverse holes is not feasible.

Similar to the broken-blade case, two scenarios are simulated, a single and three broken blades out of four. The two scenarios are shown in Figure 5.17.

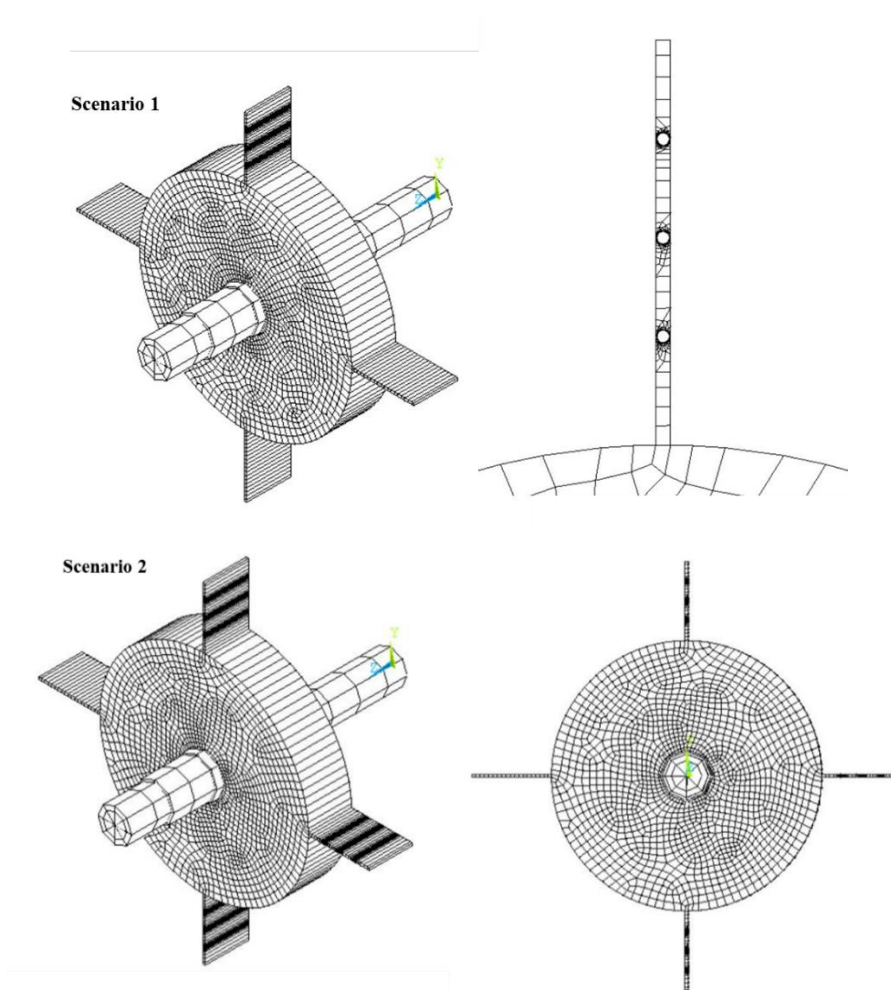


Figure 5.17. Rotor model with pitted blades scenarios.

5.8.3 Bent Blades

The last simulated blade-defect is a bent blade case. This defect is simulated by modeling the defective blades as an arch (a partial circumference of a circle with a radius of 52.2 mm) instead of a straight rectangle while maintaining the original length of the blade (82 mm). Similar to the previous defect case, two scenarios are simulated, a single and three defective blades out of four. The two scenarios are shown in Figure 5.18.

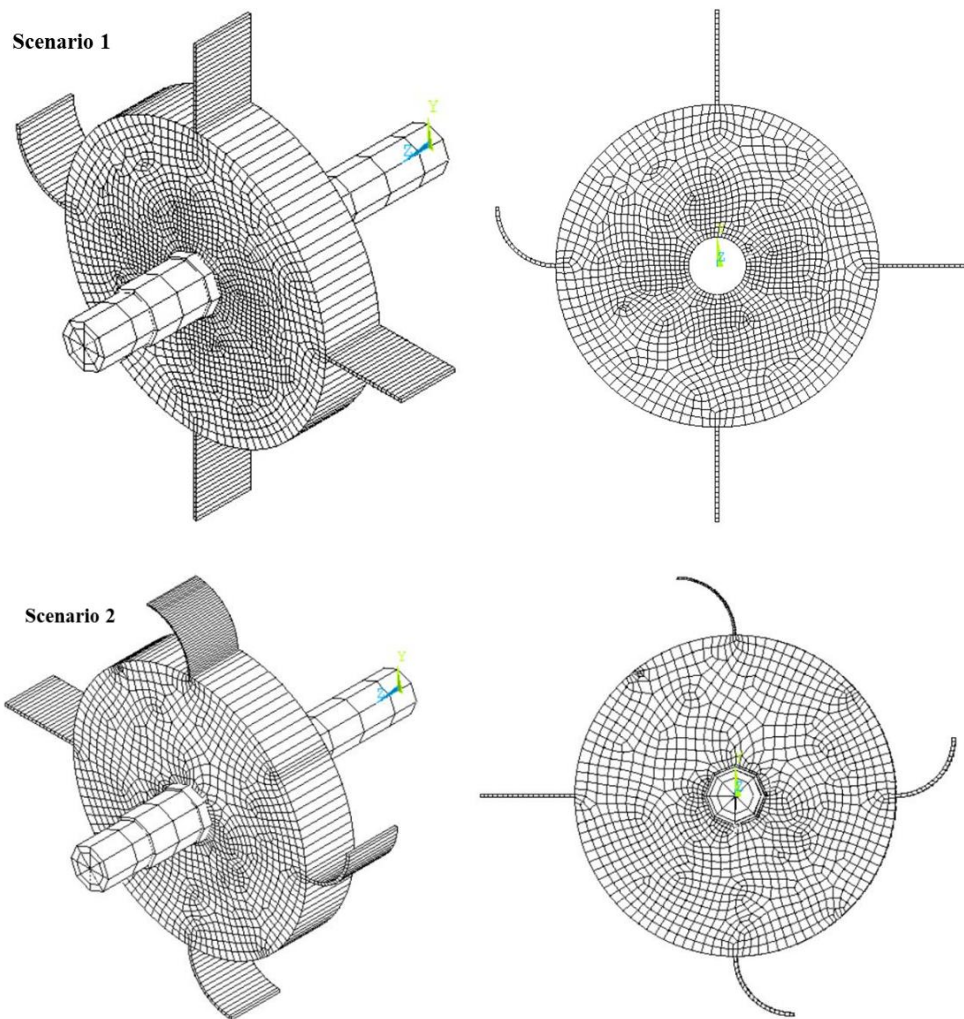


Figure 5.18. Rotor model with bent blades scenarios.

CHAPTER 6

VALIDATION OF THE MODEL

This chapter addresses the validation of the developed Shaft-Disk-Blade (SDB) rotor model using *ANSYS* Parametric Design Language (*APDL*). The validation of the model is done by comparing the results with those obtained by Hui Ma, et al. in [36] in the modal analysis, considering the effect of rotation.

6.1. Model Parameters Comparison

The benchmarked model from [36] is shown in Figure 6.1 alongside the developed rotor model. All shaft parameters, including the element type, mesh size and nodal constraints are identical in the two models. All disk parameters are identical, except for the mesh shape and number of elements. The coupling between the shaft and the disk is equivalent in the two models. Bearing characteristics are also equivalent in the two models. Only blades are different among the two models in terms of geometry, orientation and mesh. Table 6.1 list the differences between the two models' blades.

Table 6-1. Blades' Difference between Research and Benchmarked Model

Parameter	Research Model	Benchmarked Model
Material	Steel	Steel
Dimensions	82 × 58 × 3 mm	82 × 44 × 3 mm
Stagger Angle	0	25° from x-axis
Meshing Element	SHELL181	BEAM188
Number of Elements	20	4
Connection to Disk	2 sharing nodes	1 sharing node

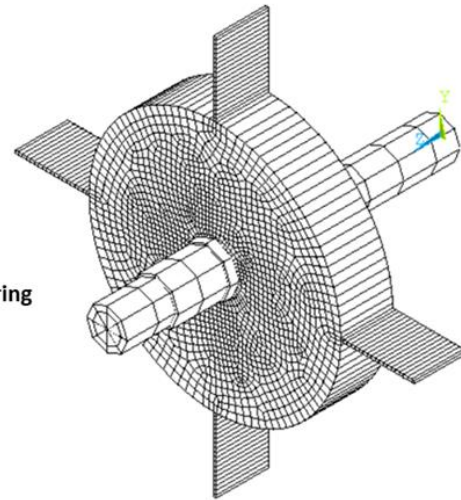
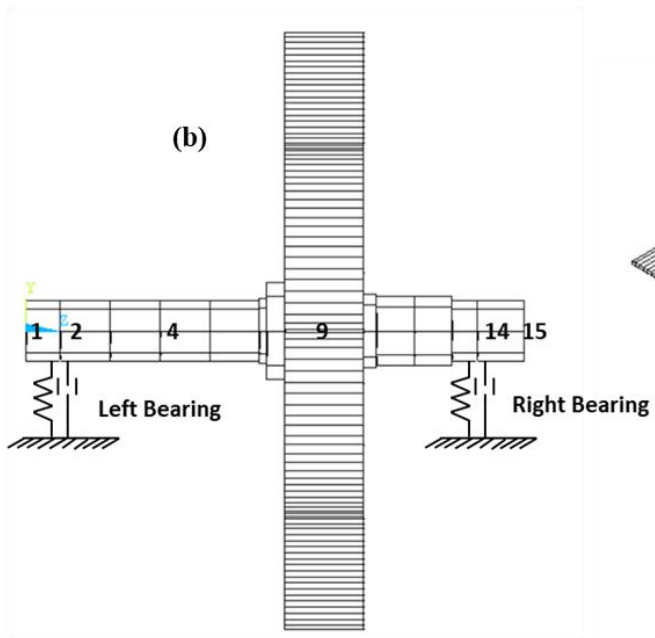
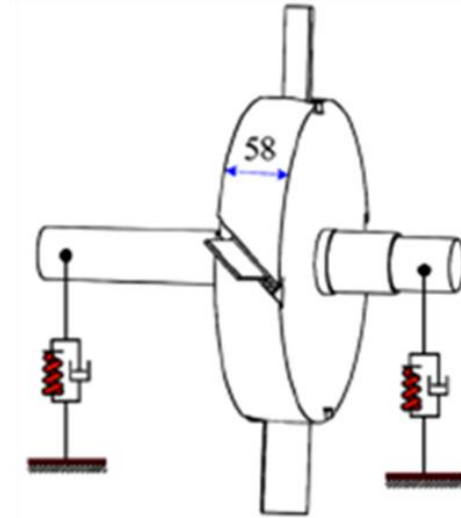
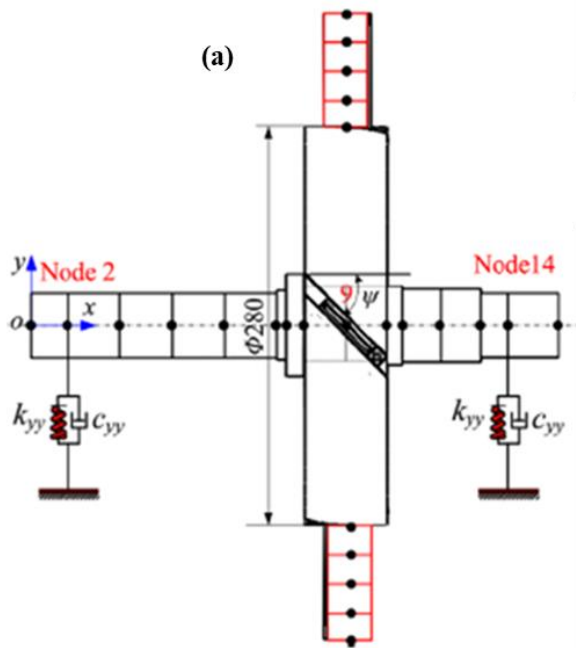


Figure 6.1. Graphical model comparison: (a) Benchmarked model [36] (b) Research model.

6.2. Modal Results Comparison – No Rotation

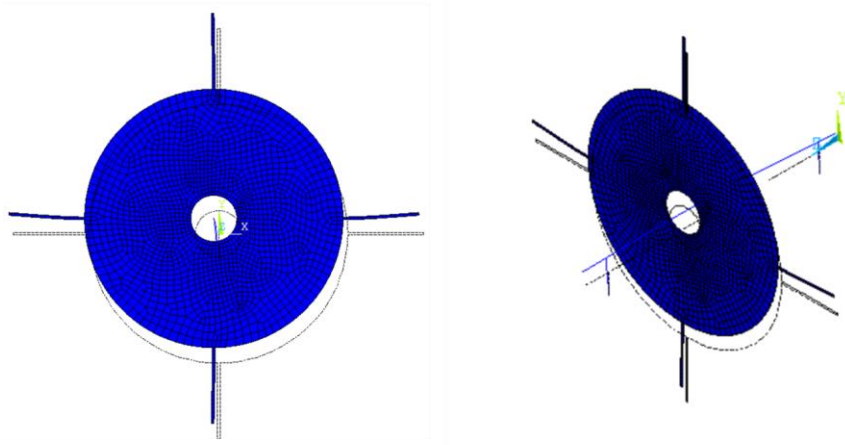
The modal analysis in the validation study is conducted using the solution controls specified in Chapter 5. Table 6.2 lists the first 9 modal results of the research model as compared with the benchmarked model in [36].

Table 6-2. First 9 Mode Shapes of the Non-Rotating Research Model as Compared to the Benchmarked Model

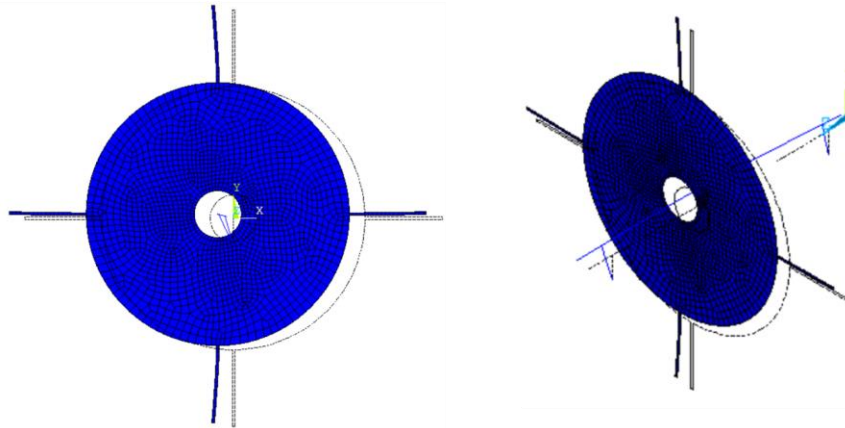
Mode Shape	Frequency Value (Hz)		Error %	Mode Shape Description
	Research Model	Model in [36]		
1	132.552	133.49	0.70	Pitching in lateral direction
2	132.552	133.49	0.70	Pitching orthogonal to Mode 1
3	154.776	159.75	3.11	Torsional vibration
4	262.989	267.38	1.64	Disk swing
5	263.009	267.38	1.63	Disk swing orthogonal to Mode 3
6	332.654	361.21	7.91	Blade-Blade coupling mode
7	333.512	363.4	8.22	Blade bending - shaft lateral
8	333.545	363.4	8.22	Blade bending - shaft lateral orthogonal to Mode 7
9	341.054	366.97	7.06	Blade bending - Shaft Torsional

From Table 6.2, it is observed that the first 5 mode-shapes relate to the vibrations of the entire structure, whereas the last 4 modes are dominated by s blades vibration. This is demonstrated by examining the mode shapes graphically. The first five modes are shaft-disk-dominated modes, 2 shaft lateral, 1 shaft torsional and 2 disk-swing modes as seen in Figure 6.2 and Figure 6.3.

(a)



(b)



(c)

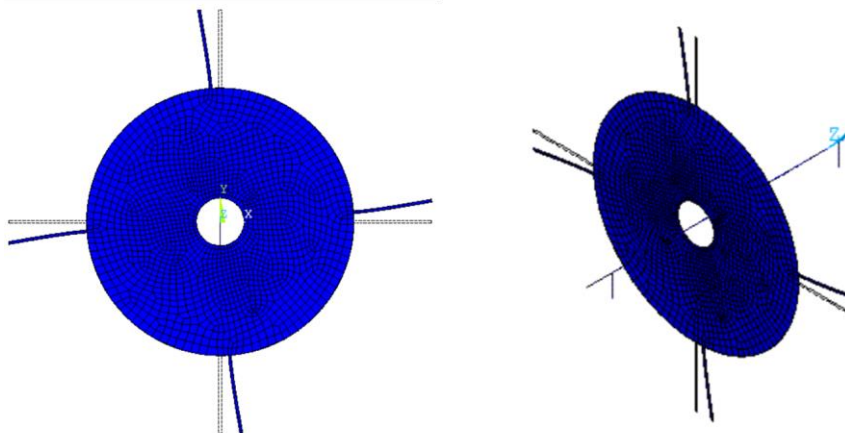
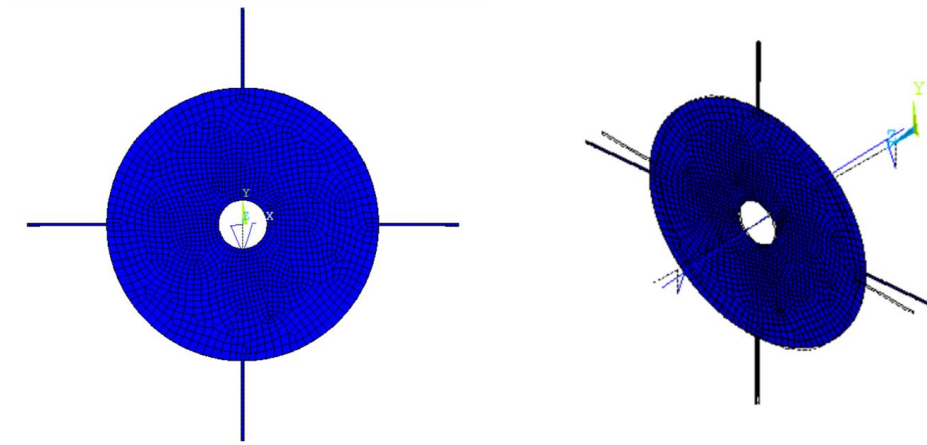


Figure 6.2. Shaft-disk-dominated mode shapes at 0 speed: (a) 1st mode (b) 2nd mode (c) 3rd mode.

(a)



(b)

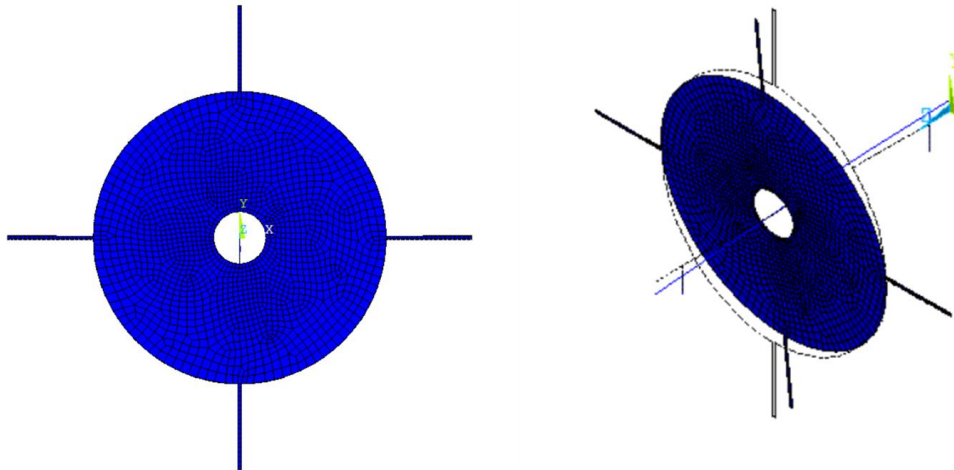
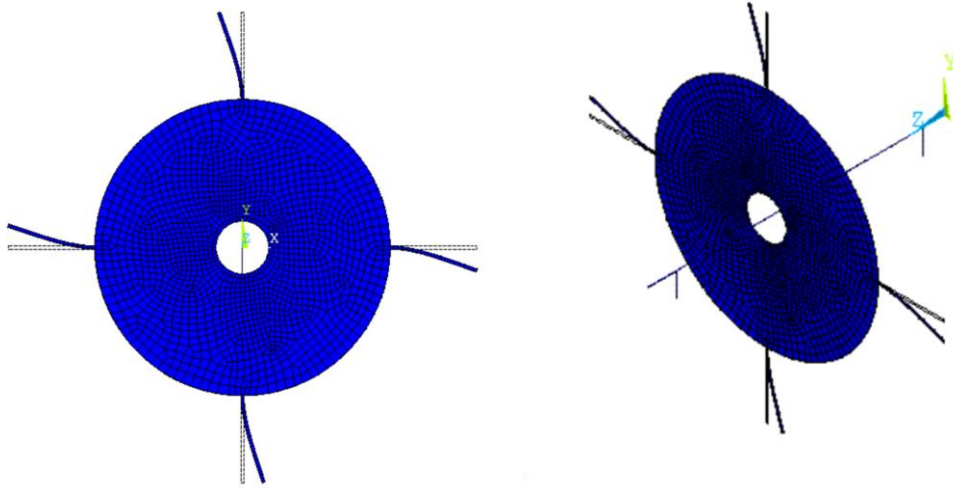


Figure 6.3. Shaft-disk-dominated mode shapes at 0 speed: (a) 4th mode (b) 5th mode.

Modes 6 through 9 are blade-dominated mode shapes linked to the blade's first bending mode as seen in Figures 5.4 and 5.5. Here, we note that the modes are repeated four times, equal to the number of blades. Mode 6 is a blade-blade coupling mode where neither the disk nor the shaft seems to be impacted by. Mode 7 and 8 are orthogonal to each other and they couple blade-bending to shaft-lateral vibrations. Mode 9 are a coupling mode among blade-bending and shaft-torsional vibrations.

(a)



(b)

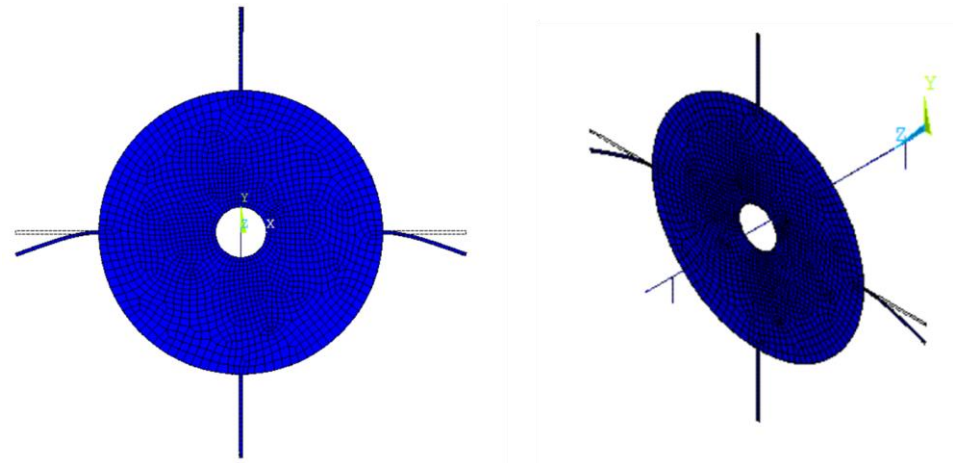


Figure 6.4. Blade-dominated mode shapes at 0 speed: (a) 6th mode (b) 7th mode.

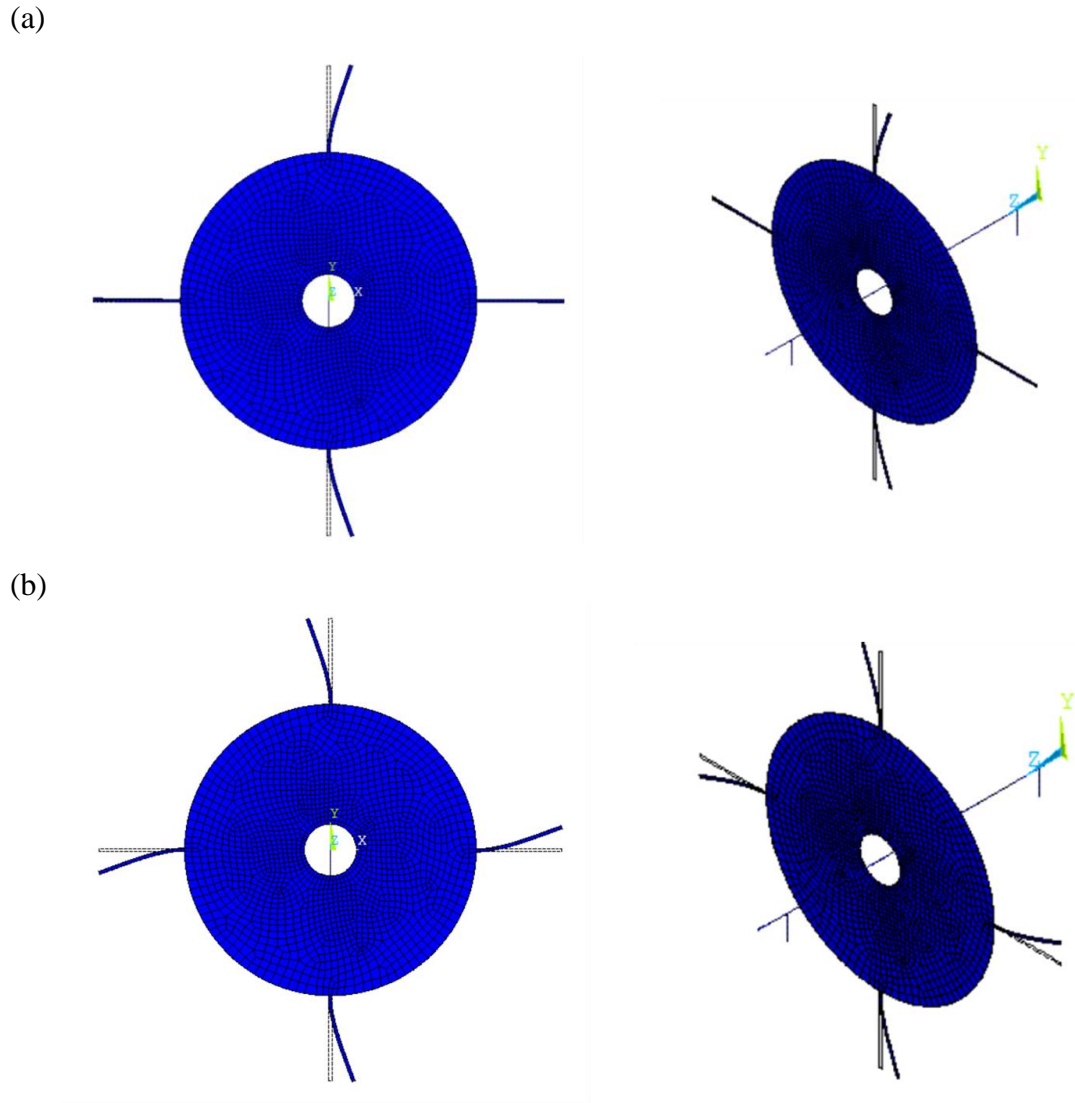


Figure 6.5. Blade-dominated mode shapes at 0 speed: (a) 8th mode (b)9th mode.

The higher mode shape that comes after the 9th mode are the shaft second bending mode at around 1014 Hz. Those modes are not coupled with the blade first bending mode and thus, they fall beyond the scope of this research, which is now set to be ranging from 0 to 1000 Hz.

As for the comparison with the model in [36], the obtained modal results at zero speed agree very well with those of [36] in the first 5 modes with a maximum error of 3%. The error value increases in the blade-dominated modes to reach a maximum of around 8%.

This is owing to the differences among the blade's in the two models. To further investigate this difference, a modal analysis is conducted for a single blade to calculate the natural frequency values corresponding to the first bending mode and the blade's higher modes as well. The blade is clamped from the end where it is normally connected to the disk and free from the other end. The first 4 mode shapes are extracted using the QRDAMP eigen solver and the results are presented in Table 6.3 and Figure 6.6.

Table 6-3. First 4 Mode Shape Results of a Non-Rotating Single Blade

Mode	Natural Frequency (Hz)	Mode Description
1	339.85	First bending mode (Flapping)
2	1061.32	First torsional mode (Twisting)
3	2171.15	Second bending mode
4	3594.46	Second torsional mode

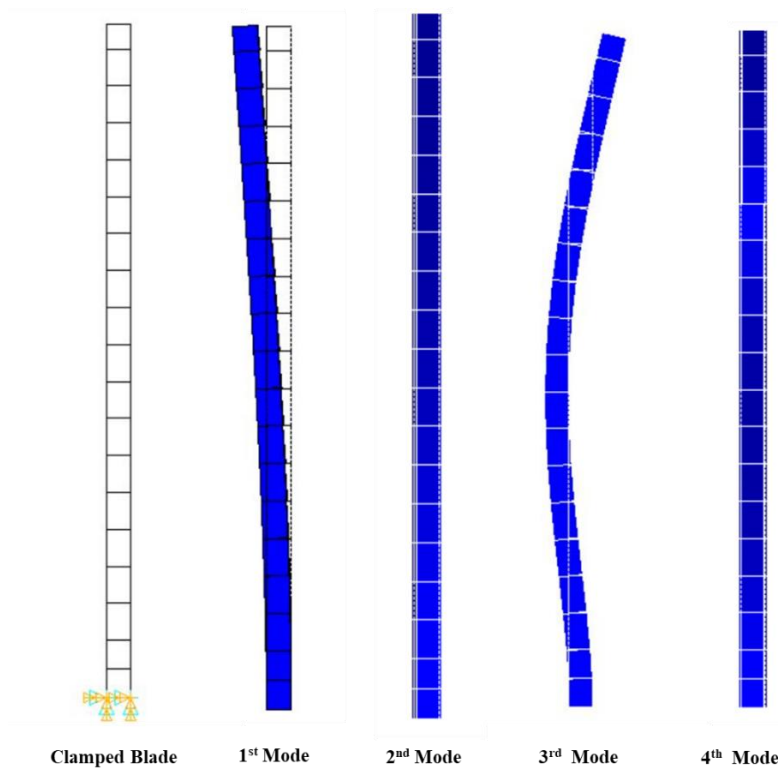


Figure 6.6. First four mode shapes of a single clamped-free blade.

From Table 6.3, the frequency value corresponding to the first bending mode of the blade is at 339.9 Hz. This value is close to the four values of the blade-dominated mode shape. Similarly, it was reported in [36], that the frequency value corresponding to the blade's first bending mode is 364.6 Hz which matches the model's blade-dominated mode shape frequency values reported in their work.

The blades used in this research had a higher thickness (58 mm) than that in [36] (44 mm). This results in making the blade in this research of a higher mass, thus reducing its natural frequency values. The stagger angle affects the coupling between the blades and the shaft as explained in Chapter 5. The 25° stagger angle in the benchmark model will essentially reduce the coupling between the blades and the shaft in Mode 7, 8 and 9 according to Equation (4.63). The effect of that on the error values is not clear and cannot be investigated because the 2-D modeling technique used in this research does not allow for stagger angle alteration.

In summary, the geometrical differences between the two model are likely the reasons to the difference in the last four modes between the models. Nevertheless, this does not indicate lower capabilities of the developed model in this research as long as the four blade-dominated mode are consistent with that of the single blade, which is found true. Therefore, the developed model is considered in agreement with the one in [36] at zero speed.

6.3. Modal Results Comparison – with Rotation

To test the model in running conditions, a modal analysis including rotation is conducted for comparison with the model in [36]. The rotation speed range at which the analysis in [36] was conducted is from 0 to 20,000 RPM. In real application, only jet engines can sustain a speed of 20,000 without running into stability issues. For that, a separate modal analysis is done on a single clamped-free blade, with the speed applied to the original spin axis, to ensure its stability across the full range of speeds (0-20,000 RPM). The results of the analysis are seen in Figure 6.7 in the form of Campbell diagram.

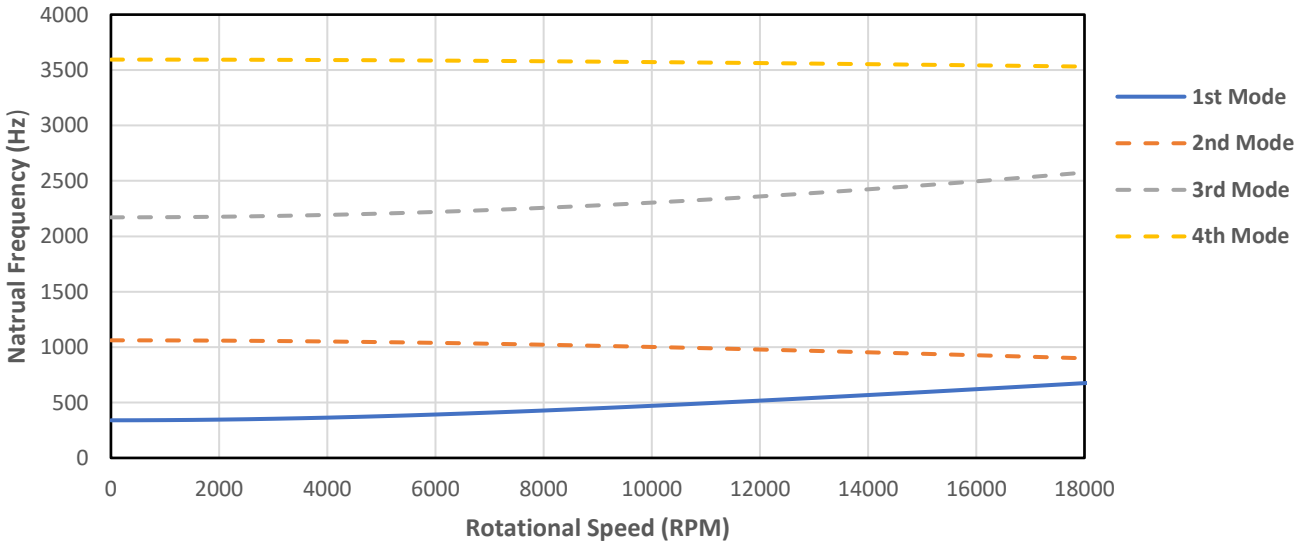


Figure 6.7. Campbell diagram of a single clamped-free blade.

The Campbell diagram in Figure 6.7 indicates that the blade is stable with no signs of instability across the full speed range of interest. In addition, the combined effect of spin softening and centrifugal stiffening is apparent on the first bending mode as the frequency values seem to increase with increasing speed. This validates the capability of the model in capturing the rotation effects as desired.

The results of the modal analysis of the full rotor model are shown in Figure 6.8 and, for comparison reasons, the result reported in [36] are shown in Figure 6.9.

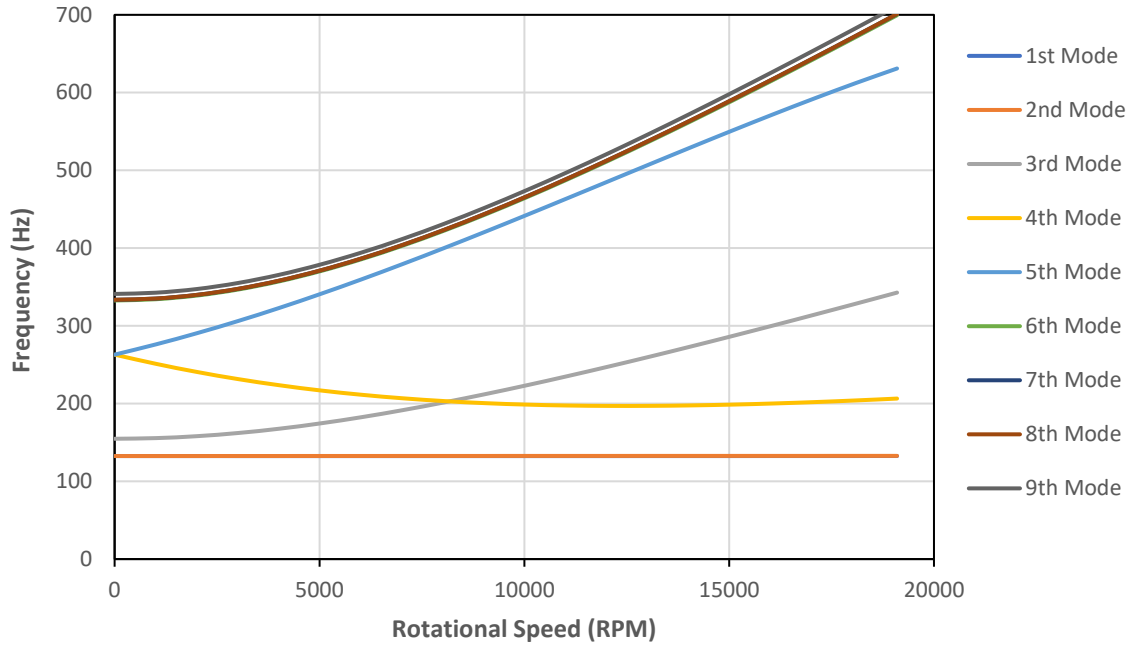


Figure 6.8. Campbell diagram of research model.

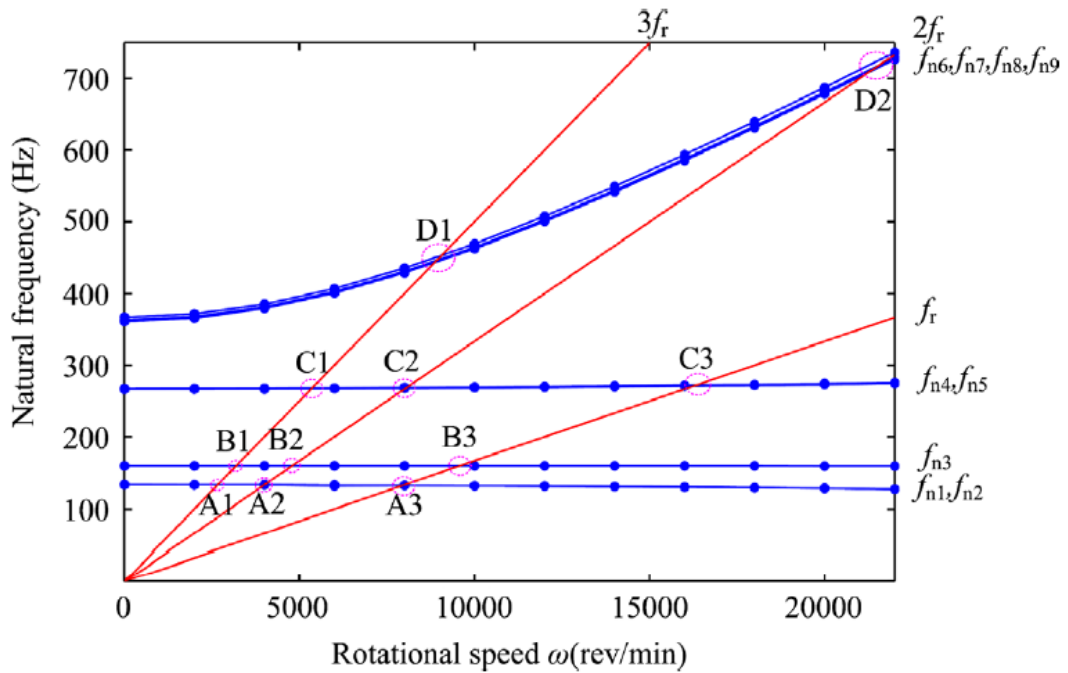


Figure 6.9. Campbell diagram of the model in [36] as reported. f_r donates the 1X line and n correspond to the mode number (1-9) as seen in Table 6.2.

In Figure 6.8, several findings were observed. First, the first and second mode shapes are not influenced by rotation. This means that they are not subject to the gyroscopic effect nor the other rotation effects. This is matched by the model in [36] as seen in Figure 6.9. Second, the third mode increases with increasing speed in a similar behavior to the first bending mode of the single blade seen in Figure 6.7. This means that the third mode is subjected to the combined effect of the spin softening and centrifugal stiffening. That behavior is not seen in [36] owing to the fact that the combined effect of the spin softening and centrifugal stiffening was only included for the blades. Third, the disk-swing modes (Mode 4 and 5) bifurcate from each other with increasing rotational speed. This bifurcation phenomenon is due to the presence of the gyroscopic moment that result in a split in the backward and forward natural frequencies of the same eigenvalue [15]. This behavior is again not captured in [36] as seen in Figure 6.9. That is because, in [36], the gyroscopic effect was not included in the entire analysis. It is also noted in Figure 6.8 that the blade-dominated modes (Mode 6,7,8 and 9) are all clustered in almost a single curve and behave similar to the first bending mode of a single blade in Figure 6.7. The frequency values of the modes increase with increasing rotational speed due to the combined effect of the spin-softening and centrifugal-stiffness. The same behavior is observed in [36] which validates the capabilities of the model to capture the rotatory inertia effect on blades during rotation. The frequency values at 1000 and 2000 RPM are compared to those in [36] in Table 6.4.

Table 6-4. Modal Results Comparison between the research model and that in [36] at 1000 and 2000 RPM

10000 RPM				20000 RPM			
Mode	Research Model	Model in [36]	Difference %	Mode	Research Model	Model in [36]	Difference %
1	132.36	133.49	0.84	1	132.16	133.49	1.00
2	132.57	133.49	0.69	2	132.33	133.49	0.87
3	223.39	159.75	39.84	3	342.61	159.75	114.46
4	197.69	267.38	26.07	4	204.25	267.38	23.61
5	437.34	267.38	63.56	5	610.62	267.38	128.37
6	463.41	460.9	0.54	6	699.22	668.3	4.63
7	464.56	461.7	0.62	7	700.84	669.4	4.70
8	464.59	461.7	0.63	8	700.87	669.4	4.70
9	472.517	468.2	0.92	9	710.95	678.6	4.77

Considering the aforementioned explanation of the differences seen in Table 6.4, it is safe to conclude that the developed rotor model achieves a comparable accuracy when compared to the model in [36] in modal results and surpasses it in the sense that it accounts for the gyroscopic, spin softening and centrifugal stiffening effects on the entire structure.

6.4. Effect of Increasing the Number of Blades

To further examine the validity of the developed model, the effect of increasing the number of blades is studied. Therein, a modal analysis is conducted on a shaft-disk system with no blades, a rotor with four, five, six and seven blades as seen in Figure 6.10. The blades are evenly distributed around the disk. The effect of rotation on modal results is considered.

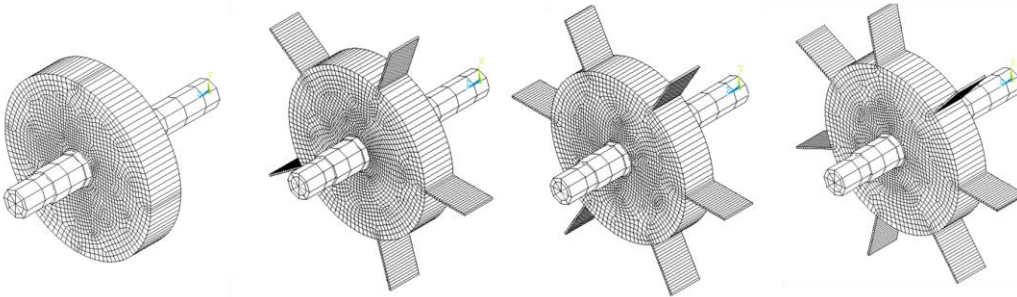


Figure 6.10. From the left: model with no blades, with five blades, with 6 blades, with 7 blades.

Table 6-5. Modal Results At 0-Speed for a Rotor with Increasing Number of Blades

Mode	Frequency (Hz)				
	No Blades	4 Blades	5 Blades	6 Blades	7 Blades
1	133.60	132.55	132.31	132.06	131.82
2	133.60	132.55	132.31	132.06	131.82
3	159.77	154.78	153.66	152.51	151.44
4	268.77	262.99	261.66	260.33	259.03
5	268.77	263.01	261.66	260.33	259.05
6	-	332.65	333.52	332.66	332.51
7	-	333.51	335.38	333.08	332.74
8	-	333.55	344.87	333.97	333.14
9	-	341.05	346.39	337.99	337.55
10	-	-	353.04	346.55	345.09
11	-	-	-	352.71	346.14
12	-	-	-	-	354.90

The modal results of the 5 rotor models at 0-speed are listed in Table 6.5. Examining the values, we first observe that all models share the first 5 modes regardless of the number of blades. This is expected since the only variation among the models is the number of blades, which we expect to influence only the blade-dominated modes. Nevertheless, the frequency values of first five modes seem to decrease slightly as the number of blades increases. This is likely owing to the increased effective mass of the system induced by each additional blade. Another factor could be that the bending modes of the blade act as springs in parallel with the shaft, which ultimately reduces the effective stiffness of the system, resulting in a decrease in the natural frequency [15]. It can also be observed that with the addition of each blade, an additional mode shape appears that correspond to the blade first bending mode shape, which further validates the finding stated earlier that their exist a number of blade-dominated mode shapes that is equal to the number of blades in the model.

The modal results including the effect of rotation for the model with no blades and with four blades are shown in the form of Campbell diagram in Figure 6.11. Aside from addition of the blade-dominates modes, there does not appear to be a significant difference between

the two models. Similar observation is made for the models with higher number of blades.

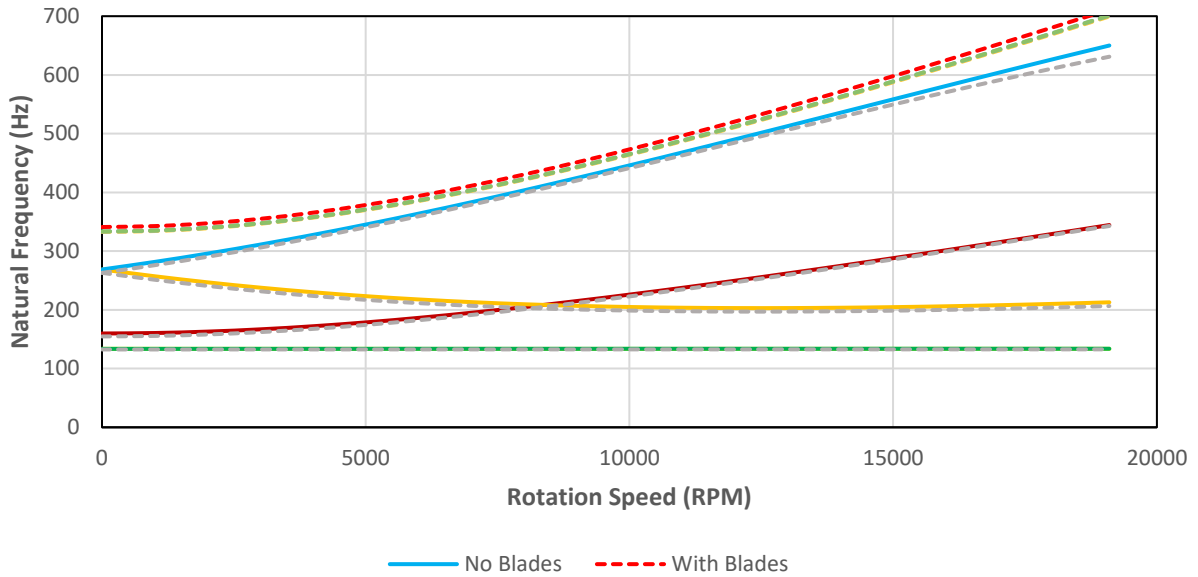


Figure 6.11. Campbell diagram of first 9 modes of the rotor with four blades as compared to a rotor with no blades.

The aforementioned findings are in line with the theoretical work done in Chapter 3 and 4 and in accordance with the findings highlighted in [36], [15] as well as other similar work done in this field of research. This help asserting that the model is fully capable of simulating the dynamical response of the model as desired and can be used to carry out the subsequent blade-defect case studies.

CHAPTER 7

BLADE-DEFECT CASE STUDIES

In this chapter, the results of the blade-defect case studies are discussed. The objective is to investigate the influence of each defect case on the mode shapes of the Shaft-Disk-Blades (SDB) rotor model and ultimately evaluate the feasibility of detecting the existence of each defect through analysis of the shaft lateral vibrations. The first part of the objective is achieved through modal analysis, whereas the second part is looked at using harmonic analysis. In both analyses, the results of each defect-case are benchmarked against those of a healthy shaft and differences are highlighted. At the end of the chapter, the overall findings are summarized.

7.1. Modal Analysis – No Rotation

Considering the cases where only a single blade out of four is defected, the modal results of each defect case in addition to those of the healthy rotor model are listed in Table 7.1. Examining the modal results, it can be observed that the first 5 mode shapes are not greatly influenced by blade-defects, with the exception of the broken blade case where the values seem to be slightly larger than those of the healthy blade. This is due to the decrease in the effective rotor mass because of the broken blade. This decrease in the effective mass results in a slight increase in the frequency values of the all mode shapes.

Table 7-1. Modal Results of a Single-Blade Defect in Comparison with a Healthy Rotor Model

Mode	Frequency (Hz)			
	Healthy Rotor	Broken Blade	Pitted Blade	Bent Blade
1	132.55	132.67	132.57	132.55
2	132.55	132.69	132.57	132.58
3	154.78	155.57	154.86	155.00
4	262.99	263.00	262.99	262.81
5	263.01	264.63	263.15	263.45
6	332.65	-	332.95	332.94
7	333.51	332.96	333.58	333.60
8	333.55	333.50	337.96	338.98
9	341.05	339.13	348.20	387.06
10	-	-	-	955.77

In addition, in Table 7.1 we observe that the blade-dominated mode shapes are the most influenced by blade defects. This behavior was noticed in Chapter 6 where the increase of blade number influenced the blade-dominated modes. In the broken blade case, the blade-blade coupling mode disappears indicating a loss in symmetry among the blades. It is likely that this frequency value is shifted to a higher value that is outside the frequency range due to the reduction in blade length. All other blade dominated modes are not significantly affected. The pitted blade case is the least defect case that affects the blade-dominated mode shapes with no significant impact on any of the mode shapes. In the bent blade cases, the blade-bending shaft-torsional coupling mode increases significantly while the other modes remain close to the healthy rotor values. In addition, there exist an additional mode shape that is higher than the other four blade-dominated modes and it appear to be related to the bent blade first-bending mode shape.

To further investigate the additional mode appearing in the bent-blade case, a single bent-blade modal analysis is conducted. The blade is clamped at one the end where it is normally connected to the disk and free at the other end. The first 4 modal results at 0-speed are listed in Table 7.2 and Figure 7.1.

Table 7-2. First 4 Mode Shape Results of a Clamped-Free Bent Blade

Mode	Natural Frequency (Hz)	Mode Description
1	394.03	First in-plane bending mode
2	968.61	First out-of-plane bending mode
3	1902.69	Second in-plane bending mode
4	2552.20	Second out-of-plane bending mode

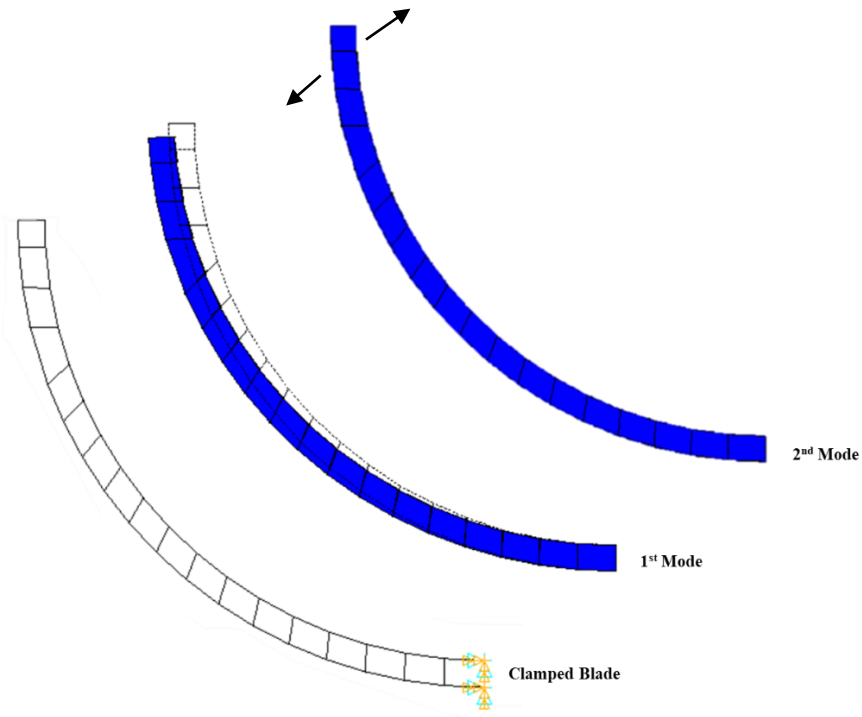


Figure 7.1. Mode shapes of a clamped-free bent blade. The second mode is not visible because it is out-of-plane.

The modal results of the clamped-free bent blade show that the first bending mode of the blade is shifted from 339.85 into 394.03 Hz. In addition, the twisting mode of the healthy blade is changed into an out-of-plane bending mode of a 968.61 Hz frequency. Those changes are likely due to the drastic alteration of the blade shape and they explain the rise in the blade-bending shaft-torsional vibration coupling mode of the rotor (Mode 9) and the existence of a new mode shape (Mode 10). The modal results at 0-speed for the cases when three blades are defected are listed in Table 7.3.

Table 7-3. Modal Results of a Three-Blades Defect in Comparison with a Healthy Rotor Model.

Mode	Frequency (Hz)			
	Healthy Rotor	3 Broken Blades	3 Pitted Blades	3 Bent Blades
1	132.55	133.00	132.60	132.62
2	132.55	133.03	132.60	132.64
3	154.78	157.29	155.03	155.76
4	262.99	264.48	263.15	263.58
5	263.01	267.08	263.31	263.94
6	332.65	-	334.38	335.07
7	333.51	-	340.01	388.4
8	333.55	335.20	344.08	399.0
9	341.05	-	349.09	401.9
10	-	-	-	551.3
11	-	-	-	989.5
12	-	-	-	992.3

Starting with the broken blades cases, the first five modes of the rotor show a further increase when compared to a single-broken blade case, which is, again, due to the decrease in the effective mass of the model. The increase reaches a maximum of 2% making it

insignificant. In addition, modes 6,7 and 9 do not appear in the results as they are shifted to higher frequency values due to the blade-length reduction. To summarize, broken-blade defect results in shifting blade-dominated modes to higher frequency values. The number of shifted modes is equal to the number of defective blades.

Pitted-blade defect, as observed from Table 7.3, remains the least defect-case that influence the modal result of the rotor, with a slight increase in the blade-dominated modal frequency values in the three defective blades case. This increase is likely due to the decrease of blade's mass with induced holes.

As for the bent-blades cases, we highlight several findings from the results in Table 7.3. First, the first five mode shapes are not influenced by the defect of three blades. Second, the blade-dominated modes are severely influenced in which only Mode 6 remains similar to that of a healthy rotor model. Mode 7,8 and 9 are increased to a maximum of 50% difference in value as compared to the healthy rotor model. New modes that are related to the blade in-plane and out-of-plane bending modes appeared similar to the case of a single blade. However, at the case of three blades, new modes appeared relating the bent-blades modes in an in-phase/out-of-phase manner. A graphical representation of the blade-dominated mode shapes of the bent-blades are shown in Figure 7.2 for illustration purposes.

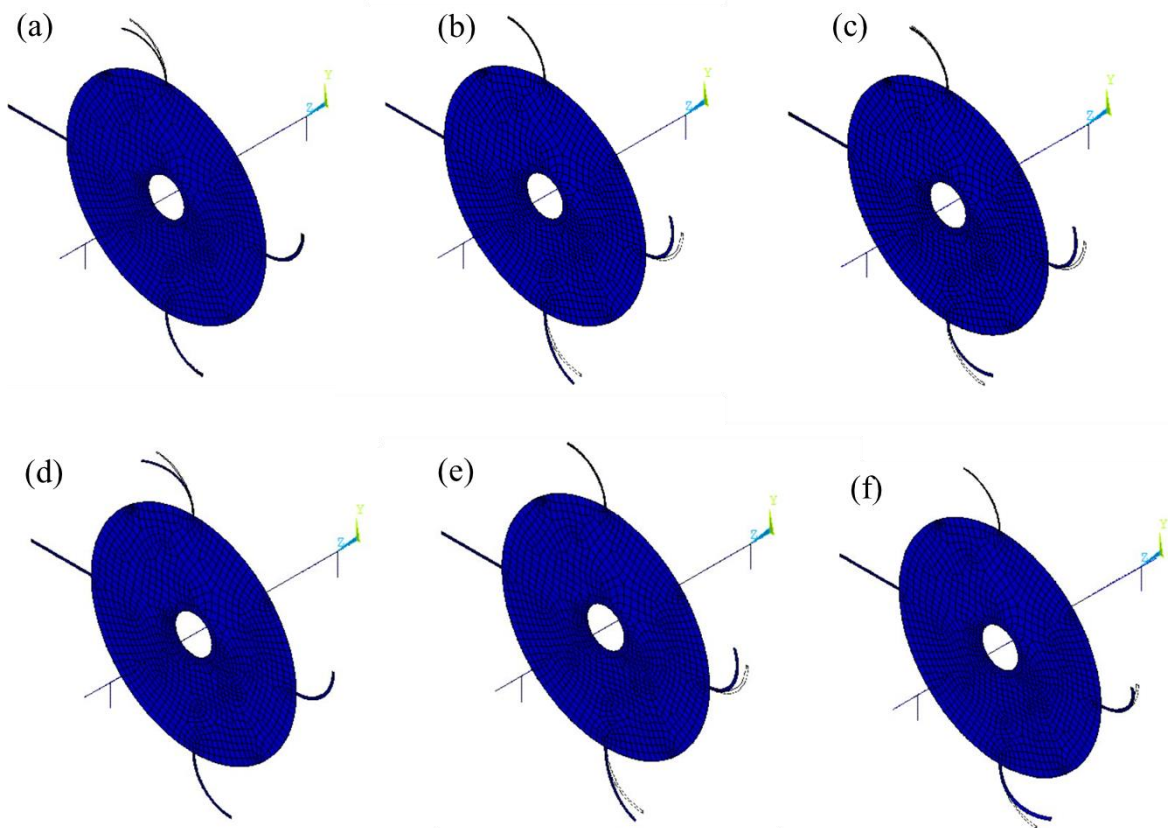


Figure 7.2. Mode representation of the model with three bent blades: (a) Mode 7 (b) Mode 8 (c) Mode 9 (d) Mode 10 (e) Mode 11 (f) Mode 12

In Figure 7.2, we observe that Mode 7 and Mode 10, are related to the top blade's first and second bending mode only, respectively. The frequency values of those modes are close to the first and second bending modes of a single-bent-blade as listed in Table 7.2. Modes 8, 9, 11 and 12 are coupling modes among the right and bottom blades. Mode 8 and 9 are related to the first bending, in-plane, mode of the right and bottom blades. The difference between the two, is that in Mode 8, the two blades are in-phase whereas in Mode 9, the two blades are out-of-phase. Similarly, Mode 11 and 12 are related to the blade-out-of-phase-bending modes, where Mode 11 resembles the in-phase motion, and Mode 12 the out-of-phase motion. This coupling among the defective blades only exist in the bent-blades case.

7.2. Modal Analysis – with Rotation

7.2.1 Broken Blades

The modal results of a single-broken blade including rotations are shown in the form of a Campbell diagram in Figure 7.3.

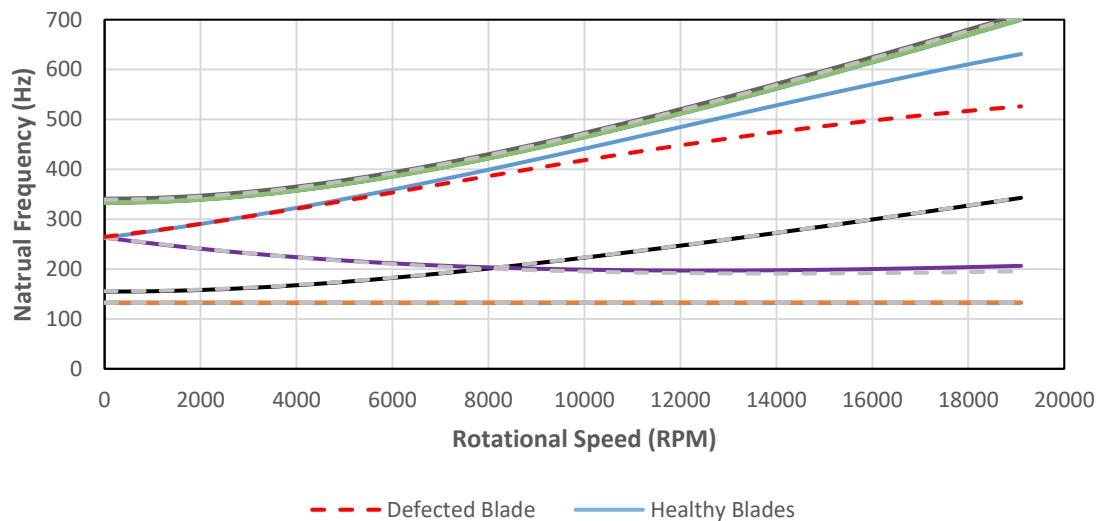


Figure 7.3. Campbell diagram of the model with a broken blade compared to a healthy rotor.

In Figure 7.3, we observe that there is no significant influence of having one broken blade on the Campbell diagram of the rotor. This is because, as stated earlier, the single broken blade case only results in a shift of one of the four blade-dominated mode shapes, which are usually close to each other and behave similarly (one clustered curve). Nevertheless, Mode 5 seems to be the most influenced mode shape in this defect-case. In Mode 5, the natural frequency values of the healthy and defected rotor start with similar values, but at around 5000 RPM they split, reaching a maximum of 16% difference in values at 20000 RPM. This effect could be because the gyroscopic effect on the defected rotor is lessened with the decrease of blade surface area.

Having three broken blades instead of one does not make significant changes either as seen in Figure 7.4. In fact, the split in Mode 5 between the two models gets less severe reaching a maximum of 5% in value at 20000 RPM.

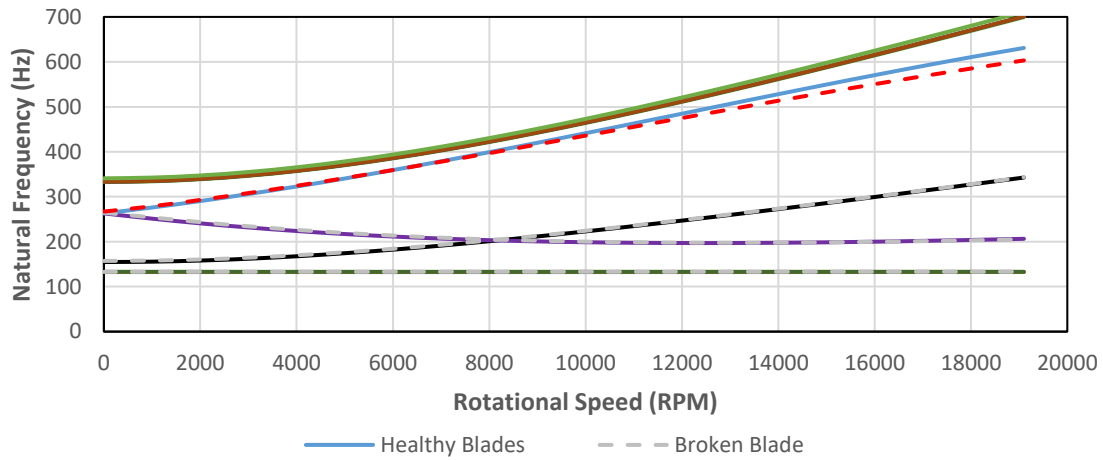


Figure 7.4. Campbell diagram of rotor with three broken blades compared to a healthy rotor.

7.2.2 Pitted Blades

The modal results of a single-pitted blade including rotations are shown in the form of a Campbell diagram in Figure 7.5.

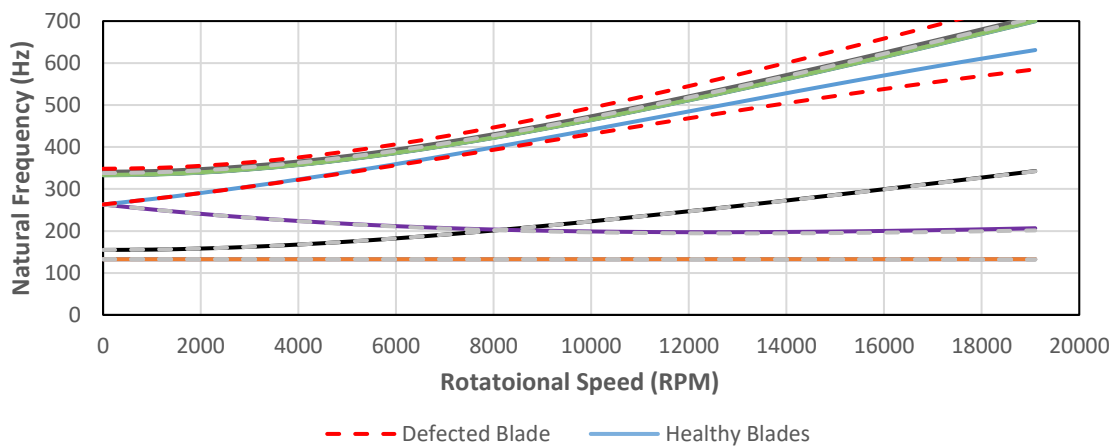


Figure 7.5. Campbell diagram of rotor with a pitted blade compared to a healthy rotor.

As stated earlier, the pitted-blade cases are the least in affecting the modal results among all defect cases. This still holds as the effect of rotation is considered as seen in Figure 7.5. Most mode shapes follow the behavior of the healthy rotor mode shapes with the exception of Mode 5 and Mode 9. Mode 5, similar to the case of the broken blades, appears to slightly split from the healthy rotor mode at around 12000 RPM with a maximum decreased in value of 7%. Mode 9, the blade-shaft torsional coupled mode shape, appears to also split from that of the healthy rotor at around 12000 RPM with increasing values of around 6%. The addition of 2 more defected blades do not alter the behavior of the Campbell diagram significantly as shown in Figure 7.6 when compared to Figure 7.5.

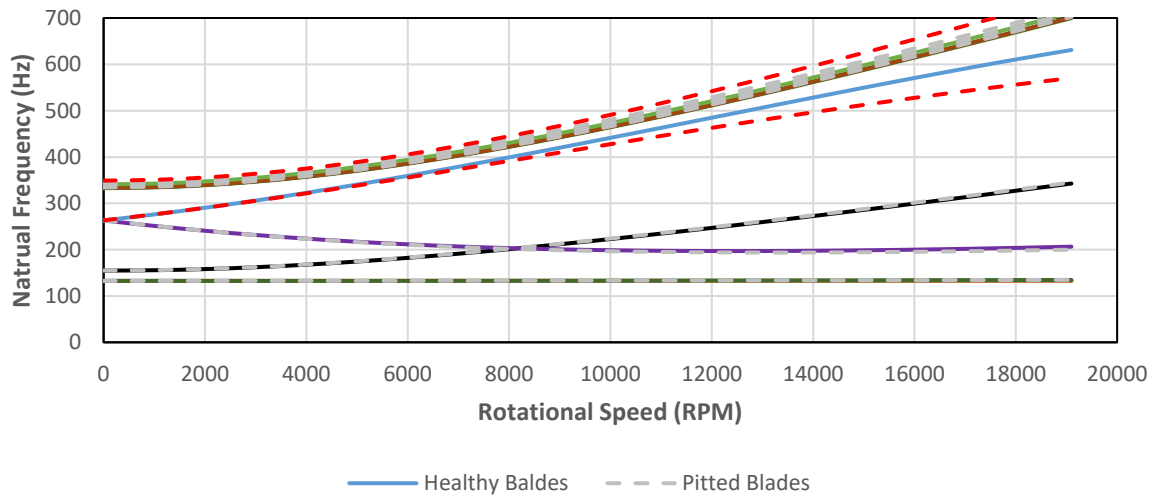


Figure 7.6. Campbell diagram of rotor with three pitted blades compared to a healthy rotor.

7.2.3 Bent Blades

The modal results of a single-bent blade including rotations are shown in the form of a Campbell diagram in Figure 7.7.

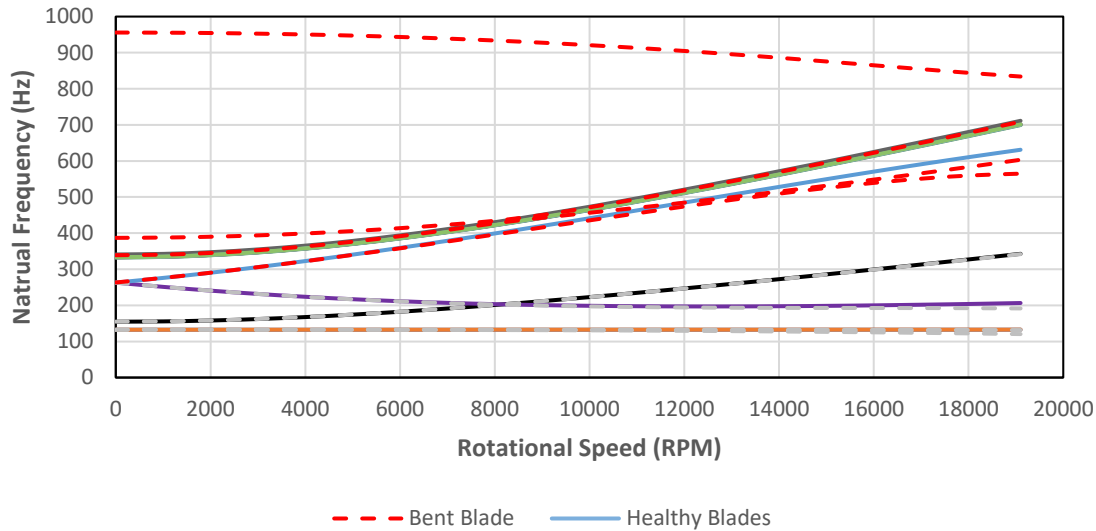


Figure 7.7. Campbell diagram of rotor with a bent blade compared to a healthy rotor.

From Figure 7.6, we observe the following. First, Mode 10, the emerging additional mode shape related to the out-of-plane bending mode of the bent blade, does not follow the behavior of the other blade-dominated modes as it slightly decreases with increasing rotation speed. Thus, it does not appear to be affected by the combined softening and stiffening effects in a similar fashion as the other blade-dominated mode shapes. In fact, it seems affected by the spin-softening effect more than the centrifugal stiffening effect. This could be due to the geometry of the blade that would alter the influence of centrifugal forces on the blade. Second, Mode 5 appears to slightly split from the healthy rotor mode at around 15000 RPM and decrease in value to reach a maximum of 10% difference at 20000 RPM. This behavior is observed in all defect cases and can be declared as a trend.

Increasing the number of bent blades from 1 into 3 seems to only exacerbate the influence of this defect case on the Campbell diagram as shown in Figure 7.8. Considering the blade-dominated mode shapes, it is observed that Mode 7, the second blade-dominated mode shape, starts to increase sharply as the rotational speed passes the 2000 RPM mark. At around 11000 RPM, the rate of increase decreases to follow that of a healthy blade-dominated mode shape. Mode 8 and 9 seem to follow the behavior of a healthy blade-dominated mode shape. Mode 10 decreases with increasing speed in what seem to be a dominant influence of the spin-softening effect.

In general, it is observed that bending blades have the most influence on the modal results of the rotor in the case of 0-speed and when rotation is applied. This finding is promising as such influence can lead to potential detection means of defect-presence through vibration analysis techniques as will be discussed subsequently.

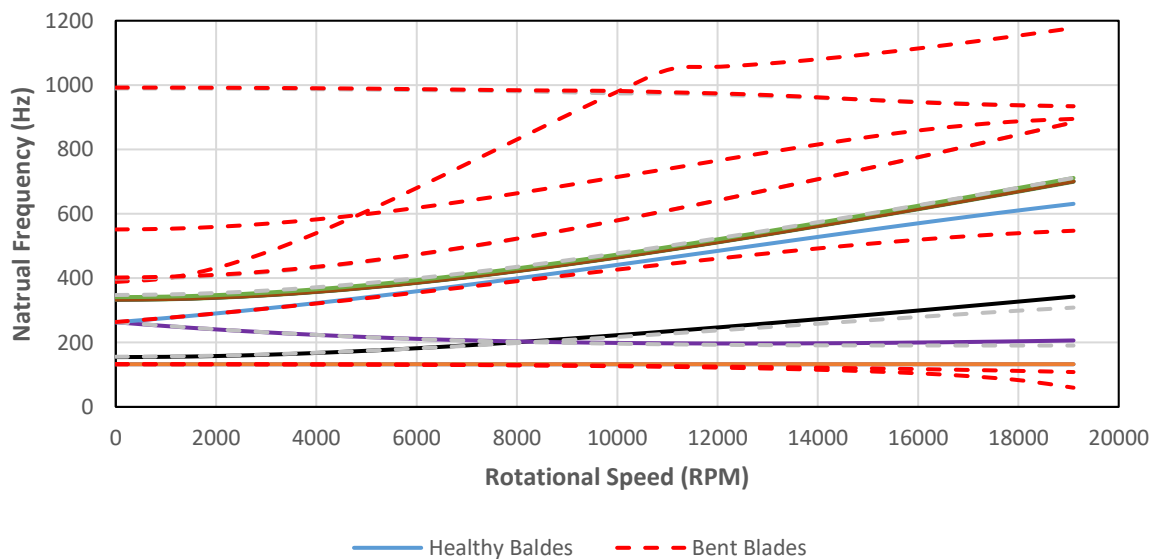


Figure 7.8. Campbell diagram of rotor with a bent blade compared to a healthy rotor.

7.3. Harmonic Analysis

Harmonic analysis of rotating structures resembles the analysis used in vibration monitoring program in real applications. It is a common practice in the rotating machine industry to assess the health of rotating equipment by monitoring the shaft vibrations through proximity probes [23]. Proximity probes provide a relatively inexpensive, less intrusive mean to monitor shaft deflections in the lateral direction, which makes them favorable for usage in the industry [33]. The underlying objective of this research is to facilitate detecting blade-defects through the interpretation of shaft lateral vibrations measurements.

The precedent modal analysis helped building a comprehensive understanding of the dynamic behavior of a healthy rotor and the influence of each blade-defect case on the overall system's vibrations. The harmonic analysis in this chapter complements the precedent findings and narrow the focus on the shaft lateral vibrations and its related mode shapes. To that end, this analysis considers a lateral excitation of the model to excite the mode shapes of interest, and discuss the results in terms of the lateral response of the shaft.

As explained in Chapter 5, a synchronous unbalance excitation is applied laterally to Node 9 as seen in Figure 7.9. The unbalance force amounts to 10% of the disk mass ($\sim 0.042 N$). The response is collected at Node 4 as shown in Figure 7.9. All the data in this chapter are presented in terms of a vectorial sum of both lateral deflections, in X and Y- direction.

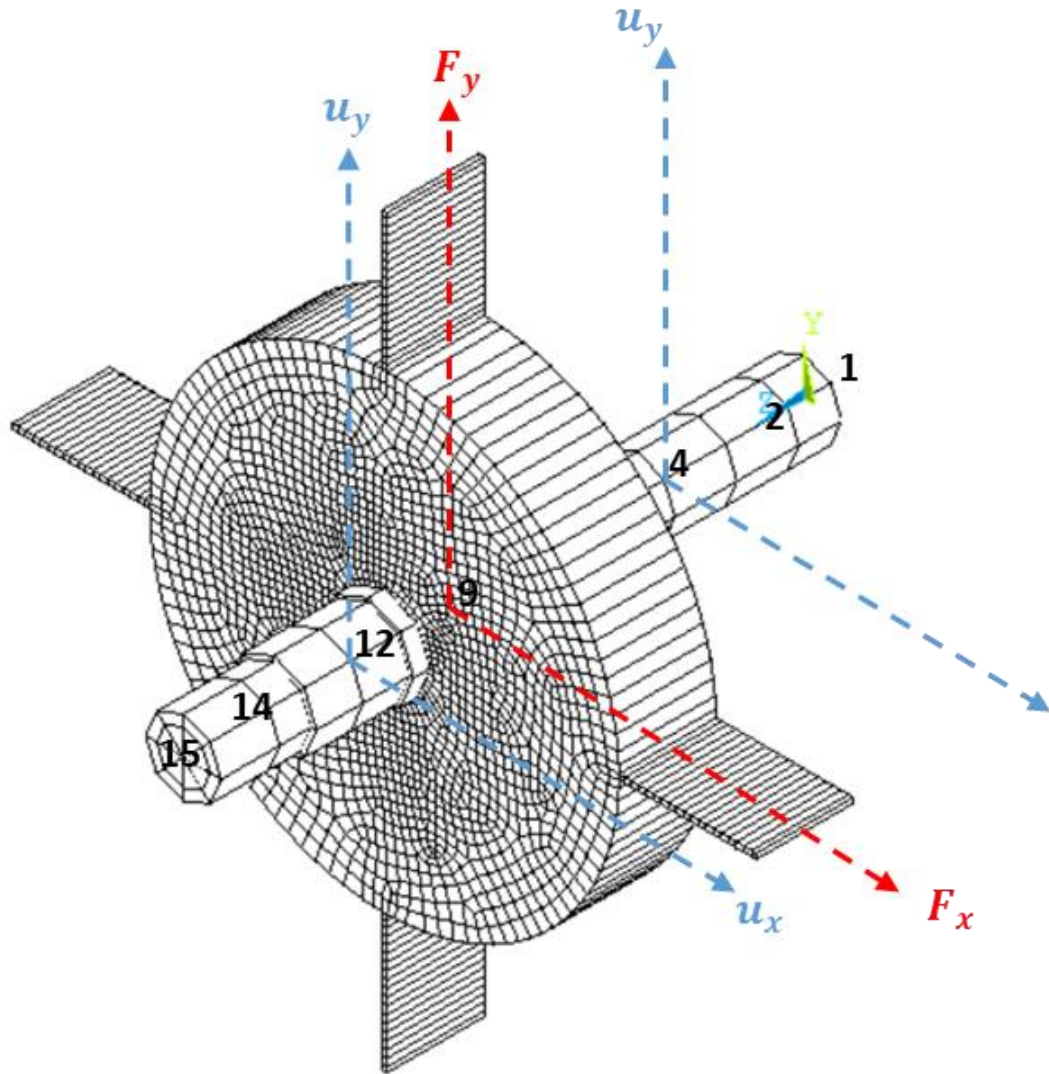


Figure 7.9. Rotor model with harmonic excitation. The dashed red lines resemble the excitation force and the dashed blue lines resemble the collected response values.

7.3.1 Healthy Rotor

The analysis in this chapter is done by establishing a baseline of a healthy rotor lateral-vibrations, benchmark the results of each defect case with the baseline and highlight findings. As a start, the lateral frequency response of Node 4 of a healthy rotor in response to the applied excitation is shown in Figure 7.10.

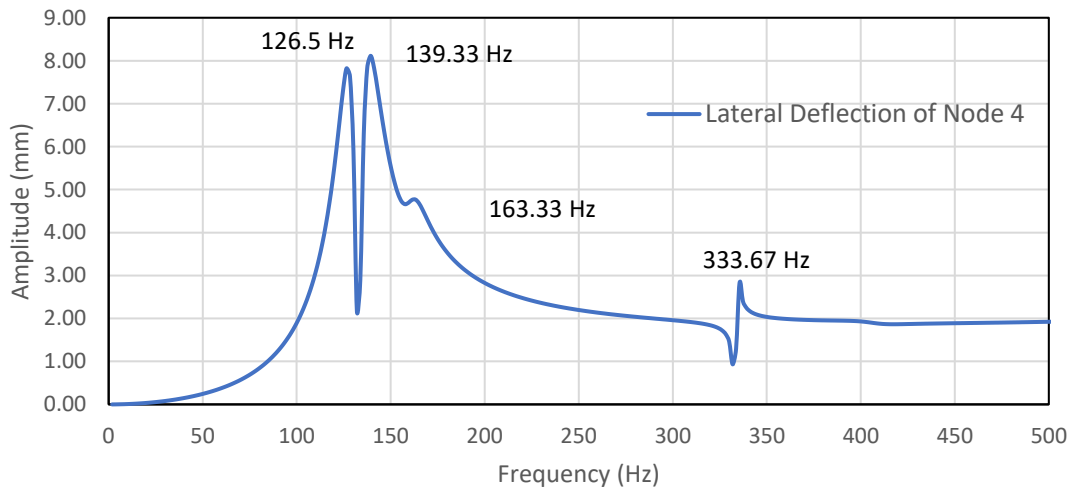


Figure 7.10. Frequency response of the lateral deflection of Node 4 to unbalance excitation.

In Figure 7.10, we observe three major peaks with response amplifications and one minor peak. The three major peaks correspond to the pitching modes of the rotor (126.50 and 139.33 Hz), and the coupling modes among blade-bending and shaft-lateral vibrations (333.51 Hz - even though they are two modes but they appear in one peak due to their close values) as listed in Table 7.4. The minor peak corresponds to the shaft torsional mode shape (154.78 Hz). It is unusual for the torsional modes of vibrations to be excited by lateral excitation, but since Mode 3 is a shaft-mode a minor excitation appears in the spectrum.

Table 7-4. Frequency Peaks of The Lateral Deflection of Node 4 to Unbalance Excitation

Mode	Frequency (Hz)		Error %
	Modal Analysis	Peaks in Harmonic Analysis	
1	132.55	126.50	4.57
2	132.55	139.33	5.11
3	154.78	163.33	5.52
7,8	333.51	333.67	0.05

The results in Table 7.4 agrees with the expectations. First, all excited modes are lateral modes, with the exception of the minor peak due to torsional vibrations which can be neglected due to its small amplification. Second, out of the four blade-dominated mode shapes, only the ones that couple the blade-bending to shaft-lateral vibrations are excited, those are Mode 7 and 8. Mode 6, the blade-blade coupling mode as well as Mode 9, the blade-shaft torsional coupling mode do not appear to be excited by the applied excitation as there are no frequency peaks corresponding to their values. This is expected since the excitation is applied laterally on the shaft.

We also observe in table 7.4 that there is a maximum error of 5% between the frequency values at which the peaks occur and the modal values. This is likely due to the fact that the results are a summation of the lateral responses in both direction x and y-direction.

To verify the feasibility of selecting Node 4, which is arbitrarily selected, to resemble the deflection of the shaft, the response for the same excitation is measured at Node 12 as seen in Figure 7.9. This is just to eliminate the possibility that Node 4 is a nodal point that yields inaccurate results. The frequency response of Node 12 is plotted against that of Node 4 in Figure 7.11 and as appeared, the two responses are alike, with the exception of the torsional

mode peak that does not appear at Node 12 response. Nevertheless, this does not affect the accuracy of the results since the interest in this analysis is on the shaft lateral modes.

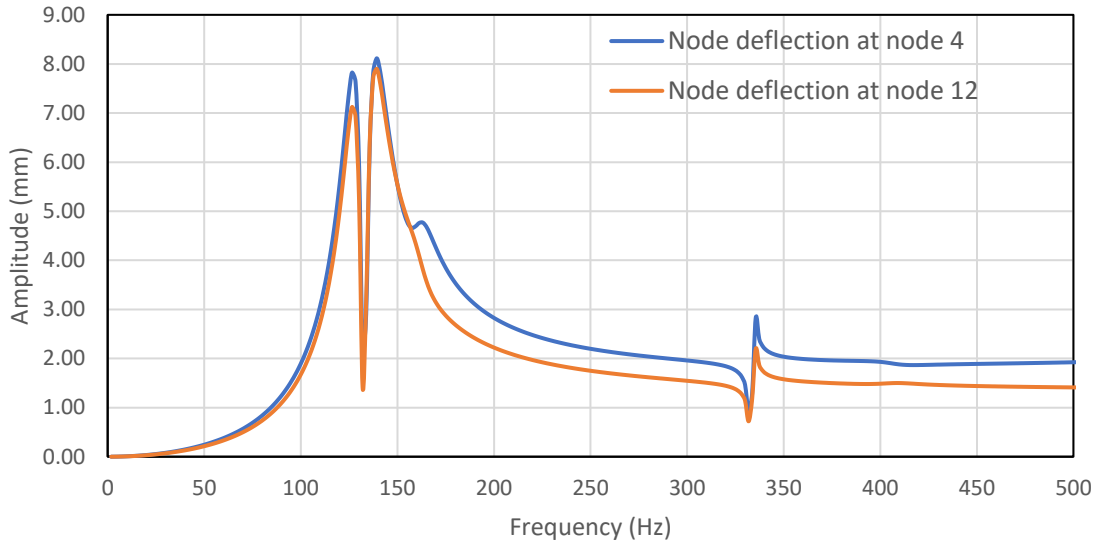


Figure 7.11. Frequency response of the lateral deflection of Node 4 and Node 12 to unbalance excitation.

7.3.2 Blade-Defects Cases

A similar analysis to the healthy rotor is done for each defect cases to identify frequency peaks. The frequency values of the peaks for the cases with one defective blade are listed in Table 7.5.

Table 7-5. Frequency Peaks of The Lateral Deflection of Node 4 at Each Defect Case

Peak #	Healthy Rotor	Broken Blade	Pitted Blade	Bent Blade	Mode Description
1	126.50	126.50	128.33	128.33	Pitching in lateral direction
2	139.33	139.33	141.17	141.17	Pitching orthogonal to previous
3	333.67	333.67	333.67	333.67	Blade Bending - Shaft Lateral
4	-	339.17	339.17	339.17	Blade Bending - Shaft Lateral orthogonal to previous

It is observed from Table 7.5 that the first three peaks of all cases are always corresponding to the same modes, pitching and blade-shaft bending coupling modes, with slight variation in the values. Whenever there is a defect in the blade, an additional peak appears in the lateral response that donates the split in the blade-shaft coupling modes (Mode 7 and 8). The peak frequency values of the blades across the defects are very close. This observation suggest that blade defects have an impact on shaft lateral vibrations. The influence of each defect-case on the response amplitude can be seen in Figures 7.12 through Figure 7.14.

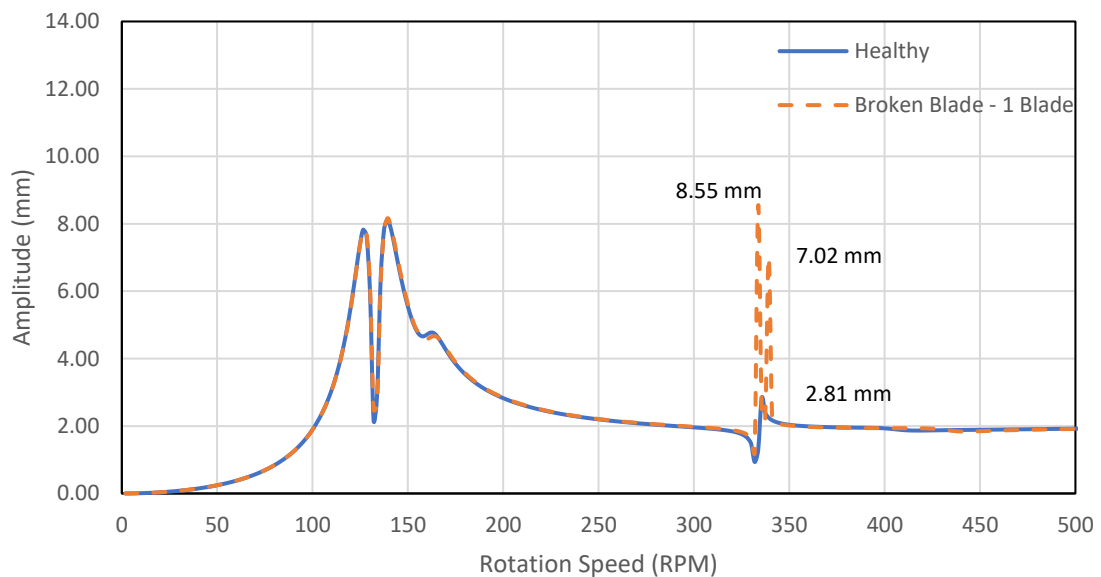


Figure 7.12. Frequency response of the lateral deflection of a model with one broken blade.

Starting with the broken blade case seen in Figure 7.12, we can observe that the amplitude at the first two peaks matches that of a healthy rotor. However, the amplitude that correspond to the blade-bending and shaft-lateral coupling modes is significantly larger than that of a healthy rotor. The difference is in the order of 4:1 mm with two spikes being observed for the two blade-dominated modes.

The pitted blade results are shown in Figure 7.13. While pitted blade cases were the least to influence the modal results of the rotor, Figure 7.13 demonstrates that having a pitted blade in the model causes an amplification in the shaft-lateral response corresponding to the blade-dominated modal frequency. This difference is in the order of 6:1 mm. The two spikes in Figure 7.13 in the pitted case curve correspond to the slight gap between blade-dominated modal frequencies.

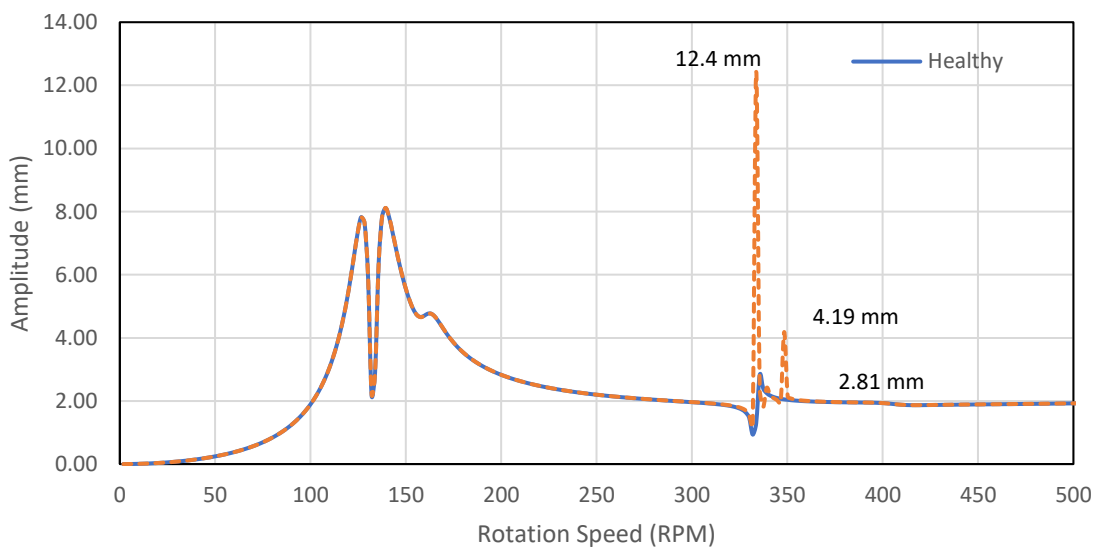


Figure 7.13. Frequency response of the lateral deflection a model with one pitted blade.

Lastly, the lateral response of the shaft in the case of a bent blade is shown in Figure 7.14. Therein, a similar trend to the previous cases is observed. The amplitude of the first two peaks matches that of a healthy blade and a spike in the order of 7:1 is observed at a frequency value corresponding to the blade-dominated modal frequencies.

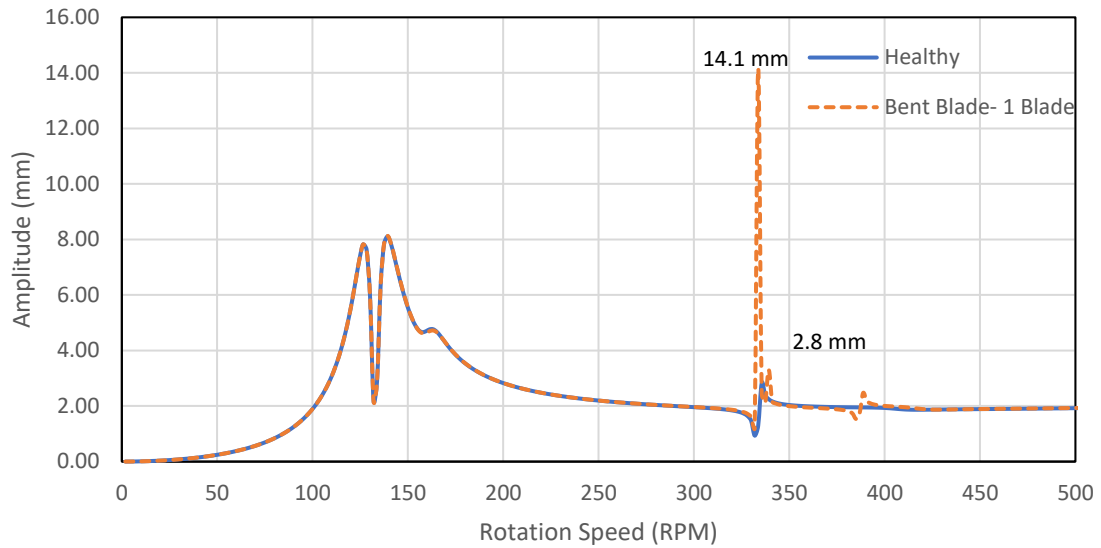


Figure 7.14. Frequency response of the lateral deflection of a model with one bent blade.

Moving to the cases where three blades are defective, the frequency response plots are shown in Figures 6.15, 6.16 and 6.17 for the broken, pitted and bent blades, respectively. Examining the results in Figure 7.14 through 6.16, we observe the following. First, similar to the case of 1 defective blade, defective blades do not impact the amplitude of the first two pitching modes of the rotor. The impact on amplitude is observed on the blade-dominated modes frequencies. However, the impact on amplitude of the 3 defective blade cases is not as severe as the single blade case.

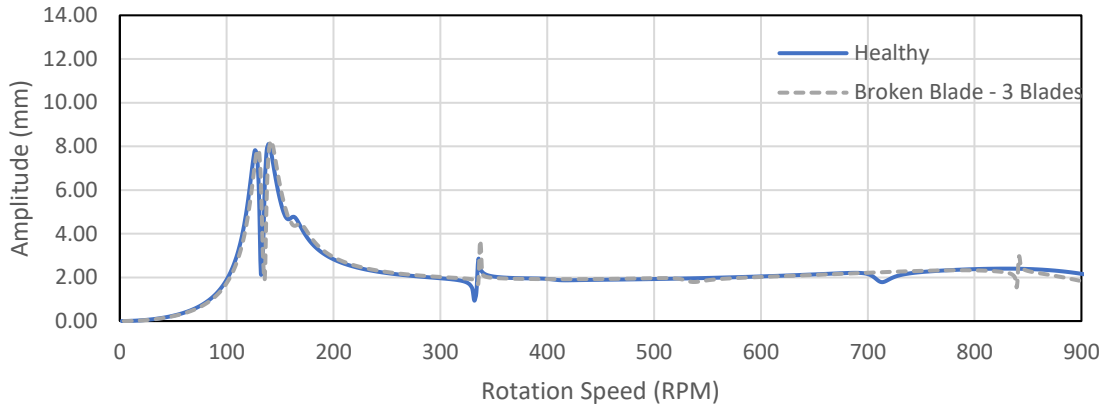


Figure 7.15. Frequency response of the lateral deflection of a model with three broken blades.

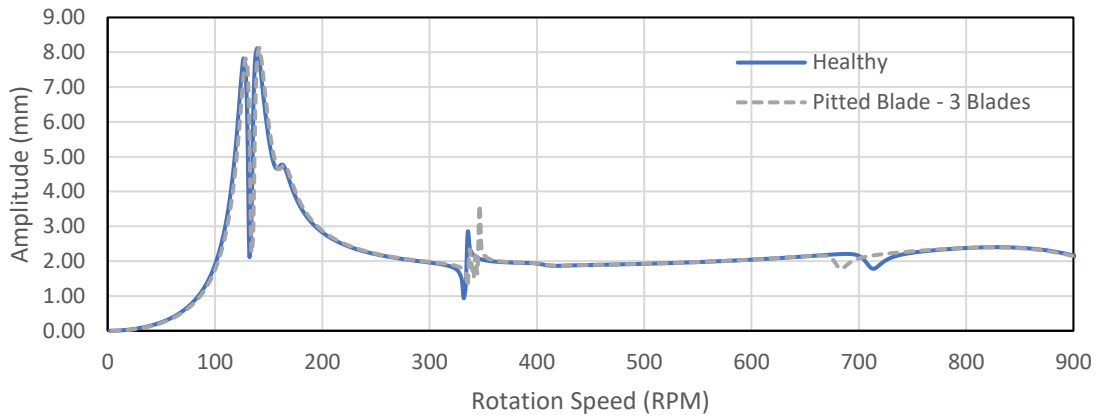


Figure 7.16. Frequency response of the lateral deflection of a model with three pitted blades.

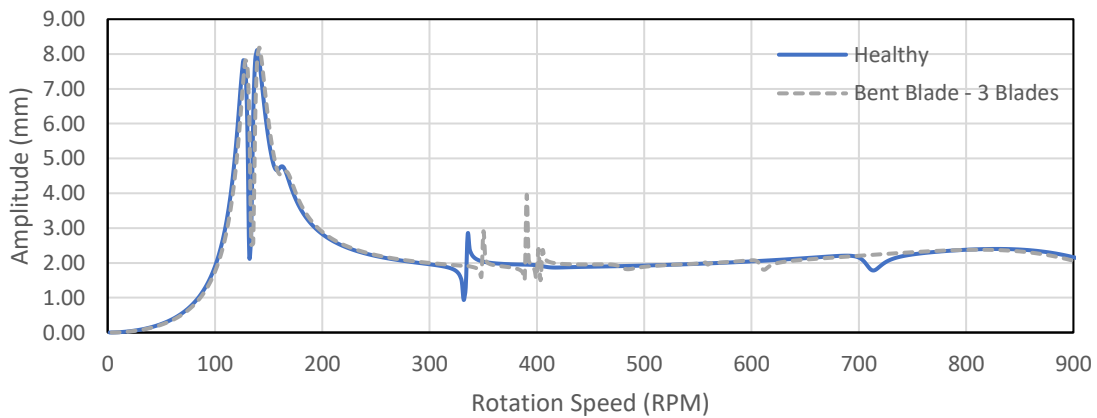


Figure 7.17. Frequency response of the lateral deflection of a model with three bent blades.

To further investigate the influence blade's defects at the blade-dominated mode shapes, the frequency span from 300-450 Hz is magnified in the following figures.

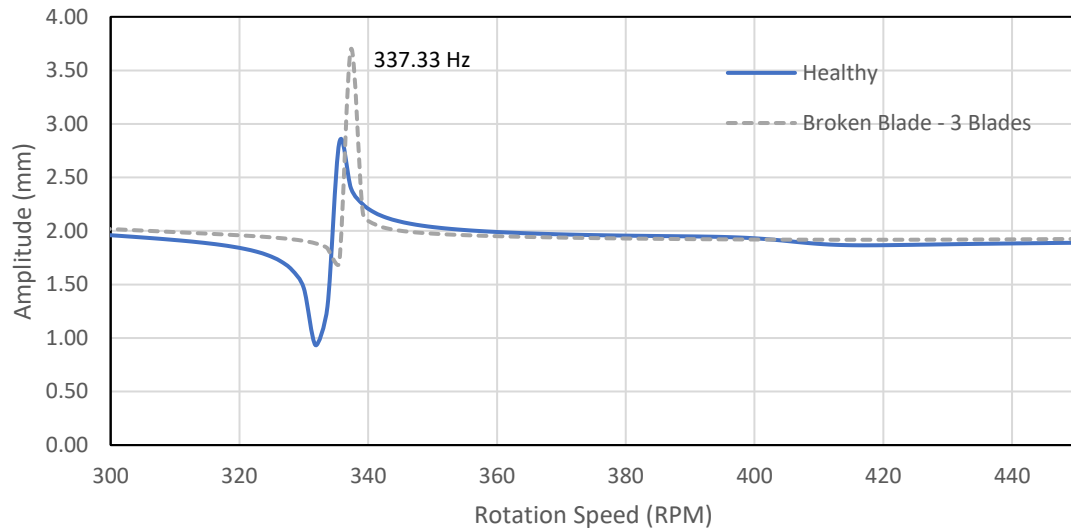


Figure 7.18. Frequency response of the lateral deflection of a model with three broken blades.

In Figure 7.18, we observe that having three broken blades result in a single peak at 337.33 Hz, which correspond to the blade-bending and shaft-lateral coupling mode, with an amplification ratio of about 2:3 as compared with that of the healthy shaft. Building on our understanding from the modal results, this finding is expected as in the case of three-broken blades the only blade-dominated mode is reported is at 335.20 while the other modes are shifted to higher frequency values due to the shortened length of the three blades.

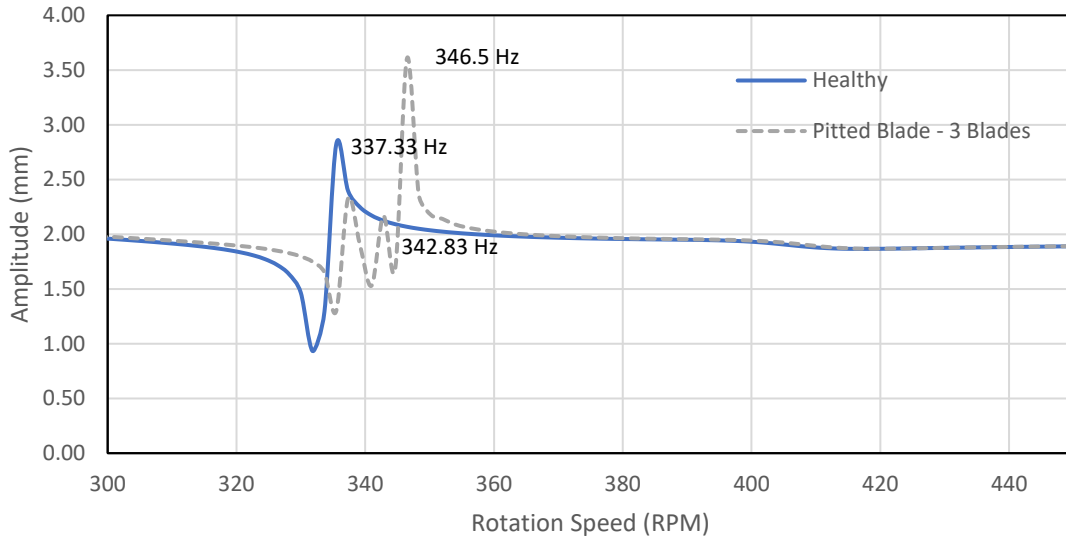


Figure 7.19. Frequency response of the lateral deflection of a model with three pitted blades.

The results of the pitted blades case are shown in Figure 7.19. In there, we notice the appearance of three peaks at 337.33, 346.5 and 342.83 Hz. Only the amplitude of the peak at 346.5 Hz exceed that of the healthy rotor with a ratio of about 2:3. Those frequency values correspond to the two blade-bending and shaft-lateral coupling modes and the blade-bending shaft-torsional coupling mode, with the highest peak occurring at the latter. Here, we observe that the shaft torsional modes get excited when there exists a coupling mode with the defective blades.

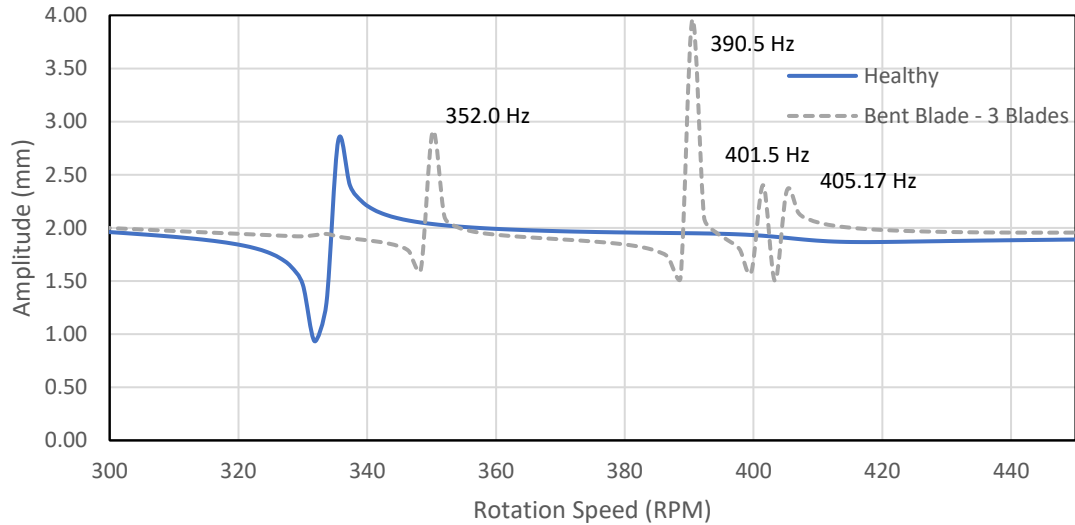


Figure 7.20. Frequency response of the lateral deflection of a model with three bent blades.

Lastly, Figure 7.20 shows the results of the bent blades case. This case resulted in the most influence on the modal results in both, with rotation and without rotation. It also results in the highest amplification ratio when one blade is defective. In the case of three defective blades, we observe the following trends. First, four peaks occur at frequency values of 352.0, 390.5, 401.5 and 405.17 Hz. Referring back to our modal results for this case, we find that those peaks correspond roughly to Mode 6, Mode 7, Mode 8 and Mode 9. Mode 6 is related to the first bending mode of the healthy blade in the model. Mode 7 is related to the first bending-blade of the top bent blade in the model. Mode 8 and 9, are related to the first bending, in-plane, mode of the right and bottom blades, whereas Mode 8 describes the in-phase motion and Mode 9 describe the out-of-phase motion. It was not apparent in the modal analysis that those modes are coupled with the shaft-lateral vibrations modes, but the behavior in Figure 7.20 suggest that they are. In addition, we observe that the peak at Mode 7 yields the largest amplitude ratio as compared with the healthy shaft.

7.4. Summary of Findings

The aforementioned discussion of results in this chapter can be summarized with the following findings.

- 1- There exists a coupling among blade-bending and shaft vibration modes in the rotor. Those modes, called blade-dominated mode shapes, are the most influenced by blade defects, while the other non-blade modes are insignificantly affected by the defects. This segregation in influence on model's mode is the corner stone in detecting blade's defect through indirect vibration measurements.
- 2- The influence of each defect case can, to a great extent but not always, be attributed to the influence of the defect on the blade's first-bending mode-shape. For instance, the shift of blade-dominated mode shapes in the broken-blade cases can be explained by tracing the effect of shortening the blade's longitudinal dimension on the blade first-bending mode-shape frequency value.
- 3- Building a sound understanding of the independent blade's model behavior is essential in understanding the overall modal behavior of the rotor. This was demonstrated in the bent blade cases explanation.
- 4- The understanding of the modal behavior of the rotor aids the interpretation of harmonic analysis results and vice versa. For example, we could only realize that Mode 8 and Mode 9 in the three-bent-blades case are coupled to the shaft lateral vibrations through the results of the harmonic analysis.

- 5- In harmonic analysis with lateral excitation, Blade defects always amplify the lateral response of the shaft, with the single blade-defect contributing to larger amplification than the three-blade defects in all cases.
- 6- Bent blade influence on shaft lateral vibrations amplitude is found the largest with an amplification ratio of 7:1 when benchmarked against a healthy rotor. Then comes the pitted blade case with an amplification ratio of 6:1, and lastly the broken blade case with the least amplification ratio of 4:1.
- 7- In harmonic analysis with lateral excitation, blade defects influence only the amplitude of the modes coupling blade-bending and shaft-lateral vibrations. This validates the assertion that blade defects can be detected by benchmarking the shaft lateral vibrations with a baseline measurement of a healthy rotor. Segregating between the defect might be difficult with no clear signs for each defect. Nevertheless, and since unbalance is inherent in the majority of real rotors, this method can be proven useful for vibration monitoring programs in real applications.

CHAPTER 8

SENSITIVITY ANALYSIS

This chapter addresses the uncertainty analysis in this research. Thus far, all data presented in this study is based on specific inputs. For instance, the model parameters including the material properties, the dimension of each components and bearing's characteristics were all assumed to be deterministic. In real applications, all of those values are subject to scatter. Material properties depend on the resolution of the specimen used to measure them. Likewise, the dimensions are subject to the tolerance of the measurement tools used to collect them. The characteristics of the bearings are true as long as the assumptions they are based on are valid. This means that every input, the developed rotor is associated with, has a degree of uncertainty in real applications. Normally, the results of a deterministic analysis are trustable within the context of the assumptions and conditions governing it. To extend the reliability of the results beyond the controls of the study, the uncertainty in the results must be assessed.

Two common procedures to assess uncertainty in studies are uncertainty analysis and sensitivity analysis. uncertainty analysis aims to quantify and assign numerical values to the scatter of the output that originates due to variation in the input. Sensitivity analysis, on the other hand, addresses the contribution of the variation in input to the uncertainty of the output. Different approaches to both analyses have been developed and used in the literature, including Monte Carlo analysis, response surface methodology and variance

decomposition procedure [42]. In such approaches, the variation in the input is usually modeled using probability prescribed distributions and the uncertainty in the output is quantified by means of statistical analysis.

When the source of input's variation is known in a study, uncertainty analysis is typically conducted to assign numerical values to the uncertainty of the results. This is common in experimental studies since the variations of input can usually be traced to the instrument-induced errors and tolerances. In other studies where quantifying the variation to the input is difficult or not possible, sensitivity analysis can be conducted to assess the impact of input's variance on the accuracy of the results without assigning numerical value to the uncertainty in results.

In this research, deterministic sensitivity analysis is deployed to assess the uncertainty in the results since the research is based on a numerical study of a hypothetical model. Among the several approaches to sensitivity analysis, the Normalized Sensitivity Coefficient (NSC) is used to address the sensitivity of the results to input's variation based on a finite difference scheme (varying one parameter at a time while keeping the others fixed) [43,44].

8.1. Approach to Sensitivity Analysis

The selected approach to sensitivity analysis in this research consists of the following steps,

- 1- Identify key input parameters that are subject to variance
- 2- Vary one parameter at a time while keeping the other parameter constant
- 3- Run the required analysis with the induced variation and obtain the results
- 4- Repeat steps 2 and 3 for other parameters
- 5- Calculate the NSC value of each parameter
- 6- Interpret sensitivity results

The key inputs that are subject to variance in this study are blade's defects. Although modal parameters such as material properties and dimensions are subject to variance in real application, the uncertainty associated with such variance is insignificant to the validity of the results. This is true considering the end objective of this research, which is not to design or assess the performance of a real rotor but to understand the impact of blade's defect on an rotor's vibrations.

The variance of the blade's defect can be addressed through quantifying the variance in the parameters used to simulate those defects. For example, the broken-blade defect was simulated by shortening the length of the blade. This shortened-length is considered the parameter to the broken-blade-defect input. Likewise, the parameters for the other key inputs are established and listed in Table 8.1.

Table 8-1. Key Inputs Parameters in this Research

Key Input	Parameter
Broken Blade	Shortened length of the blade
Pitted Blade	Diameter of created hole
Bent Blade	Radius of curvature of the longitudinal axis of the blade

The defect in each simulated case can occur differently in real application. To assess the sensitivity of the results to the variance in the selected parameter, a range of $\pm 10\%$ variance is considered in each parameter. After that, the modal study of a single-defective blade with no rotation is conducted for each input variation and the natural frequency values of the mode shapes are obtained as output. The modal study is selected as a representative sample for the sensitivity analysis because modal results underlie all the analyses and results that came after in this research.

Upon obtaining the results of each variance case, the Normalized Sensitivity Coefficient (NSC) value can be calculated according to the following equation [43, 44],

$$NSC_i = \frac{\Delta Y}{\bar{Y}} \frac{\bar{X}_i}{\Delta X_i} \quad (7.1)$$

where \bar{Y}_i is the nominal value for the measured output at a nominal value of the input parameter \bar{X}_i . The variation ΔY is the change in the output with a change of ΔX_i in the input model parameter X_i .

8.2. Sensitivity Analysis Results

The results of the sensitivity analysis considering the variation of the broken-blade defects are listed in Table 8.2. The original shortened-length of the blade was 40 mm. Varying that length by $\pm 10\%$ results in changes in the modal results as seen in Table 8.2.

Table 8-2. Normalized Sensitivity Results with Variation in Broken-Blade Shortened-Length

Mode	\bar{X}_1 (mm)	X+ (mm)	X- (mm)	\bar{Y} (Hz)	Y+ (Hz)	Y- (Hz)	ΔX_1 (mm)	ΔY (Hz)	NSC ₁
1	40	44	36	132.67	132.68	132.66	8	0.020	0.075%
2	40	44	36	132.69	132.70	132.68	8	0.020	0.075%
3	40	44	36	155.57	155.62	155.51	8	0.11	0.35%
4	40	44	36	263.00	263.01	263.00	8	0.010	0.019%
5	40	44	36	264.63	264.76	264.47	8	0.29	0.55%
6	40	44	36	332.96	332.96	332.92	8	0.040	0.060%
7	40	44	36	333.50	333.52	333.54	8	-0.020	0.030%
8	40	44	36	339.13	339.14	339.12	8	0.020	0.029%

From Table 8.2, we note that the frequency value of Mode 5, the disk-swing mode, is the most sensitive to the variation in the blade's shortened length with a 0.55% change in the output only, while the other modes have a sensitivity ratio of sub-zero.

Likewise, the results of the sensitivity analysis considering the variation of the pitted-blade and bent-blade defects are listed in Table 8.3 and 7.4, respectively.

Table 8-3. Normalized Sensitivity Results with Variation in Pitted-Blade Hole Diameter

Mode	\bar{X}_2 (mm)	X+ (mm)	X- (mm)	\bar{Y} (Hz)	Y+ (Hz)	Y- (Hz)	ΔX_2 (mm)	ΔY (Hz)	NSC ₂
1	2.5	2.75	2.25	132.57	132.56	132.57	0.5	-0.01	0.038%
2	2.5	2.75	2.25	132.57	132.57	132.57	0.5	0	0%
3	2.5	2.75	2.25	154.86	154.85	154.85	0.5	0	0%
4	2.5	2.75	2.25	262.99	262.99	262.99	0.5	0	0%
5	2.5	2.75	2.25	263.15	263.14	263.18	0.5	-0.04	0.076%
6	2.5	2.75	2.25	332.95	332.71	331.25	0.5	1.46	2.19%
7	2.5	2.75	2.25	333.58	333.08	333.03	0.5	0.05	0.075%
8	2.5	2.75	2.25	337.96	338.01	333.58	0.5	4.43	6.55%
9	2.5	2.75	2.25	348.20	351.63	340.47	0.5	11.16	16.03%

Table 8-4. Normalized Sensitivity Results with Variation in Bent-Blade Radius of Curvature

Mode	\bar{X}_3 (mm)	X+ (mm)	X- (mm)	\bar{Y} (Hz)	Y+ (Hz)	Y- (Hz)	ΔX_3 (mm)	ΔY (Hz)	NSC ₃
1	52.20	57.42	46.98	132.55	132.49	132.60	10.44	-0.11	0.41%
2	52.20	57.42	46.98	132.58	132.53	132.62	10.44	-0.09	0.34%
3	52.20	57.42	46.98	155.00	154.68	155.24	10.44	-0.56	1.81%
4	52.20	57.42	46.98	262.81	262.39	262.94	10.44	-0.55	1.05%
5	52.20	57.42	46.98	263.45	263.20	263.86	10.44	-0.66	1.25%
6	52.20	57.42	46.98	332.99	320.69	332.56	10.44	-11.87	17.82%
7	52.20	57.42	46.98	333.64	332.98	333.40	10.44	-0.42	0.63%
8	52.20	57.42	46.98	339.02	333.57	338.81	10.44	-5.24	7.73%
9	52.20	57.42	46.98	387.10	339.60	473.64	10.44	-134.04	173.13%
10	52.20	57.42	46.98	955.84	884.30	1016.90	10.44	-132.60	69.36%

From Table 8.3, we observe that the sensitivity of the first 5 modes, the rotor modes, to the variation in whole diameter is very minimal. The sensitivity of the frequency value of the blade-bending shaft-torsional coupled mode shape is highest at 16.03%. In contrast, Table 8.4 show elevated sensitivity values for the mode shape frequencies in response to variation in bent-blade's curvature, especially in the blade-dominated mode shapes with the highest sensitivity value reaching 69.36% in Mode 10 and 173.13% in Mode 9.

To further examine the sensitivity of the Mode 9 and 10 in response to variation in the blade's radius of curvature, 10 more runs of the analysis were conducted over the same variance range ($\pm 10\%$) with a 2% variance at each run. The results for Mode 9 and 10 are shown in Figure 8.1 and 7.2, respectively.

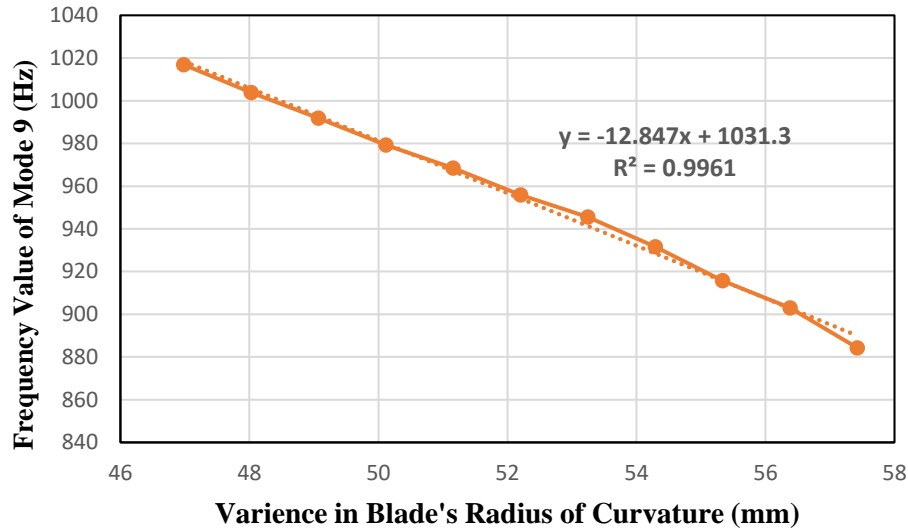


Figure 8.1. Sensitivity analysis results of Mode 9 in bent-blade defect.

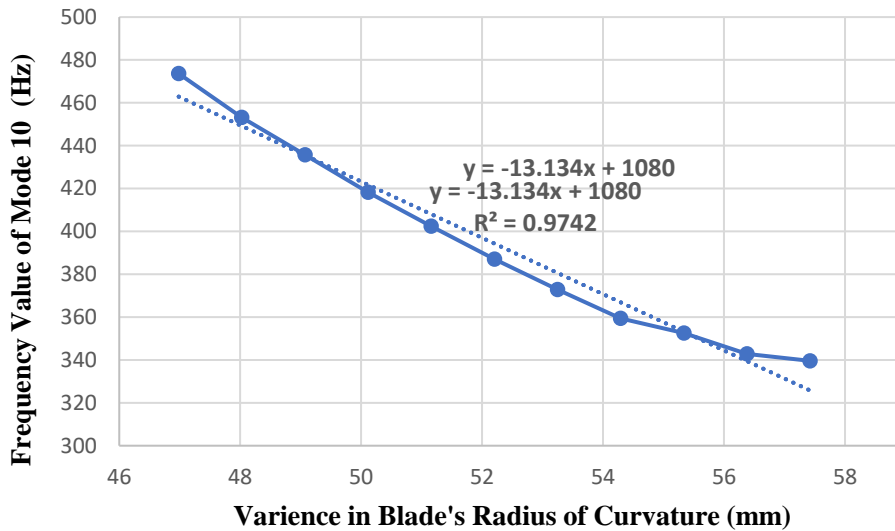


Figure 8.2. Sensitivity analysis results of Mode 10 in bent-blade defect.

The results in Figure 8.1 and 7.2, show that the scatter in the modal results of Mode 9 and 10 in the bent-blade case can be fitted with a linear line with a regression value of 0.99 and 0.97 respectively. This indicates that the model is consistent in calculating the frequency values at each variance, which verifies the robustness of the model despite the relatively high sensitivity of the results to the scatter in the blade’s curvature values.

The overall results of the sensitivity analysis, shown in Figure 8.3, indicates the high reliability of the generated results. First, we note that the modal results are least sensitive to broken-blade simulation scatter, followed by pitted-blade scatter. Second, the first 5 mode shapes are minimally affected by scatter in all key input parameters. In contrast, blade-dominated mode shapes in all cases are of higher sensitivity to input's scatter as compared to the first 5 modes. Yet, with a maximum sensitivity ratio of 16%, the modal results at the blade-dominated mode shapes range are still considered reliable, with the exception of Mode 9 and 10 in the bent-blade defect case. The results of those modes, although accurate, must be interpreted carefully due to their high sensitivity to input scatter.

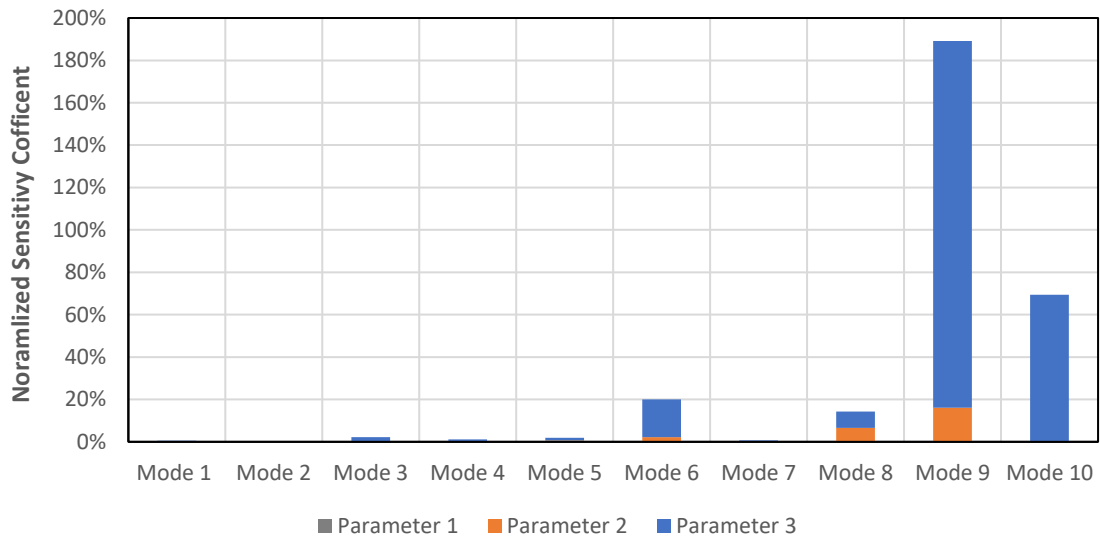


Figure 8.3. Overall NSC values of the Sensitivity Analysis.

CHAPTER 9

CONCLUSION

This study presents a numerical analysis to investigate the feasibility of detecting defects in blades through the analysis of the coupled blade-bending and shaft lateral vibrations in a shaft-disk-blades (SDB) rotor system. The rotor used in this study consists of a single-span shaft supported by ideal bearings, a disk and four rectangular blades. Based on the Energy principle and Lagrange Equations, the equation of motion governing the dynamics of the system was established considering shear deformation, rotary inertia and centrifugal forces effects. The theory underlying the finite element formulation of the rotor elements was discussed to establish a theoretical baseline of the subsequent analysis. The model was then numerically simulated using *ANSYS APDL* software, where modal and harmonic analyses were conducted to generate the results of the study.

Modal validation was accomplished by comparing the modal results of the mode shapes related to the first blade-bending mode, which constitute the scope of this study, with those presented in [36]. In static condition, the modal results in this research were found in agreement with those in [36] with a maximum of 8.22% difference reported at the blade-dominated mode shapes owing to the slight discrepancy in the way blades were modeled in both models. Considering the effect of rotation, the established model was found surpassing the model in [36] in accuracy as it accounts for all rotational effect, including the gyroscopic, spin softening and centrifugal stiffening effect on all rotor components.

Throughout the validation of the model, it was observed that there exists a set of mode shapes that are dominated by the blade's first bending mode, called blade-dominated mode shapes. By varying the number of blades in the model, it was found that the number of those mode shapes matches the number of the blades. Moreover, at least two of those mode shapes are coupled to the shaft lateral vibrations, which establish a potential platform to interpret blade's vibrations through shaft lateral vibrations and vice-versa.

Upon validation of the model, three blade-defects scenarios were simulated, a broken blade, pitted blade and bent blade. One out of four and three out of four blades were defected in each scenario. The study of each scenario was carried out first by benchmarking the modal results of each defect to those of a healthy rotor while considering the effect of rotation. In this analysis, it was found that the blade-defects influence only the blade-dominated mode shapes frequency values at static condition. When rotation is applied, Mode 5, the disk-swing mode, in addition to the blade-dominated mode shapes appear to be influenced by the defect in blades. The pitted-blade defect was found the least in influencing the blade-dominated mode shapes, followed by the broken-blade defect and lastly comes the bent-blade defect that has the highest influence on the blade mode-shapes frequency values. For the most part, the influence of each defect on the frequency values can be attributed to the impact of altering the blade's geometry to the blade's first-bending mode.

Upon establishing a comprehensive understanding of the influence of each defect scenario on the modal result of the rotor system, a harmonic analysis to unbalance excitation was conducted to focus on the coupling among blade-bending and shaft-lateral vibrations. The unbalance excitation was applied laterally to the shaft to excite the lateral modes of

vibrations and the influence of each blade-defect scenario was investigated through benchmark analysis with a healthy rotor. Therein, it was found that blade defects always amplify the lateral vibrations of the shaft at frequency values corresponding to the blade-bending and shaft-lateral vibrations coupling modes. The amplification of the single defective blade at each case was higher than that when three blades are defective. The largest vibration amplification in all cases was recorded at a frequency value corresponding to Mode 7, blade-bending and shaft-lateral coupling mode as expected. The case of bent blade was found of the largest influence to shaft lateral vibrations with an amplification ratio of 7:1 when benchmarked against a healthy rotor. Then comes the pitted blade case with an amplification ratio of 6:1, and lastly the broken blade case with the least amplification ratio of 4:1.

Based on the aforementioned findings, it was concluded that blade's defect can be detected by monitoring shaft lateral vibrations through tracking the vibrations of the shaft corresponding to the coupled modes of blade-bending and shaft-lateral vibrations.

At the end of the study, a sensitivity analysis was conducted to assess the impact of input scatter on the uncertainty of the results, and consequently establish a sense of reliability to the model. The key inputs used in the analysis were the defect to the blades and the considered output was the modal results. To that end, the finite-difference-scheme method was used to conduct the analysis by varying each key input parameter at a time and observe the impact on the output. A variance of $\pm 10\%$ was investigated in each input and the results of the analysis were presented in the form of Normalized Sensitivity Coefficients (NCS). The overall sensitivity results confirm the reliability of the model. The first 5 modal results were found minimally influenced by the scatter in the input in all cases. The blade-

dominated mode shape frequencies were found of higher sensitivity to scatter in the input, but still within acceptable range (maximum of 16% NCS), with the exception of Mode 9 and 10 in the bent-blade case, which were found of relatively higher sensitivity to the scatter in the input.

9.1. Recommendation of Future Research

To enhance the capabilities of the presented model in this research we propose the following set of recommendations that can be addressed through future research.

1- Finite Element Model Refinement

It was highlighted that the numerical model of the rotor was slightly skewed from what was initially discussed in the theoretical formulation of the model. Here we refer to the disk and blade modeling. Due to the imposed limitations in *ANSYS*, we had to model the disk and blades as a single 2-D SHELL181 element to avoid running into axial symmetry issues while accounting for the gyroscopic effect during rotations. Owing to this treatment, we could not vary the stagger angle at which the blades are connected to the disk and assign different thickness values to the blades since disk and blades were all modeled on a single plane (2-D surface). One way to overcome this limitation is by modeling the entire structure as 3-D solid elements, which support accounting for the gyroscopic effect during rotation. This way, the effect of stagger angle and the variation of blade's thickness could be accounted for in the analysis. In addition, the pitted blade defect could be represented more accurately by creating holes in the transverse direction of the blade.

2- Experimental Validation of Results

Validating the modal and harmonic results experimentally can strengthen the validity of the results and add a great deal of practicality to the highlighted findings. The modal results can be verified experimentally by conducting an impact test in static condition and under rotation. The response to the impact test can then be represented using Frequency Response Functions (FRF) to enable comparison with the obtained numerical modal results. Likewise, the harmonic study can be replicated by inducing an unbalance in the disk and measuring the shaft lateral response using proximity probes to allow comparison with obtained numerical results.

3- Additional Blade-Defects Investigation

Only three blade-defect scenarios were studied in this research. In the real world, blades are subject to various forms of defects such as twisting, root looseness and cracks. Simulating different forms of blade's defect, and investigating the feasibility of detecting them through shaft lateral vibrations will strengthen the findings of the study and widen its practicality in real applications.

REFERENCES

- [1] M. Abdelrhman, M. S. Leong, L. M. Hee, and W. K. Ngui, “Application of Wavelet Analysis in Blade Faults Diagnosis for Multi-Stages Rotor System,” *Appl. Mech. Mater.*, vol. 393, pp. 959–964, Sep. 2013
- [2] M. Abdelrhman, M. S. Leong, L. M. Hee , M. S. Leong and Salah Al-Obaidi, “Condition Monitoring of Blade in Turbomachinery: A Review”, *Advances in Mechanical Engineering*, vol. 2014, 2014
- [3] K.H. Hui, L. M. Hee, M. Salman Leong and Ahmed M. Abdelrahman “Vibration Condition Monitoring: Latest Trend and Review.” *Appl. Mech. Mater.*, vol. 773, pp.139-143, May 2015
- [4] Meher-Homji, C., “Blading Vibration and Failures in Gas Turbines-Part A: Blading Dynamics and The Operating Environment”. *ASME Paper*, (95-GT): pp. 418., 1995
- [5] N. Bachschmid, G. Salvini, E. Tanzi and E. Pesatori, “The Influence of Blade Row Dynamics on Lateral and Torsional Shaft Vibrations in Steam Turbines”, *Proceeding of the 9th IFEToMM International Conference of Rotor Dynamics, Mechanisms and Machine Science*, vol. 21, 2015
- [6] B.O. Al-Bedoor, Y. Al-Nasser, L. Ghouti, S.A. Adewsui and M. Abdlsamad, “Shaft Lateral and Torsional Vibration Response to Blade(S) Random Vibration Excitation” *The Arabian Journal for Science and Engineering*, vol. 29, 2004
- [7] Chia-Hao Yang and Shyah-Chin Huang, “The Coupled Vibration in A Shaft-Disk-Blades System”, *Journal of the Chinese Institute of Engineering*, vol. 28, No. 1, pp.89-99, 2005
- [8] B.O. Al-Bedoor, “Natural Frequencies of Coupled Blade-Bending and Shaft-Torsional Vibrations”, *Shock and Vibrations*, vol. 14, pp.65-80, 2007

- [9] Hwanhee Lee, Ji-Seok Song, Seog-Ju Cha and Sungsoo Na, “Dynamic Response of Coupled Shaft Torsion and Blade Bending in Rotor Blade System”, *Journal of Mechanical Science and technology*, vol. 27, 2013
- [10] Chia-Hao Yang and Shyh-Chin Huang, “The Influence of Disk’s Flexibility on Coupling Vibrations of Shaft-Disk-Blades Systems”, *Journal of Sound and Vibration*, vol. 301, pp.1-17, 2007
- [11] Chao-feng Li, Hou-xin She, Wen Liu and Bang-chun Wen, “The Influence of Shaft’s Bending on The Coupling Vibration of a Flexible Blade-Rotor System”, *Mathematical Problem in Engineering*, vol. 2017, 2017
- [12] Akira Okabe, Takershi Kudo, Osami Matsushita, Hiroyuki Fujiwara, Hideo Yoda and Shigeo Sakurai, “Reduced Modeling for Turbine Rotor-Blade Coupled Bending Vibration Analysis”, *Journal of Engineering for Gas Turbines and Power*, vol. 134, February 2012
- [13] Hou-xin She, Chaofeng Li, Qiansheng Tang and Bangchun Wen, “The Investigation of The Coupled Vibration in A Flexible-Disk Blades System Considering the Influence of Shaft Bending Vibration”, *Mechanical Systems and Signal Processing*, vol. 111, pp. 545-569, 2018
- [14] Surajaudeen Adewusi, “Detection of Rotating Blade Faults from Lateral Vibrations of Rotor-Disk-Blade System”, *Proceedings of the 27th conference on mechanical vibration and noise*, August 2015
- [15] Hui Ma, Yang Lu, Zhiyuan Wu, Xingyu Tai, Hui Li and Bangchun Wen, “A New Dynamic Model of Rotor-Blade Systems”, *Journal of Sound and Vibrations*, vol. 357, pp. 168-194, 2015
- [16] I.F. Santos, C.M. Saracho, J.T. Smith and J. Eiland, “Contribution to Experimental Validation of Linear and Non-Linear Dynamic Models for Representing Rotor-Blade

- Parametric Coupled Vibrations”, *Journal of Sound and Vibrations*, vol. 271, pp. 883-904, 2004
- [17] Norihisa Anegawa, Hiroyuki Fujiwara and Osami Matsushita, “Vibration Diagnosis Featuring Blade-Shaft Coupling Effect of Turbine Rotor Models”, *Journal of Engineering for Gas Turbines and Power*, vol. 133, February 2011
- [18] Romuald Rzadkowski and Marcin Drewczynski, “Coupling of Vibrations of Several Bladed Discs on the Shaft”, *Advances in Vibration Engineering*, vol. 8, 2009
- [19] Yi-Jui Chiu and Dar-Zen Chen, “The Coupled Vibration in A Rotating Multi-Disk Rotor System”, *International Journal of Mechanical Sciences*, vol. 35-pp. 1-10, 2011
- [20] Bladh, R., Castanier, M. and Pierre, C., “Effects of Multistage Coupling and Disc Flexibility on Mistuned Bladed Disk Dynamics”, *Journal of Engineering for Gas Turbines and Power*, Vol. 125, pp.121–130, 2003
- [21] Shahab, A. A. S. and Thomas, J., “Coupling Effects of Disc Flexibility on the Dynamics Behavior of Multi Disc-Shaft System”, *J. Sound Vibration*, vol. 114(3), pp. 435–452, 1987
- [22] Rzadkowski, R., Kwapisz, L., Sokoowski, J., Karpiuk, R., Ostowski, P. and Radulski, W., “Natural Frequencies and Mode Shapes of Rotating Three Shrouded Blades Discs Placed on the Part of the Shaft”, *Proceedings of the Second International Symposium On Stability Control of Rotating Machinery*, (ISCORMA-2), Gdańsk, vol. 4–8, pp. 381–392, August 2003
- [23] Gubran, Ahmed “Vibration Diagnosis of Blades of Rotating Machines”, PhD Thesis submitted to the university of Manchester, 2015
- [24] Russhard, P., “The Rise and Fall of the Rotor Blade Strain Gauge, in Vibration Engineering and Technology of Machinery”, *J.K. Sinha, Editor, Springer International Publishing*. pp. 27-37. 2015

- [25] Knappett, D. and J. Garcia, "Blade Tip Timing and Strain Gauge Correlation on Compressor Blades". *Proceedings of the Institution of Mechanical Engineers, Part G: Journal of Aerospace Engineering*. vol. 222(4), pp. 497-506. 2008
- [26] Rao, J., A. Pathak, and A. Chawla, "Blade Life: A Comparison by Cumulative Damage Theories". *Journal of Engineering for Gas Turbines and Power*, vol. 123(4), pp. 886-892. 2001
- [27] Szwedowicz, J., S.M. Senn, and R.S. Abhari, "Optimum Strain Gage Application to Bladed Assemblies". *Journal of turbomachinery*, vol. 124(4), pp. 606-613. 2002
- [28] Petrov, E. and D. Ewins, "Effects of Mistuning on the Forced Response of Bladed Discs with Friction Dampers, iIn Evaluation, Control and Prevention of High Cycle Fatigue in Gas Turbine Engines for Land, Sea and Air Vehicles". *Meeting Proceedings RTO-MP-AVT-121*, pp. 1-16, Neuilly-sur-Seine, France, 2005
- [29] Duan, F., et al. "Research on Detecting Technology of Rotating Blade Vibration Performance Parameters. in Measuring Technology and Mechatronics Automation", *ICMTMA '09. International Conference on Measuring Technology and Mechatronics Automation*. 2009
- [30] Pavel, P. and V. František, "Contactless Diagnostics of Turbine Blade Vibration and Damage". *Journal of Physics: Conference Series*, vol. 305(1): pp. 012116. 2011
- [31] Witoś, M., "High Sensitive Methods for Health Monitoring of Compressor Blades and Fatigue Detection". *The Scientific World Journal*, Vol. 2013. 2013
- [32] García, I., et al., "An Optical Fiber Bundle Sensor for Tip Clearance and Tip Timing Measurements in a Turbine Rig". *Sensors*, vol.13(6), pp. 7385-7398. 2013

- [33] Anuj Kumar Jain, Vikas Rastogi and Atul Kumar Agrawal, “Experimental Investigation of Vibration Analysis of Multi-crack Rotor Shaft”, *Proceedings of the 12th International Conference on Vibration Problems*, vol. 144, pp.1451-1458, 2015
- [34] API 670 - American Petroleum Institute Standard, “Machinery Protection Systems, 5th edition”, 2014
- [35] Yukio, I. Toshio, Y. “Linear and Nonlinear Rotordynamics: A Modern Treatment with Applications”, 2nd Edition. Wiley-VCH Verlag & Co. 2012
- [36] Hui Ma, Yang Lu, Zhiyuan Wu, Xingyu Tai and Bangchun Wen, “Vibration Response Analysis of a Rotational Shaft-Disk-Blade System with Blade-tip Rubbing”, *International Journal of Mechanical Sciences*, vol. 107, pp. 110-125, 2016
- [37] Mohiuddin, Khulief, “Modal Characteristics of Rotors Using a Conical Shaft Finite Element”, *CMAME*, Vol. 115, 1994, p.125-144.
- [38] Bazoune, Abdelaziz, “Vibration Frequencies of Rotating Tapered Beam Including Rotatory Inertia and Transverse Shear Deformation”, Masters of Science Thesis submitted to King Fahad University of Petroleum and Minerals, 1990
- [39] ANSYS “User Manuel”, Version 14.5
- [40] ANSYS “Rotordynamics Guide”, Version 15.0, November 2018
- [41] ANSYS “Advance Theory Guide”, Version 12.0, April, 2009
- [42] Helton, J. C., Johnson, J. D., Sallaberry, C. J., and Storlie, C. B. “Survey of Sampling-Based Methods for Uncertainty and Sensitivity Analysis.” *Reliability Engineering & System Safety*, 91 (10-11): 1175-1209, 2006
- [43] Masi, M, Fogliani, S, Carra, S, “Sensitivity analysis on Indium Phosphide Liquid Encapsulated Czochralski Growth”. *Crystal Research and Technology*, 34:1157–1167, 1999

- [44] M. Iordache, L. Dumitriu, D. Niculae, “On the Sensitivity Analysis of Analog Circuits”,
Annals of the University of Craiova, Electrical Engineering series, 32: 1157–1167, 2008

Vitae

EDUCATION

Master of Science in Mechanical Engineering, Expected in December 2020

King Fahad University of Petroleum and Minerals, Dhahran, SA

Bachelor of Science in Mechanical Engineering, May 2015

Virginia Polytechnic Institute and State University (Virginia Tech), Blacksburg, VA

PROFFICIONAL EMPLOYMENT – SAUDI ARAMCO

Rotating Equipment Standardization Engineer, Dhahran, SA (2018– Current)

Reliability and Maintenance Engineer, Ras Tanura Refinery, SA (2017-2018)

Maintenance Engineer, Ras Tanura Refinery, Ras Tanura Refinery, SA (2016-2017)

Standardization Engineer, Dhahran, SA (2015-2016)

PUBLICATIONS

Alsaleh, Ali L., Sedighi, H.M., Ouakad, Hassen, M., “Experimental and theoretical investigation of the lateral vibrations of an unbalanced Jeffcott rotor”. *Front. Struct. Civil. Eng*, vol. 14, pp. 1024-1032. 2020.

Alsaleh, Ali L., Oukad Hassen, “Analysis of the lateral vibrations of an unbalanced Jeffcott rotor. *The 14th International Conference on Vibration Engineering and Technology of Machinery (VETOMAC XIV)*, Lisbon, Portugal, 2018

Email: aliloay.alsaleh@gmail.com

Address: Abu Aws Al-Aslamy, Azizya, 31311
Dammam, SA